**UNIVERSITY OF SOUTHAMPTON**

FACULTY OF SCIENCE

School of Physics and Astronomy

*Southampton High Energy Physics Group*

# Moments of Parton Distribution Amplitudes and Structure Functions for the Light Mesons from Lattice QCD

*by*

**Thomas David Rae**

*Presented for the degree of*

**Doctor of Philosophy**

UNIVERSITY OF SOUTHAMPTON

# ABSTRACT

FACULTY OF SCIENCE
SCHOOL OF PHYSICS AND ASTRONOMY
SOUTHAMPTON HIGH ENERGY PHYSICS GROUP

Doctor of Philosophy

## Moments of Parton Distribution Amplitudes and Structure Functions for the Light Mesons from Lattice QCD

by Thomas David Rae

This thesis presents the lattice calculation and the required renormalisation for the determination of two hadronic structure quantities. These are the parton distribution amplitudes (PDAs) which enter in the form-factor for exclusive scattering processes and the parton distribution functions (pdfs) that appear in inclusive processes. The PDA's provide process independent partonic information about hadrons and are important quantities required for the calculation of weak physics parameters, such as CKM matrix elements and CP violating phases. We are able to calculate moments of the PDAs on the lattice using two point correlation functions of local operators. This calculation extracts the first two moments for the light mesons and is performed on three ensembles, with parameters, that enable a study of finite volume and discretisation effects. We use the Iwasaki gauge action and $2+1$ flavours of domain wall fermions for all simulations. The calculation of the pdfs through the structure function moments uses three-point correlation functions of local operators. We extract the first odd moment for the pion on our finest lattice, using partially twisted boundary conditions. An important feature of both calculations is non-perturbative renormalisation, using the Rome-Southampton method. The effect of the projections used to isolate the desired renormalisation factors and the momentum choice, that sets the renormalisation scale, on the discretisation errors is detailed through the use of twisted boundary conditions. The results for all quantities are obtained to good precision.

# Contents

# List of Figures

# List of Tables

# Declaration of Authorship

This thesis has been composed by myself and constitutes work completed as part of the broader RBC/UKQCD $N_f = 2 + 1$ domain-wall fermion phenomenology program. It was completed wholly while in candidature for a research degree at Southampton University.

Some of the results have been presented in:

- R. Arthur, P. Boyle, D. Brömmel, M. Donnellan, J. Flynn, A. Jüttner, et al. (2011). Lattice results for low moments of light meson distribution amplitudes. Physical Review D, 83(7), 1-20.
- R. Arthur, P. Boyle, D. Brömmel, M. Donnellan, J. Flynn, A. Jüttner, et al. (2010). Light Meson Distribution Amplitudes (p. 7). PoS(Lattice 2010)154.

I make no claim of originality for chapters 1-6. These chapters present background information compiled from a variety of sources, which have been referenced in the text. Of the original work contained in the remaining chapters, I worked directly on the calculation of the bare structure function and parton distribution amplitude (PDA) moments. I extended the $32^3 \times 64 \times 16$ ensemble measurements for the pdas on Southampton Universitys Iridis-3 cluster computer. I also performed the analysis of the non-perturbative renormalisation factors for both the structure functions and the PDAs. Where work in these chapters has been carried out by others, I have made reference to this within the text.

**Signed:** **Date:**

# Acknowledgements

Firstly, I would like to thank my supervisor, Jonathan Flynn, for his patient guidance, advice and support. I would also like to thank my advisor, Chris Sachrajda, for the many helpful discussions.

It has been a pleasure to work with all my collaborators, including Rudy Arthur, Peter Boyle, Michael Donnellan, Andreas Jüttner, Hugo Pedroso de Lima and James Zanotti. I would particularly like to thank Dirk Brömmel and Andrew Lytle for their helpful discussions throughout my PhD.

I would also like to thank my colleagues, and more importantly friends, James and Jonathan, for keeping my experience as a post-doctoral student interesting and amusing.

My experience would not have been the same without Lisa, to whom I thank for all her love and support.

Finally, I thank my parents for their extended support throughout my entire education.

*This work is dedicated to my family,*
*especially to my wife Lisa, baby Oliver and my*
*parents Dave and Jackie.*

# Chapter 1

# Introduction

Our picture of matter has evolved considerably, specifically what we consider as the fundamental constituents of matter. In the fifth century BC, the Greek philosopher, Democritus, proposed that all matter was built from indivisible or "uncutable" átomos (particles). The name atom has stuck for the modern description, but we now know that the term "atom" is a misnomer as each is divisible into electrons (an example of a lepton), protons and neutrons (types of hadrons).

Following Chadwick's discovery of the neutron in 1932 [4], it was believed that all matter could be built from the "fundamental" particles: the electron, $e^-$, proton, $p$, and neutron, $n$. However, cosmic ray and collider experiments at increasingly large energies were producing new particles that could be considered as equally "fundamental" [5, 6]. By the mid-1960's there were many such particles which raised the question: "Can they all be fundamental?" There was considerable experimental evidence to suggest that this was not the case. An example is neutral meson production, where the interaction of high energy electrons with protons can produce neutral mesons,

$$e^- + p \to e^- + p + \pi^0.$$

This process is very hard to explain without any underlying structure. The large anomalous magnetic moment of the neutron was a further indication of internal structure that involves the distribution of charge. The most conclusive evidence for hadronic structure came from the Deep Inelastic Scattering (DIS) of high energy electrons off of hydrogen at the Stanford Linear Accelerator Centre (SLAC) in the late 1960's [7–9]. The recorded data could be most easily understood if the protons and neutrons were described by collections of point-like particles with fractional electric charge. Inelastic scattering allows the hadronic substructure to be probed as the hadron does not remain intact after the scattering. If the scattering is at a large enough momentum transfer, $Q^2 = -q^2$, the processes that take place are sensitive to very small scales and therefore probe the point-like particles within the hadron.

In 1964, Murray Gell-Mann and George Zweig independently proposed a model that explained the observed spectrum of hadrons using elementary constituents of fractional charge, known as quarks [10–12]. Mesons consist of quark-antiquark bound states, whereas baryons consist of three quark bound states. This model proved a phenomenological success at predicting the hadronic states, however it could not explain the lack of observed particles with fractional charge outside of hadrons or the apparent violation of the Pauli exclusion principle in the case of the $\Delta^{++}$ baryon (composed of three up quarks in the same spin and orbital states). To solve this Nambu, Greenberg and Gell-Mann proposed that quarks carry an additional quantum number: colour [13, 14]. This led to the later development of QCD.

QCD clarified that the point-like particles (partons) within the hadrons were quarks and gluons, which exhibit two defining properties: confinement (quarks and gluons cannot be isolated and are forever bound in hadrons) and asymptotic freedom (the coupling becomes small in the ultra-violet (UV) regime) [15, 16]. At large energies (and thus small distances) the fields may be treated using perturbation theory. This has been exploited and has provided many predictions, which agree with experiment to excellent precision. However in an asymptotically free theory, in the low energy regime (large distances), the coupling becomes large and the use of perturbation theory is no longer satisfactory. Hadronisation, the processes of forming or splitting up hadrons, falls into this regime. Associated quantities are therefore non-perturbative and require a different approach.

Scattering processes can be factorised into two parts: the perturbatively calculable hard scattering of the quarks, gluons, leptons etc. at large momentum transfer and the non-perturbative hadronisation required to form colour singlets. Hadronic scattering processes can be classed as inclusive or exclusive. Inclusive scattering processes are those which are summed over all possible final states, an example of which is the DIS experiments at SLAC that do not depend on the final state and tell us about the partonic content. The partons in such an inelastic scattering are described by their characteristic momentum distributions, known as "parton distribution functions" (pdfs). Complementary information can be extracted from exclusive scattering processes, where all final state particles are observed, such as any elastic scattering process. Exclusive processes provide information about the hadronic structure. One such quantity that we will explore in depth is the parton distribution amplitudes (PDAs). Both the parton distribution functions and amplitudes are non-perturbative quantities and form the subject of interest for this thesis. We will use Lattice QCD (LQCD) coupled with chiral-perturbation theory to extract these non-perturbative quantities for the light mesons.

The brief outline is as follows:

- In chapter 2, I discuss QCD describing the Lagrangian and its symmetries. I will follow this with an introduction to exclusive and inclusive scattering processes and comment upon the information that they provide with respect to hadronic structure.
- In chapter 3, I discuss the formalism of Deep Inelastic Scattering (DIS), developing the previous chapter's discussion of inclusive processes. I will detail the relationship between DIS, the structure functions and the pdfs.
- In chapter 4, I introduce the PDAs through the electromagnetic form factor, commenting on the relation of the PDAs to the Gegenbauer moments that arise in the conformal expansion of massless QCD.
- In chapter 5, I provide an overview of chiral perturbation theory and discuss its applicability in obtaining results at the physical quark masses from the lattice results.

- In chapter 6, I review Lattice QCD (LQCD) and, in particular, discuss the fermion and gauge formulations used by the RBC/UKQCD collaborations. I also discuss the use of partially twisted boundary conditions for tuning the momenta in our simulations, followed by a summary of the simulation parameters used in our calculations.
- In chapter 7, I discuss the calculation of the renormalisation constants required for the moments of the PDAs and structure functions. I present the results from both a perturbative and a non-perturbative calculation.
- In chapter 8, I present the calculation of the second moment for the pion structure function on the lattice for our finest ensemble, and compare our result with existing lattice calculations.
- In chapter 9, I present the calculation and results for the PDAs on the three available lattice ensembles, which allow us to comment on both finite volume and discretisation effects.
- In chapter 10, I present the conclusions as well as future prospects for these calculations.

# Chapter 2

# QCD and the Parton Model

## 2.1 The Standard Model

The Lagrangian that describes the Standard Model (SM) of particle physics is constructed so that it has a local internal gauge symmetry [17]:

$$SU(3)_C \times SU(2)_L \times U(1)_Y. \tag{2.1}$$

The SM offers an excellent description of three of the four fundamental forces of nature within a single framework: electromagnetism, the strong force and the weak force. This is achieved through the combination of Quantum Chromodynamics (QCD), $SU(3)_C$, and electroweak theory, $SU(2)_L \times U(1)_Y$. The fermions in the SM are leptons and quarks. The leptons are organised into three families: the electron $e$ and its neutrino $\nu_e$, the muon $\mu$ and its neutrino $\nu_\mu$, and the tau $\tau$ and its neutrino $\nu_\tau$. Similarly, the quarks are organised into families: $u$ and $d$, $c$ and $s$, $t$ and $b$. The weak interactions can produce transitions between members of the same weak isospin doublet and also between different families, although transitions within the same doublet are dominant. The weak quark doublets are of the form

$$\begin{pmatrix} u \\ d' \end{pmatrix}, \quad \begin{pmatrix} c \\ s' \end{pmatrix}, \quad \begin{pmatrix} t \\ b' \end{pmatrix}, \tag{2.2}$$

where $d'$, $s'$ and $b'$ are weak interaction eigenstates that are related to the strong interaction eigenstates through the Cabbibo-Kobayashi-Maskawa (CKM) unitary matrix [18,19]

$$\begin{pmatrix} d' \\ s' \\ b' \end{pmatrix} = \begin{pmatrix} V_{ud} & V_{us} & V_{ub} \\ V_{cd} & V_{cs} & V_{cb} \\ V_{td} & V_{ts} & V_{tb} \end{pmatrix} \begin{pmatrix} d \\ s \\ b \end{pmatrix}, \tag{2.3}$$

where the elements correspond to the couplings of the $W$ weak gauge boson to all possible quark pairs.

The SM also has a scalar 'Higgs' field that provides a mechanism to generate the fermion and gauge boson masses. All attempts to incorporate gravity into the description have been unsuccessful. The SM also falls short of providing an explanation for some of the phenomena which it encompasses, such as CP violation, the hierarchy of the quark masses or an explanation for the existance of three generations. These have to be introduced "by hand" and manifest themselves as the 19 free parameters of the SM. Nonetheless the SM provides many precise predictions that have been scrutinised time and time again through experiment and have agreed almost without fail. The gyromagnetic ratio calculation of the muon provides a tension between experimental measurements, $(g-2)/2|_{\mathrm{exp}} = 0.0011659208(6)$, and the theoretical predictions, $(g-2)/2|_{\mathrm{th}} = 0.0011659181(7)$ (calculated to order $\alpha^4$ where the theoretical errors are partly due to the numerical evaluation of the Feynman diagrams) at the level of 8 decimal places [20,21]. It is possible that this could be due to new physics beyond the SM. It is expected that, whatever form the complete theory takes, the SM is at least a limiting case of it. In which case the SM is an effective theory describing things well at "low" energy scales but which should be supplemented by something else at high scales. We will continue with a discussion of QCD, but will leave the discussion of the electroweak theory as it is not directly relevant for the work presented in this thesis.

## 2.2 Quantum Chromodynamics (QCD)

In the quark model, quarks required an additional quantum number, colour, in order for the model to be successful phenomenologically. Indirect evidence for this comes from two well known processes: the decay of $\pi^0 \to 2\gamma$ and $e^+e^-$ annihilation. For both of these processes colour appears as an extra factor in the reaction rates [22]. In the latter case, the ratio,

$$R = \frac{\sigma(e^+e^- \to \text{hadrons})}{\sigma(e^+e^- \to \mu^+\mu^-)} = \text{multiplicity} \times \sum_f Q_f^2, \tag{2.4}$$

steps, with increasing centre of mass energy, as the threshold for heavier quark flavours is passed. In order for this to agree with experiment the multiplicity must equal three, the number of identical copies for a particular quark. The quark model, however, did not explain the underlying structure that ensures hadrons are colour singlets, or describe the mechanism behind the interaction between quarks. From the DIS experiments at SLAC it was discovered that quarks exhibit asymptotic freedom, a property shared with non-abelian gauge theories [23]. A non-abelian theory of the strong interactions emerged with colour as the gauge charge of the quarks. The quarks belong to the fundamental representation of the local colour gauge group, $SU(3)$, and the quanta of the $SU(3)$ gauge field are called gluons, which themselves carry colour and exhibit the non-abelian feature of self interacting. The resulting theory is known as Quantum Chromodynamics (QCD).

## 2.3 The QCD Lagrangian

The QCD Lagrangian density is:

$$\mathcal{L}_{QCD} = \sum_f^{N_f} \overline{\psi}_{f,i} \left(i\gamma^\mu D_\mu - m_f\right)_{ij} \psi_{f,j} - \frac{1}{4} F^{a\mu\nu} F^a_{\mu\nu}. \tag{2.5}$$

Quarks are fermions and are therefore described in the free theory by the Dirac equation. However, because QCD is a gauge theory, we replace the derivative in the kinetic term with a covariant derivative, which introduces a coupling between the fermion and gauge fields via the coupling constant, $g_s$. This corresponds to the first term in the Lagrangian, where $\psi_f$ is the quark field for a given flavour $f$ with corresponding mass $m_f$, and the sum is over six quark flavours, $\{u, c, t, d, s, b\}$. $i, j = \{1, 2, 3\}$ are colour indices in the fundamental representation and the spinor indices are suppressed. The $4 \times 4$ Dirac matrices, $\gamma^\mu$, satisfy the anti-commutation relation

$$\{\gamma^\mu, \gamma^\nu\} = 2g^{\mu\nu} \tag{2.6}$$

where the Greek index runs over space-time and $g^{\mu\nu}$ is the space-time metric. The covariant derivative is defined as

$$(D_\mu)_{ij} = \partial_\mu \delta_{ij} - ig_s \left(A_\mu\right)_{ij}. \tag{2.7}$$

The gauge fields, $A_\mu$, transforms under the adjoint representation of the $SU(3)$ gauge group and hence consist of eight gluon fields,

$$A_\mu = A_\mu^a \lambda^a, \tag{2.8}$$

where $\lambda^a$ are the generators of the group $SU(3)$ and follow the commutation relation, involving the structure constants $f^{abc}$,

$$[\lambda^a, \lambda^b] = if^{abc}\lambda^c, \tag{2.9}$$

where $a, b, c$ are colour indices in the adjoint representation that run from 1-8. The generators are conventionally normalised so that

$$\mathrm{Tr}\left(\lambda^a, \lambda^b\right) = \frac{1}{2}\delta^{ab}. \tag{2.10}$$

The second term in the Lagrangian describes the dynamics of the gauge fields, where the field strength tensor can be expressed as

$$F_{\mu\nu}^a = \partial_\mu A_\nu^a - \partial_\nu A_\mu^a + g_s f^{abc} A_\mu^b A_\nu^c, \tag{2.11}$$

(from $F_{\mu\nu} = [D_\mu, D_\nu]$) whose structure clearly demonstrates the possibility of gluon-gluon interactions in QCD.

## 2.4 Symmetries of the QCD Lagrangian

The massless QCD Lagrangian respects many symmetries. It is invariant under Poincaré transformations, scale transformations known as dilatations, and also under special conformal transformations (a combination of translation and space-time inversions). All of these taken together are referred to as "the conformal group". The conformal symmetry that is respected at the classical level is broken by quantum effects (whilst the Lagrangian is scale invariant, the Green's functions are not), leading to the conformal anomaly. This introduces a scale, $\Lambda_{\text{QCD}}$, at which the confinement of quarks occurs and hence determines the masses of the hadrons. This is highlighted by the non-vanishing QCD beta-function [15, 16], given to leading order in perturbation theory by

$$\beta(g_s) = \mu \frac{\partial g_s}{\partial \mu} = -\frac{b_0 g_s^3}{16\pi^2} \quad \text{where} \quad b_0 = \frac{11}{3} N_c - \frac{2}{3} N_f, \tag{2.12}$$

which preserves asymptotic freedom for $N_f \leq 16$ for $N_c = 3$, where $g_s$ is the strong coupling and $N_c$ and $N_f$ are the number of quark colours and flavours respectively. In a classical field theory the coupling constant is dimensionless, however the logarithmic divergences from quantum corrections cause this "constant" to depend on the momentum involved in the process, $Q^2$. At one loop

$$\alpha_s(Q^2) = \frac{4\pi}{b_0 \log(Q^2/\Lambda^2_{\text{QCD}})}, \tag{2.13}$$

where $\alpha_s(Q^2) = g_s^2/4\pi$. The scale parameter $\Lambda_{\text{QCD}}$ is the scale at which $\alpha_s$ becomes strong as $Q^2$ is decreased and has been determined by experiment $\Lambda^2_{\text{QCD}} \approx 200$ MeV. Perturbation theory is only valid when $Q^2 \gg \Lambda^2_{\text{QCD}}$, which is often taken to be above $Q^2 = 1$ GeV for which $\alpha_s(Q^2) \approx 0.4$ [17]. The scale parameter $\Lambda_{\mathrm{QCD}}$ naturally splits the quark masses into two groups,

$$m_u,\ m_d,\ m_s < \Lambda_{QCD} < m_c,\ m_b,\ m_t. \tag{2.14}$$

This splitting means that it is often useful to work in an effective theory, where the heavy quark degrees of freedom are integrated out. This is the case for the lattice calculations using $N_f = 2+1$ (2 degenerate light flavours and 1 heavier flavour) that are described in this thesis. Conformal symmetry does, however, exist in the quantum theory at short distances where $g_s \to 0$ and $\mu \to \infty$ and at tree level, where the beta function vanishes. This proves to be a useful tool in specifying the structure of conformal expansions, which may be used for the calculation of parton distribution amplitudes via Gegenbauer moments.

There are also approximate global symmetries that result from the space-time independent rotations that can be made in flavour space. Writing the kinetic term in terms of left- and right-handed quarks (projecting by $(1 \pm \gamma_5)/2$),

$$\sum_f^{N_f} \overline{\psi}_f \gamma^\mu D_\mu \psi_f = \sum_f \left( \overline{\psi}_{Lf} \gamma^\mu D_\mu \psi_{Lf} + \overline{\psi}_{Rf} \gamma^\mu D_\mu \psi_{Rf} \right). \tag{2.15}$$

We can perform a $U(N_f)$ transformation independently on the left- and right-handed quarks, where the flavours of the left- and right-handed quarks are rotated by independent unitary matrices,

$$\psi_L \to U_L \psi_L, \qquad \psi_R \to U_R \psi_R, \tag{2.16}$$

where

$$\psi_L = \begin{pmatrix} \psi_L^1 \\ \vdots \\ \psi_L^{N_f} \end{pmatrix}. \tag{2.17}$$

This term therefore has the approximate global $U(N_f)_L \times U(N_f)_R$ symmetry. The transformations, $\psi_f \to e^{i\alpha\gamma_5}\psi_f$ and $\psi_f \to e^{i\beta}\psi$ are, respectively, axial $U(1)_A$ and vector $U(1)_V$ symmetries of the action. Anomalous transformations preserve the action but not the measure of the path integral [24]. The axial $U(1)_A$ transformation does not preserve the measure and is known as the “axial anomaly”. The result is the global symmetry $SU(N_f)_L \times SU(N_f)_R \times U(1)_V$, where $U(1)_V$ is just baryon number and the independent $SU(N_f)_{L,R}$ rotations are referred to as chiral symmetry transformations.

The mass term in the Lagrangian couples left- and right-handed quarks and so is not invariant under the full chiral symmetry,

$$\sum_f m_f \overline{\psi}_f \psi_f = \sum_{f,g} \overline{\psi}_{Rf} M_{fg} \psi_{Lg} + h.c.. \tag{2.18}$$

However, if the $N_f$ masses are equal, so that the mass matrix is a multiple of the identity, $M = mI$, then whilst we no longer have a $SU(N_f) \times SU(N_f)$ global symmetry, a $SU(N_f)$ global symmetry remains in which left- and right-handed quarks are rotated in the same way

$$\mathcal{L}_m = m(\overline{\psi}_L \psi_R + h.c.), \tag{2.19}$$

which is invariant under eq. (2.16) where $U_L = U_R$. This approximation can be used for the lightest quarks $u$, $d$ and $s$ since they are considerably below $\Lambda_{QCD}$. If we assume $m_u = m_d$, we have the approximate $SU(2)$ global symmetry, known as isospin. If we were to further assume $m_u = m_d = m_s$ we get the approximate global $SU(3)$ flavour symmetry. Since $m_u$ and $m_d$ are much smaller than $m_s$, the extent to which the symmetry is broken is much less for $SU(2)$ than $SU(3)$.

In the limit where the up and down quarks are massless, QCD has an approximate $SU(2) \times SU(2)$ symmetry. However, there is an added complication due to the vacuum. The QCD vacuum contains a condensate of quark antiquark pairs, which are paired so that the pair has zero total and angular momentum, resulting in pairs of left-handed quarks with right-handed anti-quarks and vice-versa [17]. The resulting vacuum state has a non-zero vacuum expectation value

$$\langle 0 | \overline{\psi}_R \psi_L + \overline{\psi}_L \psi_R | 0 \rangle \neq 0, \tag{2.20}$$

that mixes the two quark helicities. We therefore see that even without explicit quark masses the symmetry is broken. The QCD vacuum spontaneously breaks the $SU(2)$ axial symmetry and results in three quasi-Goldstone Bosons (one for each of the broken generators) . Quasi- refers to the fact that they are not massless because the $SU(2) \times SU(2)$ symmetry is approximate. The particles are, however, much lighter compared to the other hadrons. They are the three pions, with masses $\sim 140$MeV compared with the $\sim 1$GeV protons and neutrons. The vector $SU(2)$ symmetry remains unbroken and is in fact isospin symmetry, particles are arranged in isospin multiplets that are almost degenerate in mass, the three pions form a triplet, the proton and neutron form a doublet, etc.. This explains why the mass difference between the particles in a given multiplet is so small ($\sim 1$MeV) compared to the strong interaction scale ($\sim 100$MeV). Similarly $SU(3) \times SU(3)$ is broken to vector $SU(3)$, but now there are 8 Goldstone Bosons - the octet of pseudoscalar mesons. An effective theory can be constructed, which describes the low energy physics of QCD in terms of the pseudoscalar mesons (Goldstone Bosons) through a simultaneous expansion in the quark masses and momentum. This is chiral perturbation theory and will prove to be a very useful tool in the analysis of our lattice calculations, which will be covered in chapter 5.

## 2.5 The Quark-Parton Model and Factorisation

In the parton model [25], hadrons are viewed as composite particles consisting of constituent partons (point-like particles). The model makes the assumption that the hadrons can be described in terms of partonic states and further that these partons are free (they do not interact with each other). If we consider the scattering of an electron with a hadron through the exchange of a virtual photon with a large momentum transfer. In the centre of mass frame the hadron is Lorentz contracted in the direction of the collision and the internal interactions become time dilated. The lifetime of the partonic states is therefore longer for scatterings with a larger centre of mass energy. When this lifetime is much longer than the length of time the electron takes to pass the hadron, the hadron can be thought of as “frozen” and may be described by a definite number of partons. As these partons are non-interacting they each share a fraction of the hadron’s overall momentum and it makes sense to think of a scattering between the electron and a single parton (this is, at least, true for very high energies, where the virtual photons cannot travel far) [26].

Factorisation addresses the problem of how to calculate high energy cross sections, which are combinations of short- and long-distance effects and are therefore not directly accessible through the usual perturbative methods. Factorisation systematically separates the long- and short- distance effects, allowing the cross-section to be written as a convolution of a perturbatively calculable hard scattering cross section and a non-perturbative function (a PDA for exclusive- and a pdf for inclusive-processes). Factorisation is an assumption of the parton model and is underpinned by the operator product expansion (OPE).

## 2.6 Operator Product Expansion

An operator product like $A(x)B(y)$ is often singular as $x \to y$. The operator product expansion (OPE) allows such products to be written as a series of non-singular operators, $N_j$, with c-number coefficients, $C_j$, that depend on the separation [27],

$$A(x)B(y) \to \sum_j C_j(x-y)N_j(y) \qquad \text{as} \qquad (x-y)^2 \to 0. \tag{2.21}$$

The $C_j$ capture the singularities of the product as $x \to y$. The coefficients are universal for a given product of operators and are therefore not process dependent. It is instructive to look at the dimension of the coefficients,

$$C_i(x-y) \sim (x-y)^{d_{N_i}-d_A-d_B} \tag{2.22}$$

where $d_{\mathcal{O}}$ is the mass dimension of the operator $\mathcal{O}$. The higher the dimension of the operator, $N_i$, the less singular the coefficients, $C_i$, and therefore the operators with the smallest dimension are the most dominant. Furthermore we can perform a Taylor expansion of an operator product, $N_i$, about the light cone. Each successive term in the expansion has an increasing dimension $d_{N_i}$ and correspondingly a less singular coefficient. The result is that the combined expansion becomes ordered in twist (the dimension - spin) of an operator. For the structure functions and distribution amplitudes calculated in this work, the operators are products of currents that are at least bilinear in the fields, and so the leading order (smallest) twist is two [27].

## 2.7 Scattering Processes

Armed with an introduction to the parton model and factorisation, we will continue with a discussion, in the physically intuitive parton picture, of the two classes of hadronic scattering process [27] studied in this thesis.

### 2.7.1 Inclusive Scattering Process

The cross-section for an inclusive scattering process requires an integration over all hadronic final states. DIS is an example of an inclusive process,

$$l(k)H(p) \to l(k')X(p_X) \tag{2.23}$$

where a lepton, $l$, scatters with a hadron, $H$, transferring a large momentum $Q^2$ such that the hadron breaks up into some final state $X$. At large momentum transfer the particle velocities are light-like, and the parton picture is applicable. The virtual photon (mediating the scattering process) couples to a single parton within the hadron, imparting a large momentum to it and ejecting it clear of the hadron. The final-state partons then recombine into colourless hadronic states (fragmentation). This process therefore involves two time-scales: the initial fast scattering, where the parton is ejected before this can be communicated to the other partons and the slower hadronisation process. The inclusive cross-section is then given by the cross section for the lepton-parton scattering at the given parton momentum fraction, $\xi$, multiplied by the probability, $f_{f,H}(\xi)$, that the hadron, $H$, contains a parton of species $f$ at that value of $\xi$, integrated over $\xi$

$$\sigma(l(k)H(p) \to l(k')X(p_X)) = \int_0^1 \mathrm{d}\xi \sum_f f_{f,H}(\xi)\ \sigma(l(k)q_f(\xi p) \to l(k')q_f(p')). \quad (2.24)$$

The probability functions, $f_{f,H}(\xi)$, are known as parton distribution functions (pdfs) and are innately non-perturbative, as they depend on the soft processes that form the structure of hadrons. They can, however, be extracted from experiment and also determined on the lattice (section 8). Whilst they are intrinsic to a given hadron, they are process independent and, once determined, can be used for other inclusive processes involving the given hadron [17].

### 2.7.2 Exclusive Scattering Process

An exclusive process is one where we observe the final state particles. Let us consider the example of elastic electron pion scattering, $e^-\pi \to e^-\pi$. The scattering amplitude for this process involves the pion form factor $F_\pi(Q^2)$ through the matrix element

$$\langle \pi(\mathbf{p}')|V_\mu^{\mathrm{EM}}(0)|\pi(\mathbf{p})\rangle = (p'_\mu + p_\mu)F_\pi(Q^2), \quad (2.25)$$

where $Q^2 = -q^2$ and $q_\mu = p'_\mu - p_\mu$ is the momentum carried by the virtual photon. The vector electromagnetic current between the pion states is defined as

$$V_\mu^{\mathrm{EM}}(x) = \frac{2}{3}\overline{u}(x)\gamma_\mu u(x) - \frac{1}{3}\overline{d}(x)\gamma_\mu d(x). \quad (2.26)$$

There is no term proportional to $(p'_\mu - p_\mu)$ and in the forward limit $F_\pi(0) = 1$ because of charge conservation. As we will see this form factor is a convolution of perturbative and non-perturbative dynamics (eq. (2.27)). In the non-relativistic limit, the form factor can be written as the Fourier transform of the charge distribution and is therefore related to the charge radius.

We, once again, turn to the parton model in order to describe exclusive processes. The partons can be considered as “frozen” during the scattering so that the photon couples to a single parton. Because we are interested in a particular final state, we need to consider the Fock states within the hadron: states consisting of a well-defined number of particles. Once the virtual photon has imparted the large momentum transfer to a given parton, the resulting state is very unlike a pion - the struck parton is likely to be travelling in the opposite direction to the spectator partons. The only way that the partons are likely to reform into a pion is if they are collinear, which requires the communication of the impact between the struck parton and the spectators. This is achieved through the exchange of hard gluons to “turn around” the spectator partons to the direction of the struck parton. There is of course an associated cost with every exchanged hard gluon and we therefore see that the lowest Fock-state dominates the process [26]. The pion’s electromagnetic form factor can be written to leading order as

$$F_\pi(Q^2) = \int_0^1 \mathrm{d}x \int_0^1 \mathrm{d}y \; \phi_\pi^*(y, Q^2) T_H(x, y, Q^2) \phi_\pi(x, Q^2) \tag{2.27}$$

$T_H$ is the scattering amplitude for the form factor where the pions are replaced with collinear partons in the lowest Fock-state $q\overline{q}$. $\phi_\pi$ are process-independent distribution amplitudes and may be interpreted as the probability amplitude for finding the $q\overline{q}$ pair in the pion with momentum fractions $x$ and $\overline{x} = 1 - x$. The hard scattering amplitude $T_H$ can be calculated perturbatively, however the distribution amplitudes $\phi_\pi$ which involve soft effects are intrinsically non-perturbative and require alternative methods for their calculation. They are difficult to extract from experiment without contamination from other hadronic uncertainties, however, they can be determined through a lattice calculation (chapter 9).

Inclusive and exclusive scattering processes provide complementary information and can both be described by the parton model in the large momentum transfer regime, where $Q^2$ is large with respect to $\Lambda_{QCD}$, so that factorisation is applicable. Inclusive processes tell us about hadrons at a partonic level - the pdfs, $f_{f,H}(\xi)$, are the probability of finding a given parton with the momentum fraction $\xi$, whereas exclusive processes provide information at the amplitude level on the structure of the bound hadronic states - the pion PDA, $\phi_\pi$, is the probability amplitude for finding a $q\overline{q}$ pair in the hadron with given momentum fractions. We will cover each of these in chapters 3 and 4.

## 2.8 Light-Cone Quantisation

We have so far discussed two fundamentally different pictures of hadronic structure: the parton model and QCD. The parton model is phenomenologically motivated and is related to experimental observations. In the parton model hadrons are relativistic bound states consisting of confined quark and gluon quanta, whereas QCD has been developed as a covariant non-abelian quantum field theory. It would therefore be desirable if the parton picture could be derived through an appropriate approximation of QCD. In order to do this one could use the conventional Fock-state expansion based upon a quantisation of QCD at a particular time $t = 0$ (the equal-time quantisation). However this has the problem that the zero-particle state in the Fock-basis is not an eigenstate of the Hamiltonian and so does not coincide with the physical vacuum.

Light-cone quantisation offers a formalism for which the vacuum is significantly simpler. The light cone coordinates are defined from the more familiar coordinates

$$(x^0, x^1, x^2, x^3) \rightarrow (x^+, x^1, x^2, x^-) \tag{2.28}$$

where we define

$$x^+ = x^0 + x^3, \qquad x^- = x^0 - x^3 \qquad \text{and} \qquad \mathbf{x}_\perp = (x^1, x^2), \tag{2.29}$$

for which the metric tensor is

$$g_{\alpha\beta} = \begin{pmatrix} 0 & 0 & 0 & 1/2 \\ 0 & -1 & 0 & 0 \\ 0 & 0 & -1 & 0 \\ 1/2 & 0 & 0 & 0 \end{pmatrix}. \tag{2.30}$$

The squared-magnitude of $x$ is then $x^2 = x^+x^- - x_\perp^2$ and we choose the quantisation surface $x^+ = 0$, which is a plane tangent to the light cone [26]. For this choice of quantisation surface, the physical vacuum state now coincides with the zero particle state of the Fock-basis as it is an eigenstate of the full Hamiltonian. It also follows that there cannot be any spontaneous creation of massive fermions from the vacuum which occur in the equal-time quantisation. We can write the Fock-basis states as

$$|0\rangle, \tag{2.31}$$

$$|q\bar{q} : \mathbf{k}_i, \lambda_i\rangle = b^\dagger(\mathbf{k}_1, \lambda_1) d^\dagger(\mathbf{k}_2, \lambda_2)|0\rangle, \tag{2.32}$$

$$|q\bar{q}g : \mathbf{k}_i, \lambda_i\rangle = b^\dagger(\mathbf{k}_1, \lambda_1) d^\dagger(\mathbf{k}_2, \lambda_2) a^\dagger(\mathbf{k}_3, \lambda_3)|0\rangle, \tag{2.33}$$

$$\vdots \tag{2.34}$$

where $b^\dagger$, $d^\dagger$ and $a^\dagger$ create quarks, antiquarks and gluons with momenta $\mathbf{k}_i$ from the vacuum. The $\lambda_i$ is the helicity quantum number. For the case of a pion with momentum $\mathbf{P} = (P^+, \mathbf{P}_\perp)$,

$$\begin{aligned} |\pi(\mathbf{P})\rangle \;&=\; \sum_{n,\lambda_i} \int \prod_i \delta\left(1 - \sum_j x_j\right) \mathrm{d}x_i \; \delta^2\left(\sum_j \mathbf{k}_{\perp j}\right) \mathrm{d}^2\mathbf{k}_{\perp i} \\ &\quad \psi_{n/\pi}\left(x_i, \mathbf{k}_{\perp i}, \lambda_i\right) \left| n : x_i P^+, x_i \mathbf{P}_\perp + \mathbf{k}_{\perp i}, \lambda_i \right\rangle \end{aligned} \tag{2.35}$$

where the delta functions ensure that the fractional momentum $x_i = k^+/P^+$ carried by the Fock-states (sum over $n$) sums to one and that the transverse momentum $\mathbf{k}_{\perp i}$ carried by the Fock states sums to zero. Eq.(2.35) defines the light-cone wavefunction for the pion

$$\psi_{n/\pi}(x_i, \mathbf{k}_\perp, \lambda_i) = \langle n : x_i P^+, x_i \mathbf{P}_\perp + \mathbf{k}_{\perp i}, \lambda_i | \pi(\mathbf{P})\rangle, \tag{2.36}$$

which is the amplitude to find $n$ partons with momentum fractions $x_i$ and transverse momenta $k_{\perp i}$ in the pion.

We are now in a position to rewrite the inclusive parton distribution functions and the exclusive (leading twist) pion distribution amplitudes in terms of the light-cone wavefunction eq.(2.36) [28].

$$f_\pi(x_i, Q^2) = \sum_{n,\lambda_i} \int \frac{\mathrm{d}^2\mathbf{k}_\perp}{16\pi^3} |\psi_{n/\pi}(x_i, \mathbf{k}_{\perp i}, \lambda_i)|^2 \tag{2.37}$$

$$\phi_\pi(x_i, Q^2) = \int \frac{\mathrm{d}^2\mathbf{k}_\perp}{16\pi^3} \psi_{q\bar{q}/\pi}(x_i, \mathbf{k}_{\perp i}, \lambda_i) \tag{2.38}$$

where the pdfs, eq. (2.37), are related to the light-cone wavefunction through an integral over the transverse momenta and a sum over Fock-states, $n$. The pion distribution amplitude, eq. (2.38), is related to the light-cone wavefunction through the integration over transverse momenta for the valence Fock-state [29].

In the following two chapters, I will continue the discussion of the pdfs (chapter 3) and the PDAs (chapter 4) in more detail, resulting in a description of the PDAs and pdfs via an expansion in their moments. This is in anticipation of their calculation via correlation functions of local operators on the lattice.

# Chapter 3

# Deep Inelastic Scattering and Structure Functions

The deep inelastic scattering cross-section can be parameterised in terms of structure functions that characterise the response of the hadron to the leptonic probe. We will start with a description of this and finish by relating the structure functions to the parton model and, hence, the parton distribution functions described in the previous section. The structure functions are discussed in many textbooks, here we follow the discussion in the book by Peskin and Schroeder [17].

## 3.1 Structure Functions

Consider the deep inelastic scattering of an electron with a pion, from which a new state is produced ($e\pi \to eX$), fig. 3.1. The matrix element for this inclusive process

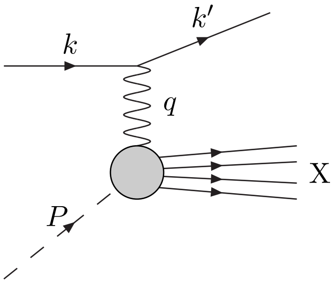

**Figure 3.1:** *Deep inelastic scattering.*

is:

$$iM(e\pi \to eX) = (-ie)\bar{u}(k')\gamma^{\mu}u(k)\frac{-i}{q^2}(ie)\int \mathrm{d}^4x e^{iq.x}\langle X|V^{EM,\mu}(x)|\pi\rangle \tag{3.1}$$

where $V^{EM,\mu}(x) = \sum_f Q_f\bar{\psi}_f(x)\gamma_\mu\psi_f(x)$ is the electromagnetic current and $Q_f$ is the charge corresponding to quark flavour $f$. The momentum transfer is $q = k' - k$. To simplify the calculation of this inclusive process, where we must sum over all possible final states $X$, we apply the optical theorem (diagrammatically fig. 3.2), which relates the total cross section to a forward matrix element.

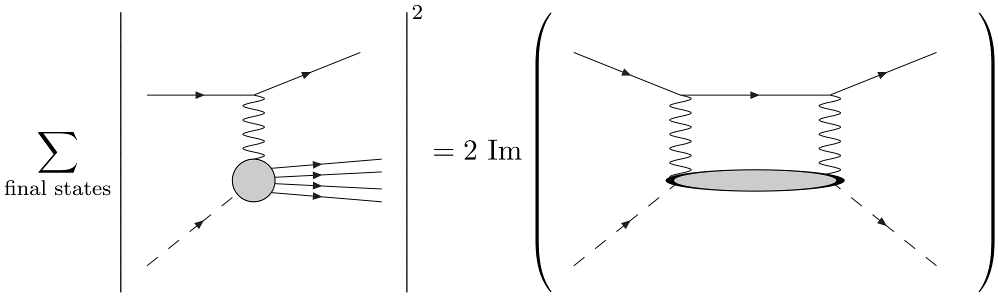

**Figure 3.2:** *The optical theorem applied to DIS.*

It is useful to define the hadronic tensor, $W^{\mu\nu}$, which describes the interaction of the electromagnetic current with the target nucleon and thus parameterises our ignorance of the hadronic current,

$$W^{\mu\nu} = i\int \mathrm{d}^4x \; e^{iq.x}\langle\pi|T\{V^{EM,\mu}(x)V^{EM,\nu}(0)\}|\pi\rangle. \tag{3.2}$$

Applying the optical theorem to $W^{\mu\nu}$,

$$2\ \mathrm{Im}W^{\mu\nu}(P,q) = \sum_X \int \mathrm{d}\Pi_X \ \langle\pi|V^{EM,\mu}(-q)|X\rangle\langle X|V^{EM,\nu}(q)|\pi\rangle, \tag{3.3}$$

where $V^{\mu}(q)$ is the Fourier transform of the current. In lowest order perturbation theory, the cross-section for the scattering of leptons and nucleons may be expressed as a product of leptonic and hadronic tensors that are associated with the upper and lower vertices in fig. 3.1,

$$\sigma(e\pi \to eX) \propto L_{\mu\nu}\ \mathrm{Im}W^{\mu\nu}, \tag{3.4}$$

where $L_{\mu\nu}$ is the leptonic tensor that can be calculated perturbatively within quantum electrodynamics (QED). $W^{\mu\nu}$ can be decomposed using Lorentz symmetry and current conservation and is parameterised by two structure functions.

$$W_{\mu\nu} = W_1\left(-g_{\mu\nu} + \frac{q_\mu q_\nu}{q^2}\right) + W_2\left(P^\mu - \frac{P.q}{q^2}q^\mu\right)\left(P^\nu - \frac{P.q}{q^2}q^\nu\right) \tag{3.5}$$

A more physically intuitive description of the structure functions can be appreciated through the parton model. In this description, the pion matrix element is replaced by a sum of quark and anti-quark matrix elements, each weighted by the parton distribution functions, where $f_{f,H}(x')$ is the probability density of finding a parton $f$ with momentum fraction $x' = p/P$ inside the pion ($H = \pi$), so that,

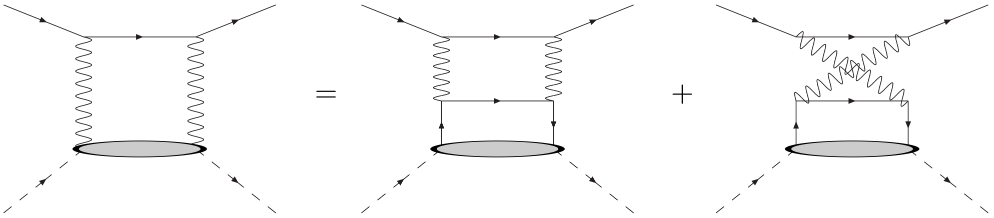

**Figure 3.3:** *The parton model to lowest order for DIS.*

$$W^{\mu\nu} \approx i\int \mathrm{d}^4x\ e^{iq.x}\int_0^1 \mathrm{d}x' \sum_f f_{f,H}(x')\frac{1}{x'}\langle\psi_f(p)|T\{V^{EM,\mu}(x)V^{EM,\nu}(0)\}|\psi_f(p)\rangle, \tag{3.6}$$

and $1/x'$ is the appropriate normalisation [17]. The matrix element can be evaluated by considering non-interacting fermions, for which there are two contributing diagrams (fig. 3.3). The two contributions are identical under the interchange of $\mu \leftrightarrow \nu$ and correspondingly $q \leftrightarrow -q$. Averaging over the quark spin and taking the imaginary part of the result as in the optical theorem results in,

$$\mathrm{Im}W^{\mu\nu} = \sum Q_f^2 f_{f,H}(x)\frac{1}{x}\frac{\pi}{ys}\left(4x^2P^\mu P^\nu + 2x\left(P^\mu q^\nu + P^\nu q^\mu\right) - g^{\mu\nu}xys\right), \tag{3.7}$$

where $x$, $y$ and $s$ are invariant quantities. The Bjorken $x = Q^2/(2P.q)$ is related to the momentum fraction, $x'$, through a delta function, $s = (k+P)^2$ is the centre of mass energy squared of the lepton-hadron system and $y = Q^2/(xs)$ is the lepton's energy in the hadron's rest frame. Through adding and subtracting terms proportional to $q^\mu q^\nu$, and comparing eq. (3.5) with eq. (3.7) we see that, to lowest order in the parton model, the structure functions are given by

$$\begin{aligned} \mathrm{Im}W_1 &= \pi \sum_f Q_f^2 f_{f,H}(x), & (3.8) \\ \mathrm{Im}W_2 &= \frac{4\pi}{ys} \sum_f Q_f^2 x f_{f,H}(x), & (3.9) \end{aligned}$$

where the sum runs over the different quarks and anti-quarks, weighted by their corresponding charge, $Q_f$. The relation

$$\mathrm{Im}W_1 = \frac{ys}{4x} \mathrm{Im}W_2 \tag{3.10}$$

is known as the Callan-Gross relation [30] and reflects the spin $\frac{1}{2}$ nature of the quarks. At this order, we see that the cross-section is independent of the probing momentum $Q^2$, known as Bjorken scaling [31]. This is however violated for large $Q^2$ due to the emission of gluons from the interacting quark. The parton distribution functions $f_{f,H}(x)$ are universal to the hadron $H$ (in our case, the pion) and do not depend on the process. They cannot be calculated in perturbation theory and so lattice QCD is a useful tool for their evaluation.

## 3.2 Moments of the Structure Functions

Whilst the parton model provides a good physical interpretation of the process, the operator product expansion provides a more explicit treatment of the expansion of the product of currents. It enables us to rewrite the product of quark currents in eq. (3.2) as a sum of terms each with a local operator and a coefficient. The most important terms in the operator product of quark currents at lowest order are

$$\overline{q}(x)\gamma^{\mu}q(x)\overline{q}(0)\gamma^{\nu}q(0) = \overline{q}(x)\gamma^{\mu}\overbracket{q(x)\overline{q}}(0)\gamma^{\nu}q(0) + \overbracket{\overline{q}(x)\gamma^{\mu}q(x)\overline{q}(0)\gamma^{\nu}q}(0) \tag{3.11}$$

(corresponding to the two diagrams in fig. 3.3). Performing the Fourier transform in eq. (3.2), and expanding in the short-distance limit for which $q$ is larger than the external momenta, we find that the complete operator expansion only contains terms even in $q$. These terms are all of the form

$$\overline{q}\gamma^{\mu_1}\left(i\partial^{\mu_2}\right)\cdots\left(i\partial^{\mu_k}\right)q. \tag{3.12}$$

It is therefore useful to define the operator with $n$ derivatives as

$$\mathcal{O}_f^{(n)\{\mu_1\ldots\mu_n\}}(x,t) = \bar{q}_f(x,t)\gamma^{\{\mu_1}(iD^{\mu_2})\ldots(iD^{\mu_n\}})q_f(x,t) - \text{traces}. \tag{3.13}$$

where we have introduced covariant derivatives, so that we have gauge invariant operators. The subtraction of traces ensures that we avoid any mixing due to the many different irreducible representations of the Lorentz group that could otherwise contribute to this operator. This operator may then be used to write an expression for the most singular part of the OPE of the two currents,

$$\begin{aligned} i\int \mathrm{d}^4x\ e^{iq.x}V^{\mu}(x)V^{\nu}(0) \quad &= \quad \sum_f Q_f^2\left[4\sum_{n=2,4,\cdots}^{\infty}\frac{(2q^{\mu_1})\ldots(2q^{\mu_{n-2}})}{(Q^2)^{n-1}}\mathcal{O}_f^{(n)\mu\nu\mu_1\ldots\mu_{n-2}}\right. \\ &\left. -g^{\mu\nu}\sum_{n=2,4,\cdots}^{\infty}\frac{(2q^{\mu_1})\ldots(2q^{\mu_n})}{(Q^2)^n}\mathcal{O}_f^{(n)\mu_1\ldots\mu_n}\right] + \ldots \end{aligned} \tag{3.14}$$

The hadronic tensor involves currents taken between two hadronic (meson) states, which we may now write in terms of the operators, $\mathcal{O}_f^{(n)}$,

$$\langle\pi(P)|\mathcal{O}_f^{(n)\mu_1\cdots\mu_n}|\pi(P)\rangle = A_f^n\ 2P^{\mu_1}\cdots P^{\mu_n} - \text{traces}, \tag{3.15}$$

the only Lorentz structure that this matrix element can depend on is the pion's momentum $P$. By comparing the insertion of eq. (3.14) in eq. (3.2) with eq. (3.5) we can relate the structure functions to the coefficients $A^n$. Note that, for the case of two currents with different flavour this is only true if the cross terms (supressed by $(1/Q^2)$ relative to the leading terms) are neglected, which allows the hadronic tensor to be separated into a series of flavour terms $W^{\mu\nu} = \sum_f Q_f^2 W_f^{\mu\nu}$ ,

$$W_1 = \sum_f Q_f^2 \sum_{n=2,4,\cdots}^{\infty} 2\frac{(2q.P)^n}{(Q^2)^n} A_f^n, \tag{3.16}$$

$$W_2 = \sum_f Q_f^2 \sum_{n=2,4,\cdots}^{\infty} \frac{8}{Q^2}\frac{(2q.P)^{n-2}}{(Q^2)^{n-2}} A_f^n. \tag{3.17}$$

The size of contributions to the OPE are ordered by their twist (the operator's dimension minus its spin), which, for the operators that we are considering (two currents of the same flavour) is twist two. The OPE enables the evaluation of expressions for $W_1$ and $W_2$ as an expansion in inverse powers of $Q^2$. However, for this, $Q^2$ must be larger than any other invariant kinematic. The physical region of deep inelastic scattering, is $2p.q \geq Q^2$, therefore a dispersion relation is required to relate $W_1$ and $W_2$ to the deep inelastic cross-section. This results in "momentum sum rules" which relate the moments of the parton distribution functions $f(x)$ to the pion matrix elements of twist-2 operators

$$A_f^n = \int_0^1 x^{n-1}[f_f(x) + (-1)^n f_{\bar{f}}(x)]\mathrm{d}x \qquad \text{for } \; n = 1, 2, \ldots \; . \tag{3.18}$$

The coefficients $A_f^n$ are dimensionless and are related to the structure functions. For the case $n = 1$ the operators reduce to the quark vector currents and $A_f^1$ is equal to the number of quarks minus anti-quarks of flavour $f$ in the state, $N_f$. $A_f^2$ corresponds to the momentum carried by the quarks of flavour $f$, $\langle x \rangle$.

$$A_f^1 = \int_0^1 [f_f(x) - f_{\bar{f}}(x)]\mathrm{d}x = N_f \tag{3.19}$$

$$A_f^2 = \int_0^1 x[f_f(x) + f_{\bar{f}}(x)]\mathrm{d}x = \langle x \rangle_f \tag{3.20}$$

In chapter 8 we will present our results for $A_f^2$ for the pion, which we determine on the lattice using ratios of correlation functions that contain local operators.

# Chapter 4

# Distribution Amplitudes

Chapter 2 introduced the PDAs through the elastic electron-pion exclusive scattering process, where the form factor for this process may be described by an incoming and outgoing PDA convolved with a perturbatively calculable scattering kernel. The PDAs are ubiquitous in exclusive scattering processes that involve an element of hadronisation and therefore factorisation. The PDAs are process-independent quantities. A topical application, that highlights the importance of the determination of the PDAs, is to the ongoing $B$-physics experiments at $B$-factories such as BaBar and Belle. Here, the PDAs play a vital role in parameterising the non-perturbative physics within the factorisation of $B$-decays. The light pseudoscalar meson PDAs are important for the non-leptonic decays that are used for measuring CP-violation $B \to \pi\pi$ and $B \to \pi K$, whereas the vector mesons are useful for the extraction of the CKM matrix elements such as $|V_{ub}|$ through channels such as $B \to \rho l v_l$, $B \to \rho\gamma$ and $B \to \rho\pi$ [32–34]. A considerable motivation for our LQCD simulations is to use our PDA results in combination with experiment to check CKM matrix elements and flavour physics in general.

For this work we will only consider the leading order (twist-two) distribution amplitudes for the light mesons and the longitudinally polarised vector mesons $K^*$ and $\rho$. We exclude the $\eta$ meson from our calculations due to its mixing with the $\eta'$ meson, which is a flavour singlet and therefore suffers contributions from disconected diagrams. The distribution amplitudes are defined on the light cone through vacuum-to-meson matrix elements of quark-antiquark light-cone operators. For the pseudoscalar mesons, this is of the form

$$\langle 0|\bar{q}(z)\gamma_\rho\gamma_5\mathcal{P}(z,-z)q'(-z)|\Pi(p)\rangle|_{z^2=0} \equiv f_\Pi(ip_\rho)\int_0^1 \mathrm{d}x e^{i(x-\bar{x})p.z}\phi_\Pi(x,\mu). \tag{4.1}$$

However, for the vector mesons, due to the polarisation, we have the choice of longitudinally and transversely polarised vector meson states, each of which allow the opportunity to study different aspects of weak interaction physics [34]. We will concentrate on the longitudinally polarised case for which,

$$\langle 0|\bar{q}(z)\gamma_\rho\mathcal{P}(z,-z)q'(-z)|V(p,\lambda)\rangle|_{z^2=0} \equiv f_V m_V(p_\rho)\frac{\epsilon_{(\lambda)}.z}{p.z}\int_0^1 \mathrm{d}x e^{i(x-\bar{x})p.z}\phi_V^{||}(x,\mu) \tag{4.2}$$

where $x$ and $\overline{x} = 1 - x$ are the momentum fractions carried by the two quarks respectively. The quantities $f_\Pi$ and $f_V$ in eqs. (4.1) and (4.2) are the decay constants. For a pion the decay constant is defined by the pion-to-vacuum matrix element of the axial vector current,

$$\langle 0|\overline{u}\gamma_\mu\gamma_5 d|\pi(p)\rangle = if_\pi p_\mu, \tag{4.3}$$

and for the vector, containing polarisation index $\lambda$ and polarisation vector $\epsilon^\mu_{(\lambda)}$, is defined as

$$\langle 0|\overline{q'}\gamma_\mu q|V(p,\lambda)\rangle = f_V m_V \epsilon^\mu_{(\lambda)}. \tag{4.4}$$

The expressions above contain the path ordered exponential,

$$\mathcal{P}(z,-z) = P\exp\left(-ig\int_{-z}^{z}\mathrm{d}w^\mu A_\mu(w)\right), \tag{4.5}$$

which ensures gauge invariance. The distribution amplitudes reduce to the decay constants as $z \to 0$. We are able to write the PDAs in terms of moments through a Taylor expansion about $z = 0$. The normalisation of the distribution amplitudes is given by,

$$\int_0^1 \mathrm{d}x \phi_\Pi(x,\mu) = 1. \tag{4.6}$$

The first moment is,

$$\begin{aligned} \partial_\mu \langle 0|\overline{u}(z)\gamma_\rho\gamma_5\mathcal{P}(z,-z)d(-z)|\Pi(p)\rangle|_{z^2=0} &= \langle 0|\overline{u}(0)\gamma_\rho\gamma_5(\overleftarrow{D}_\mu - \overrightarrow{D}_\mu)d(0)|\Pi(p)\rangle \quad (4.7) \\ \langle 0|\overline{u}\gamma_5\gamma_\rho(\overleftarrow{D}_\mu - \overrightarrow{D}_\mu)d|\Pi(p)\rangle &= f_\Pi(ip_\rho)(ip_\mu)\int_0^1 \mathrm{d}x(2x-1)\phi_\Pi(x,\mu) \quad (4.8) \end{aligned}$$

For mesons of definite G-parity, such as the pion, the odd moments vanish. Isospin symmetry implies that $\phi(x,\mu)$ is symmetric under the interchange of the $u$ and $d$ quarks and, hence, of $x$ and $\overline{x}$, so that

$$\int_0^1 \mathrm{d}x(2x-1)^{2n+1}\phi(x,\mu) = 0 \tag{4.9}$$

for integer $n$. This is not the case for the kaon and is an important example of $SU(3)$ breaking. The first moment provides the difference between the longitudinal momentum fractions carried by the valence quarks and we therefore expect this to be positive. The pion's first non-trivial moment is the second

$$\langle 0|\overline{u}(0)\gamma_5\gamma_{\{\rho}(\overleftrightarrow{D}_\mu \overleftrightarrow{D}_{\nu\}})d(0)|\pi(p)\rangle = f_\pi(ip_\rho)(ip_\mu)(ip_\nu)\int_0^1 \mathrm{d}x(2x-1)^2\phi_\pi(x,\mu) \tag{4.10}$$

where we have symmeterised over the indices and have introduced the definition $\overleftrightarrow{D}_\mu = \overleftarrow{D}_\mu - \overrightarrow{D}_\mu$ where $\overrightarrow{D}_\mu = \overrightarrow{\partial}_\mu + igA_\mu$ and $\overleftarrow{D}_\mu = \overleftarrow{\partial}_\mu - igA_\mu$. We therefore have a parameterisation of the distribution amplitudes in terms of their moments

$$\langle \xi^n \rangle = \int_{-1}^1 \mathrm{d}\xi \xi^n \phi(\xi,\mu) \tag{4.11}$$

where the difference between the longitudinal momentum fractions is $\xi = x - \bar{x} = 2x - 1$. It is this parameterisation of the distribution amplitudes

$$\langle 0|\mathcal{O}_{\{\mu_0 \ldots \mu_n\}}(0)|\Pi(p)\rangle = \langle \xi^n \rangle_\Pi f_\Pi p_{\mu_0} \ldots p_{\mu_n} + \ldots \tag{4.12}$$

in terms of matrix elements of local operators

$$\mathcal{O}_{\{\mu_0\cdots\mu_n\}}(0) = (-i)^n\overline{\psi}\gamma_{\{\mu_0}\gamma_5\overleftrightarrow{D}_{\mu_1}\ldots\overleftrightarrow{D}_{\mu_n\}}\psi \tag{4.13}$$

which allows for their study on the lattice. The expressions which relate the moments of the distribution amplitudes to the matrix elements containing the appropriate local matrix elements are:

$$\begin{aligned}
\langle 0|\overline{q}(0)\gamma_{\{\rho}\gamma_5\overleftrightarrow{D}_{\mu\}}s(0)|K(p)\rangle &= \langle\xi^1\rangle_K f_K p_\rho p_\mu & (4.14)\\
\langle 0|\overline{q}(0)\gamma_{\{\rho}\gamma_5\overleftrightarrow{D}_{\mu}\overleftrightarrow{D}_{\nu\}}q(0)|\pi(p)\rangle &= -i\langle\xi^2\rangle_\pi f_\pi p_\rho p_\mu p_n u & (4.15)\\
\langle 0|\overline{q}(0)\gamma_{\{\rho}\overleftrightarrow{D}_{\mu\}}s(0)|K^*(p,\lambda)\rangle &= \langle\xi^1\rangle^{\parallel}_{K^*} f_{K^*} m_{K^*}\frac{1}{2}(p_\mu\epsilon^{(\lambda)}_\rho + p_\rho\epsilon^{(\lambda)}_\mu) & (4.16)\\
\langle 0|\overline{q}(0)\gamma_{\{\rho}\overleftrightarrow{D}_{\mu}\overleftrightarrow{D}_{\nu\}}q(0)|\rho(p)\rangle &= -i\langle\xi^2\rangle^{\parallel}_{\rho} f_\rho m_\rho\frac{1}{3}(\epsilon^{(\lambda)}_\rho p_\mu p_\nu + \epsilon^{(\lambda)}_\mu p_\nu p_\rho + \epsilon^{(\lambda)}_\nu p_\rho p_\mu)\\
& & (4.17)
\end{aligned}$$

## 4.1 Conformal Expansion

An alternative description of the DAs can be achieved through exploiting the conformal symmetry exhibited by massless QCD at tree level [35]. A close analogy to the conformal expansion is provided by a partial wave expansion of non-relativistic quantum mechanics in a spherically symmetric potential [36]. The $O(3)$ symmetry allows the separation of the angular, described by spherical harmonics, and radial degrees of freedom, which are thus governed by a one-dimensional Schrödinger equation. The wavefunction can therefore be expanded in terms of its spherical harmonics ordered by their orbital angular momentum [37].

$$\psi(r,\theta,\phi) \to R(r)\sum_{m,l} Y^l_m(\theta,\phi). \tag{4.18}$$

Similarly, the conformal symmetry allows the separation of the longitudinal degrees of freedom (momentum fractions), contained in the orthogonal Gegenbauer polynomials $C^{3/2}_n(x)$ [35], from the transverse degrees of freedom, which appear as the Gegenbauer coefficients, $a_n(\mu)$. The detailed argument to demonstrate this is technical and is not reproduced here, but may be found in [38]. The distribution amplitude can then be given as an expansion in Gegenbauer polynomials,

$$\phi(x,\mu) = 6x(1-x)\left(1+\sum_{n=1}^{\infty} a_n(\mu) C_n^{3/2}(2x-1)\right). \tag{4.19}$$

The Gegenbauer coefficients contain the non-perturbative information from the distribution amplitude and renormalise multiplicatively (to leading order accuracy)

$$a_n(\mu) = \left(\frac{\alpha_s(\mu)}{\alpha_s(\mu_0)}\right)^{\gamma_n^{(0)}/b_0} a_n(\mu^0), \qquad b_0 = \frac{11}{3}N_c - \frac{2}{3}N_f. \tag{4.20}$$

The anomalous dimension at this order is given by

$$\gamma_n^{(0)} = C_F\left(1 - \frac{2}{(n+1)(n+2)} + 4\sum_{m=2}^{n+1}\frac{1}{m}\right) \tag{4.21}$$

which is positive and increases in magnitude with increasing conformal spin. Therefore as $\mu \to \infty$, large $Q^2$ for our application, the coefficients become increasingly damped for increasing conformal spin and the distribution amplitudes tend to the asymptotic limit

$$\phi(x,\mu\to\infty) = \phi_{\mathrm{as}}(x) = 6x(1-x). \tag{4.22}$$

The Gegenbauer moments can be related to the ordinary moments,

$$a_1 = \frac{5}{3}\langle\xi^1\rangle, \tag{4.23}$$

$$a_2 = \frac{7}{12}(5\langle\xi^2\rangle - 1), \tag{4.24}$$

and so we can also determine the Gegenbauer moments on the lattice. This is particularly useful for a comparison to alternative methods such as the QCD sum rules which use the conformal expansion in their calculation of the Gegenbauer moments.

## 4.2 Existing Results

There are three main approaches for extracting the PDAs, which I will now discuss.

### 4.2.1 QCD Sum Rule Calculations

These use the Gegenbauer moments that arise from the conformal spin approach detailed above, for which representative results for the kaon first moment include:

$$a_1^K(1\text{ GeV}) = \begin{cases} 0.05(2)\ [39] \\ 0.10(12)\ [40] \\ 0.050(25)\ [41] \\ 0.06(3)\ [42] \\ 0.10(4)\ [43] \end{cases} \tag{4.25}$$

These results demonstrate the expected sign, but have large uncertainties of approximately 50%. The sum rule approach has an irreducible error of $\sim 20\%$ associated with it because the hadronic states cannot be completely isolated, unlike LQCD where we are able to take the limit of large Euclidean time so that the excited state contributions decay away.

### 4.2.2 Extraction from Experiment

In addition to the calculation of the distribution amplitudes on the lattice and through QCD sum rules it is possible to extract the DAs from experiment. The process $\gamma\gamma^* \to \pi_0$ is one of the simplest exclusive processes to which perturbation theory can be applied. Through a comparison of the pion-photon transition form-factor $F_{\pi\gamma}(Q^2)$, estimated in theory with the measured values, it is possible to extract information on the shape of the leading-twist pion distribution amplitude [44].

Experimental data for this process with $Q^2 < 3\text{GeV}^2$ was recorded in the early 1990's by the Cello collaboration [45]; later the Cleo collaboration provided results covering a broader range of $Q^2 \in [1.5, 9.2]\mathrm{GeV}^2$ [46], and more recently, the BaBar collaboration has added more precise results at both high and low energy regions in $Q^2 \in [4, 40]\mathrm{GeV}^2$ [47]. The experimental results for the high energy region contradict the asymptotic behaviour eq. (4.22) and instead suggest a distribution amplitude with a broader shape. The results could even be explained using a flat distribution amplitude, however this falls down for the small $Q^2$ behaviour. Currently, there is no definite conclusion on the pion distribution amplitude shape from experiment. It could take the asymptotic [29], Chernyak-Zhitnitsky [48], or even the flat form [49]. However, the results in [44] show that for $Q^2 \lesssim 15\mathrm{GeV}^2$ the asymptotic and broader forms for the DA can explain all the collaborations datasets with appropriate choices of parameters. For the new high $Q^2$ data from BaBar the conventional asymptotic form needs to be broadened in order to be consistent.

### 4.2.3 Lattice QCD

The calculation of the PDAs has not received as much attention as the pdfs. There has, however, been considerable work undertaken for both the meson and baryon PDAs. The first investigations were carried out by Martinelli and Sachrajda for the protons first and second moments in [50], as well as for the pions second moment in [51]. The latter of these initial calculations was performed on a $10^3 \times 20$ lattice using Wilson fermions in the quenched approximation. A value of $\langle \xi^2 \rangle = 0.26(13)$ was obtained, in the lattice renormalisation scheme at $a^{-1} = 1.8GeV$. The initial study of the PDAs by the RBC/UKQCD collaboration [52] obtained $\langle \xi^1 \rangle_K = 0.032(3)$ using $N_f = 2 + 1$ domain wall fermions for a $16^3 \times 32 \times 16$ lattice. In addition to our collaboration, there is a QCDSF/UKQCD calculation using $N_f = 2$ improved Wilson quarks [37]. Further to this the QCDSF collaboration have published results for the moments of baryon DAs [53]. A recent lattice review [54] details the lattice results for hadronic distribution amplitudes. In chapter 9 we compare the results from our lattice calculations to those obtained by other lattice collaborations.

# Chapter 5

# Chiral Perturbation Theory

Chiral Perturbation Theory is a very useful tool for our lattice calculations. It provides a way to constrain the form of the extrapolations required to link the lattice simulations at unphysical quark masses to the physical limit. Chiral symmetry is an approximate global symmetry of the QCD Lagrangian, which results from the u and d (and s) quark masses being small when compared to the typical QCD scale, $\Lambda_{QCD}$. Neglecting the explicit quark masses the QCD Lagrangian is invariant under separate left and right $SU(N_f)_{L,R}$ transformations. Based on this symmetry alone we would expect a corresponding degeneracy in the QCD spectrum. This parity doubling of even- and odd-parity hadrons is, however, not observed. The chiral symmetry must, therefore, be spontaneously broken. The order parameter for this is the chiral condensate, $\langle \overline{q}q \rangle$. Should the chiral symmetry be intact, the chiral condensate would vanish; however, when the symmetry is broken, $\langle \overline{q}q \rangle \neq 0$.

Goldstone's theorem tells us that when a continuous global symmetry is broken, massless Goldstone bosons appear in the spectrum. For the breaking of $SU(N_f)_L \times SU(N_f)_R$ to $SU(N_f)_V$, we expect $N_f^2 - 1$ Goldstone bosons. For $N_f = 2$ these are identified with the pions: $\pi^+$, $\pi^0$ and $\pi^-$ and for $N_f = 3$ there are, in addition to the pions, the kaons: $K^+$, $K^0$, $\overline{K}^0$, $K^-$ and the $\eta$ meson [55]. The Goldstone bosons are the lightest particles in the QCD spectrum and therefore determine the dynamics at low energies. It is therefore natural to build a low energy effective theory in terms of the Goldstone boson fields.

## 5.1 Constructing The Chiral Lagrangian

The symmetry group $G = SU(N_f)_L \times SU(N_f)_R$ is broken to the $H = SU(N_f)_V$ symmetry group via the condensate, where the Goldstone bosons can be identified with the fields in the coset space $G/H$, which is isomorphic to $SU(3)$ [56]. The Goldstone bosons can therefore be represented as special unitary matrices, $\Sigma(x)$, which transform under chiral rotations as

$$\Sigma(x) \to U_L \Sigma(x) U_R^\dagger. \tag{5.1}$$

The standard choice for the field is to use the exponential of the Goldstone boson fields, which transforms simply under $G$, whereas the Goldstone bosons themselves have a more complicated non-linear transformation under $G$.

$$\Sigma(x) = \exp(2i\pi^a(x)T^a/f), \qquad a = 1, ..., 8, \tag{5.2}$$

where the group generators are normalised $\mathrm{Tr}T^aT^b = \delta^{ab}/2$ and $f$ is a low energy constant which is equal to the decay constant $f_\pi$ at lowest order in chiral perturbation theory. For $N_f = 3$, the $T^a$ are related to the Gell-Mann matrices ($T^a = \lambda^a/2$)

$$\pi(x) = \sum_{a=1}^{8} \pi^a(x)T^a = \frac{1}{\sqrt{2}} \begin{bmatrix} \frac{1}{\sqrt{2}}\pi^0 + \frac{1}{\sqrt{6}}\eta & \pi^+ & K^+ \\ \pi^- & -\frac{1}{\sqrt{2}}\pi^0 + \frac{1}{\sqrt{6}}\eta & K^0 \\ K^- & \overline{K}^0 & -\frac{2}{\sqrt{6}}\eta \end{bmatrix} \tag{5.3}$$

and for $N_f = 2$, the $\sigma^a$ are the Pauli matrices

$$\pi(x) = \sum_{a=1}^{3} \pi^a(x)\frac{\sigma^a}{2} = \frac{1}{\sqrt{2}} \begin{bmatrix} \frac{1}{\sqrt{2}}\pi^0 & \pi^+ \\ \pi^- & -\frac{1}{\sqrt{2}}\pi^0 \end{bmatrix}. \tag{5.4}$$

We have, thus far, ignored the explicit symmetry breaking from the mass term in the QCD Lagrangian, which enters through the mass matrix

$$M = \begin{bmatrix} m_u & 0 & 0 \\ 0 & m_d & 0 \\ 0 & 0 & m_s \end{bmatrix} = M^\dagger. \tag{5.5}$$

The chiral symmetry of the QCD Lagrangian can, however, be retained by treating $M$ as a spurion field which transforms as

$$M \to U_L M U_R^\dagger. \tag{5.6}$$

Building the effective Lagrangian with these spurion fields provides an easy way of keeping track of the symmetry breaking caused by the mass term [57]. The fields $\Sigma$, $\Sigma^\dagger$, $M$ and $M^\dagger$ can then be used to construct the effective chiral Lagrangian. Terms will necessarily transform solely under the left-handed or right-handed subgroups and are therefore combined into separate traces to make them invariant under $G$. The most general term with no derivatives and no mass contributions is of the form $\mathrm{Tr}\Sigma\Sigma^\dagger...\Sigma\Sigma^\dagger$, where $\Sigma$ and $\Sigma^\dagger$ alternate. However, because $\Sigma^\dagger\Sigma = 1$ these are constant. Lorentz (Euclidean) invariance rules out terms with a single derivative [56]. It follows that the only independent term with two derivatives is

$$\mathrm{Tr}\partial_\mu\Sigma\partial^\mu\Sigma^\dagger \tag{5.7}$$

and the only term with no derivatives and one mass insertion is

$$\mathrm{Tr}\left(\Sigma^\dagger M + M^\dagger\Sigma\right). \tag{5.8}$$

There are, of course, other terms involving four derivatives, two derivatives and one mass insertion, etc., which all appear in the effective Lagrangian, each with independent unknown coefficients. As this effective theory is non-renormalisable there are, in fact, infinitely many terms [55]. A systematic method is therefore required to order these in terms of the size of their contributions to physical processes. Power counting provides this ordering and determines the scale, $\Lambda \sim 4\pi f_\pi = 1200\text{MeV}$, at which chiral perturbation theory breaks down [57]. When $p^2/\Lambda^2 = 1$, all the terms become equal in magnitude and there is no longer a suppression of the higher order terms. At leading order - adopting the standard power counting, whereby the lowest order terms in the chiral expansion are those with the fewest derivative operators and where two derivatives are counted for each spurion field - we have

$$\mathcal{L}_\chi^2 = \frac{f}{4}\text{Tr}\,(\partial_\mu \Sigma \partial^\mu \Sigma) - \frac{f^2 B_0}{2}\text{Tr}(M\Sigma^\dagger + \Sigma M^\dagger), \tag{5.9}$$

with the usual low energy constants, $f$ and $B_0$, associated with chiral perturbation theory. The quark masses are required to be small as the mass term breaks the chiral symmetry. Small means, by one definition the QCD scale, $m_q \ll \Lambda_{QCD} \sim 300\text{MeV}$ or, more exactly, from the chiral perturbation criterion $m_{\pi,K,\eta} \ll \Lambda$ [57]. As one would expect, we therefore see that $SU(2)_L \times SU(2)_R$ is a very good approximate symmetry, $(m_u + m_d)/2 \sim$MeV whereas $SU(3)_L \times SU(3)_R$ is more badly broken as $m_s \sim$100MeV. A number of current lattice simulations worldwide have shown that using $SU(2)_L \times SU(2)_R$ is very worthwile, since we can now tune $m_s$ to be almost correct and then take advantage of the much better $SU(2)_L \times SU(2)_R$ symmetry.

It is interesting to study the pion properties through inserting eq. (5.2) into eq. (5.9) and expanding to 2nd order in the pions. The mass term becomes

$$\mathcal{L}_m = -B\text{Tr}(M\pi^2), \tag{5.10}$$

substituting eq.(5.5) and eq.(5.3) for $M$ and $\pi$, we obtain the following predictions from chiral perturbation theory for the quark-meson mass relations,

$$\begin{aligned} m_{\pi^\pm}^2 &= B(m_u + m_d), && (5.11)\\ m_{K^\pm}^2 &= B(m_u + m_s), && (5.12)\\ m_{K^0}^2 &= B(m_d + m_s). && (5.13) \end{aligned}$$

The $\pi^0$ and $\eta$ mix, however, to first order in the isospin breaking parameter $m_u - m_d$,

$$
\begin{aligned}
m_{\pi^0}^2 &= B(m_u + m_d), && (5.14)\\
m_{\eta}^2 &= \frac{B}{3}(m_u + m_d + 4m_s). && (5.15)
\end{aligned}
$$

These relations are of the characteristic form $m_\Pi^2 \propto m_q$ associated with spontaneously broken symmetries. For our lattice simulations we work with degenerate $u$ and $d$ quarks, for which eqs. (5.11) to (5.15) simplify further. The use of further chiral perturbation theory, described in chapters 8 and 9, coupled with the above quark-meson mass relations will help to guide extrapolations of our lattice results performed at unphysical quark masses to the physical mass limit.

# Chapter 6

# Lattice QCD

QCD is a non-perturbative theory in its low energy regime. Non-perturbative methods are therefore required to calculate observables and make predictions that allow comparisons with experiment. Lattice QCD (LQCD) provides a non-perturbative implementation that uses the path integral approach. In this chapter I discuss the lattice action used for our simulations. I also describe the use of (partially) twisted boundary conditions, which allow us fine control over the momenta used in calculating lattice correlation functions.

## 6.1 Euclidean Path Integral

The lattice prescription is formed as a Euclidean field theory, however we are more familiar in dealing with QFTs in Minkowski space. The Minkowski field theory with $(D-1)$ spatial dimensions and 1 temporal dimension can be connected to $D$-dimensional Euclidean field theory through an analytic continuation (Wick rotation) to imaginary time,

$$x_0 = t \quad \longrightarrow \quad -ix_4 = -i\tau \tag{6.1}$$

$$p_0 = E \quad \longrightarrow \quad ip_4. \tag{6.2}$$

It should be noted that this simple case only holds for single particle states where the pole can be avoided in the analytic continuation. The analytic continuation requires more thought for multi-particle states, such as $n$-particle scattering amplitudes, and is not necessarily possible.

The Euclidean path integral approach is based upon the Feynman functional integral partition function,

$$Z = \int \mathrm{D}A_\mu \mathrm{D}\psi \mathrm{D}\overline{\psi} e^{-S}, \tag{6.3}$$

where the action is defined as

$$S = \int \mathrm{d}^4 x \left[ \frac{1}{4} F_{\mu\nu} F^{\mu\nu} - \overline{\psi} M \psi \right], \tag{6.4}$$

$M = (\gamma_\mu D^\mu + m)$ is the Dirac operator and $\overline{\psi} M \psi$ implies a sum over quark flavours. The fermions, $\psi$, are represented by anti-commuting Grassmann variables, which can be integrated out, as the fermion action is linear in both $\psi$ and $\overline{\psi}$. The fermion part of the functional integral is then completely contained within the determinant of the Dirac operator, leaving the integral over the background gauge field configurations

$$Z = \int \mathrm{D}A_\mu \det M \exp\left( - \int \mathrm{d}^4 x \frac{1}{4} F_{\mu\nu} F^{\mu\nu} \right). \tag{6.5}$$

The implementation of Grassmann variables on the lattice is therefore avoided [58]. A common approximation that was made in the past, in order to save on the expense of computer simulations, was to set $\det(M) = \text{constant}$, known as quenching. This removes the possibility of including internal quark loops in the simulations. Fortunately improvements in algorithms and computing hardware have removed this restriction for current simulations. We can rewrite the action after the integration of the fermion fields as

$$\begin{aligned} \tilde{S} &= S_{\mathrm{Gauge}} + S_{\mathrm{Fermion}} && (6.6) \\ &= \int \mathrm{d}^4 x \frac{1}{4} F_{\mu\nu} F^{\mu\nu} - \log(\det M), && (6.7) \end{aligned}$$

In general, we want to be able to calculate results for physical observables:

$$\langle \mathcal{O} \rangle = \frac{1}{Z} \int \mathrm{D}A_\mu \mathcal{O} e^{-\tilde{S}} \tag{6.8}$$

where the operator $\mathcal{O}$ is a time ordered product of gauge and fermion fields. These correlation functions can be expressed via Wick's theorem in terms of fermion propagators on a given background field. The fermion propagators are related to the inverse of the Dirac operator

$$S(y, j, b; x, i, a) = \left(M^{-1}\right)^{y,j,b}_{x,i,a}. \tag{6.9}$$

The $i$ and $j$ indices are spin, $x$ and $y$ are position, and $a$ and $b$ are colour. The propagator in eq. (6.9) is for a quark of spin $i$ and colour $a$, from site $x$ to site $y$, with spin $j$ and colour $b$, and is given by the corresponding element in matrix $M$ [58].

Thus far, we have detailed the procedure should we be able to calculate these quantities analytically. In order to calculate the expectation values of physical observables, we will need to turn the problem of solving the non-perturbative relativistic QFT into a problem of numerical integration. To do this, we need to reduce the system to one that is finite, in order to get a finite dimensional integral, whilst preserving as many as possible of the defining properties of the original system, e.g. gauge invariance and chiral symmetry. Nielsen-Ninomoya provided a no-go theorem telling us that we cannot preserve chiral symmetry without introducing "doublers" - additional copies of the fermion fields from the discretisation [59]. The design of lattice actions is therefore a significant area of research. We will go into more detail for the gauge action and type of fermions that we use for our calculations in the following sections.

As part of the lattice prescription the system is discretised so that we only know the values of the fermion fields at the lattice sites, which are separated by the lattice spacing $a$ in each direction. This unavoidably introduces discretisation errors. The challenge then becomes to make the lattice spacing as large as possible whilst keeping these errors as small as possible. We thus have a trade-off between the lattice spacing and the total volume to match the number of points to the available computing resources. The discretisation errors are due to the following: the lattice replaces derivatives with approximate difference operators and it imposes an ultraviolet (UV) cut-off. We will expand upon each in turn. The derivative of a field at point $x_j$ is given by [60]:

$$\frac{\partial \phi(x_j)}{\partial x} = \Delta_x \phi(x_j) + \mathcal{O}(a^2), \tag{6.10}$$

where

$$\Delta_x(x) = \frac{\phi(x+a) - \phi(x-a)}{2a}. \tag{6.11}$$

It is possible to use alternative difference operators by considering the field at more lattice points in order to improve the accuracy to higher orders in $a$, with, of course, an additional cost in computer resources/time. The UV cut-off introduces errors because the shortest wavelength which can be modelled on the lattice is $\lambda_{min} = 2a$ and so quarks or gluons on the lattice with a momenta $p = 2\pi/\lambda$ greater than $\pi/a$ cannot be resolved on the lattice [61]. The process of discretisation introduces an extra parameter $a$. This is however a physical quantity, which acts as the UV regulator of the theory and must eventually be taken to zero in order to reach the continuum theory. We therefore see that LQCD is an example of a "bare" QFT, with an explicit UV regulator.

Even after discretisation, for an infinite volume there are infinitely many integration variables and we do not know how to evaluate this in general. After going to a finite volume we have a (hugely) multi-dimensional ordinary integral, which is amenable to numerical evaluation. The Euclidean action eq. (6.7) is real and bounded from below, and so the factor $e^{-S}$ can be treated as a probability weight for the generation of the background gauge configurations. The important configurations can be generated through Markov chain Monte Carlo integration and importance sampling, where the configurations are generated with probability of occurrence given by $e^{-S}$ [62]. It is, therefore, possible to provide a good approximation to the functional integral.

Given a set of background gauge field configurations, we want to calculate quark propagators on each background field configuration. This is done by inverting the now finite (after discretisation) Dirac operator numerically. This is one of the most expensive parts of the simulation, which becomes increasingly difficult as the quark mass is decreased. The eigenvalues of $M$ range between a fixed upper value and the quark mass. The ratio of the largest and smallest eigenvalues is the condition number, which becomes very large when the quark mass is small. The numerical determination of $\det M$ and $M^{-1}$ become prohibitively expensive as the condition number becomes large and therefore prevents running simulations at the physical light (up and down) quark masses. We therefore simulate with a range of un-physical light quark masses and extrapolate to the physical value (determined as described in section 6.8). This extrapolation can be guided by chiral perturbation theory (chapter 5).

For a given quark mass, the calculation of $\det(M)$ is more expensive than for $M^{-1}$ and as such $\det(M)$ is only calculated for a limited number of quark masses. After the determination of $\det(M)$ as part of the generation of the gauge field configurations, we have the freedom to choose $M^{-1}$ to have the same quark mass as $\det(M)$ (a unitary point) or to have a different, usually lighter quark mass (a partially quenched point).

The most straightforward calculation of correlation functions requires the propagator from a given source position to all other sites on the lattice. This corresponds to 12 columns of $M^{-1}$ one for each of the 12 spin and colour degrees of freedom [58]. Our numerical approximation to the full expectation values of the operators can then be evaluated through an average over the set of gauge configurations.

## 6.2 Gluon Fields in LQCD

We represent the gauge field $A_\mu(x)$ on the lattice with a link variable. The links are represented by $SU(3)$ matrices

$$U(x, x + a\hat{\mu}) = U_\mu(x) = \exp(iagA_\mu(x + a\hat{\mu}/2)). \tag{6.12}$$

$\hat{\mu}$ is a unit vector in one of the four space-time directions. $U_\mu(x)$ links sites at $x$ and $x + a\hat{\mu}$. The fields transform under local gauge transformations as,

$$\begin{aligned} \psi(x) &\rightarrow V(x)\psi(x) & (6.13)\\ \overline{\psi}(x) &\rightarrow \overline{\psi}(x)V^\dagger(x) & (6.14)\\ U_\mu(x) &\rightarrow V(x)U_\mu(x)V^\dagger(x + a\hat{\mu}) & (6.15)\end{aligned}$$

where $V(x)$ are $SU(3)$ matrices in the same representation as the fermion fields (i.e. the fundamental representation). We can construct two types of gauge invariant quantities on the lattice: an ordered string of links capped by a fermion and an anti-fermion at the ends, and a trace of a closed loop of links (Wilson loop) [58]. Examples of these are

$$\mathrm{tr}\left(\overline{\psi}(x)U_\mu(x)U_\nu(x + a\hat{\mu})...U_\rho(y - a\hat{\rho})\psi(y)\right), \tag{6.16}$$

and $\mathrm{tr}(P_{\mu\nu}(x))$ where

$$P_{\mu\nu}(x) = U_\mu(x)U_\nu(x + a\hat{\mu})U_\mu^\dagger(x + a\hat{\mu})U_\nu^\dagger(x). \tag{6.17}$$

$P_{\mu\nu}(x)$ is the smallest possible Wilson loop referred to as the plaquette [60]. A gauge invariant action can therefore be built from these quantities with the further limitation that it should reduce to the continuum action for $a \rightarrow 0$.

### 6.2.1 Wilson Action

The Wilson gauge action [63] is defined using the plaquette eq. (6.17)

$$S_W = \frac{1}{g^2}\sum_x \sum_{\mu<\nu} \mathrm{Re}[\mathrm{tr}(1 - P_{\mu\nu}(x))]. \tag{6.18}$$

It is easy to see that this is invariant under the transformations eqs. (6.13)-(6.15). Inserting eq. (6.12) into eq. (6.17) and expanding about the mid-point of the plaquette $x + a(\hat{\mu} + \hat{\nu})/2$ gives

$$P_{\mu\nu}(x) = 1 + iga^2 F_{\mu\nu}(x) - \frac{g^2 a^4}{2} F^2_{\mu\nu}(x) + ... \tag{6.19}$$

which translates to the Wilson gauge action

$$\begin{aligned} S_W &= a^4 \left( \sum_x \frac{1}{4} F^{b,\mu\nu}(x) F^b_{\mu\nu}(x) + \mathcal{O}(a^2) \right) && (6.20) \\ &\overset{a \,\to\, 0}{=} \int \mathrm{d}^4x \frac{1}{4} F^{b,\mu\nu}(x) F^b_{\mu\nu}(x). && (6.21) \end{aligned}$$

We observe two things: that the Wilson action reduces, as required, to the continuum case for $a \to 0$ and that lattice artefacts occur at $\mathcal{O}(a^2)$. This is, however, not a unique description, and as we will see there are other (gauge invariant) alternatives for which the artefacts occur at higher orders. The Iwasaki gauge action [64], which we employ for our simulations, is an example of this.

### 6.2.2 Iwasaki Action

The Iwasaki gauge action is an example of a gauge action which uses a linear combination of closed gauge loops.

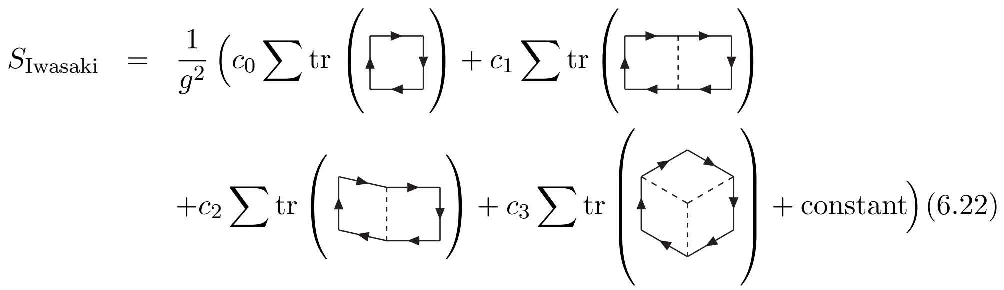

$$S_{\text{Iwasaki}} = \frac{1}{g^2}\Big( c_0 \sum \mathrm{tr}\left(\ \right) + c_1 \sum \mathrm{tr}\left(\ \right) + c_2 \sum \mathrm{tr}\left(\ \right) + c_3 \sum \mathrm{tr}\left(\ \right) + \text{constant}\Big) \tag{6.22}$$

where the sums are over the orientation of the loops, and the normalisation is such that $c_0 + 8c_1 + 16c_2 + 8c_3 = 1$. For the ensembles used in this work the constants $c_1 = c_2 = 0$ and $c_3 = -0.331$ which also defines $c_0$. This action was chosen because of the improvement in lattice artefacts (reducing discretisation errors) and because it reduces the residual chiral symmetry breaking which arises from the domain-wall fermion action [65].

It is conventional to use the inverse lattice coupling $\beta$ instead of the bare coupling constant $g^2$ for a lattice action with spacing $a$. For the Wilson and Iwasaki actions, $\beta = 2N_c/g^2$, where $N_c$ is the number of colours. The lattice spacing is not known a priori to a lattice calculation. Its value depends on the bare coupling constant. For example, in $SU(3)$ for the Iwasaki gauge action, $\beta \sim 2$ corresponds to $a \sim 0.1$fm. Larger values of $\beta$ correspond to finer lattices and smaller values to coarser lattices [66]. The bare lattice coupling may therefore be considered as at the scale $a^{-1}$. Details of the determination of $a$ are given in section 6.8.

## 6.3 Quark Fields in LQCD

In order to discretise the Dirac (fermion) action, we need to replace the derivative operator with the symmetrised difference operator

$$\overline{\psi} \not{D} \psi = \frac{1}{2a} \overline{\psi} \sum_{\mu} \gamma_\mu \left[ U_\mu(x)\psi(x + a\hat{\mu}) - U^\dagger_\mu(x - a\hat{\mu})\psi(x - a\hat{\mu}) \right], \tag{6.23}$$

where the appropriate gauge links are included to preserve gauge invariance. The continuum action must be recovered when $a \to 0$. This can be seen through a Taylor expansion in the gauge and fermion fields with respect to $a$, which also demonstrates that the discretisation errors occur at $\mathcal{O}(a^2)$.

### 6.3.1 Naïve Fermions

The simplest "Naïve" action written for a single flavour of fermion is

$$\begin{aligned} S_{\text{Naive}} &= m_q \sum_x \overline{\psi}(x)\psi(x) + \frac{1}{2a}\sum_x \overline{\psi}(x) \not{D}\, \psi(x) && (6.24) \\ &= \sum_x \overline{\psi}(x) M(x,y)\psi(y) && (6.25) \end{aligned}$$

where the $\gamma_\mu$ are the Euclidean gamma matrices, which are hermitian $\gamma_\mu = \gamma_\mu^\dagger$ and satisfy $\{\gamma_\mu, \gamma_\nu\} = 2\delta_{\mu\nu}$. $M(x,y)$ is the interaction matrix

$$M(x,y) = m_q \delta_{y,x} + \frac{1}{2a}\sum_{\mu=1}^{4}\left[\gamma_\mu U_\mu(x)\delta_{y,x+a\hat{\mu}} - \gamma_\mu U_\mu^\dagger(x)\delta_{y,x-a\hat{\mu}}\right] \tag{6.26}$$

This action preserves chiral symmetry, but suffers from the notorious "fermion doubling problem". This is illustrated by the free fermion propagator, $U_\mu(x) = 1$. Using a Fourier transform

$$\psi(x) = \int_{-\pi/a}^{\pi/a} \frac{\mathrm{d}^4 p}{(2\pi)^4} \tilde{\psi}(p) e^{ip.x}, \tag{6.27}$$

the action becomes

$$\tilde{S}_{\text{Naive}} = \int_{-\pi/a}^{\pi/a} \frac{\mathrm{d}^4 p}{(2\pi)^4} \tilde{\overline{\psi}}(-p)\left[i\gamma_\mu \bar{p}_\mu + m_q\right]\tilde{\psi}(p) \tag{6.28}$$

where

$$\bar{p}_\mu = \frac{1}{a}\sin(ap_\mu). \tag{6.29}$$

The free quark propagator is then

$$G(p) = M^{-1}(p) = \left(i\sum_\mu \gamma_\mu \bar{p}_\mu + m_q\right)^{-1}, \tag{6.30}$$

where we see that there are poles at $p_\mu = \pm\pi/a$ (for $m_q \ll p_\mu$) in addition to the poles at $p_\mu = 0$ that exist in the continuum theory. This is, therefore, describing $2^d$ fermions, where $d = 4$ is the number of dimensions. There are prescriptions that remove these additional undesirable modes. We will describe two of them: Wilson fermions and domain-wall fermions.

### 6.3.2 Wilson Fermions

In order to remove the additional 15 species, Wilson introduced an irrelevant dimension-5 operator, a second derivative-like term, where the extra species at $p_\mu = \pm\pi/a$ become very heavy as $a \to 0$. The Wilson fermion action is

$$\begin{aligned} S_{\text{Wilson}} &= S_{\text{Naive}} - \frac{r}{2a}\sum_x \sum_{\mu=1}^{4} \overline{\psi}(x)\left[U_\mu(x)\psi(x+a\hat{\mu}) - 2\psi(x) + U_\mu^\dagger(x-a\hat{\mu})\psi(x-a\hat{\mu})\right] \\ &= \frac{1}{2a}\sum_x \overline{\psi}(x)\left[(\gamma_\mu - r)U_\mu(x)\psi(x+a\hat{\mu}) - (\gamma_\mu + r)U_\mu^\dagger(x-a\hat{\mu})\psi(x-a\hat{\mu})\right] \\ &+ \frac{m_f a + 4r}{a}\sum_x \overline{\psi}(x)\psi(x) \\ &= \sum_{x,y} \overline{\psi}(x) M_W(x,y)\psi(y) \end{aligned} \tag{6.31}$$

where r is the Wilson parameter $0 \le r \le 1$, and

$$\begin{aligned} M_W(x,y) &= -\frac{1}{2}\sum_{\mu=1}^{4}\left[\left(\frac{r}{a} - \gamma_\mu\right)U_\mu(x)\delta_{y,x+a\hat{\mu}} + \left(\frac{r}{a} + \gamma_\mu\right)U_\mu^\dagger(x)\delta_{y,x-a\hat{\mu}}\right] \\ &+ \left(m_q + \frac{4r}{a}\right)\delta_{x,y}. \end{aligned} \tag{6.32}$$

Considering the free field fermion propagator, $U_\mu(x) = 1$,

$$G(p) = M_W^{-1} = \left(i\sum_\mu \gamma_\mu \bar{p}_\mu + m_q + \frac{2r}{a}\sum_\mu \sin^2\frac{ap_\mu}{2}\right)^{-1}. \tag{6.33}$$

We see that we have the usual pole at $p_\mu = 0$. However for, $p_\mu = \pm\pi/a$, the last term in eq. (6.33) diverges for $a \to 0$. The masses for the $p_\mu = \pm\pi/a$ modes therefore become increasingly heavy (and comparable to the cut-off $\mathcal{O}(1/a)$ for $a \to 0$) and hence disappear in the continuum limit. This is, however, done at the cost of losing chiral symmetry at non-zero lattice spacing. The new Wilson term (first line eq. (6.31)) is of the type $\overline{\psi}(x)\psi(x)$ which breaks the chiral symmetry. The Nielsen and Ninomiya [59] no-go theorem suggested that a lattice action cannot preserve both chiral-symmetry and be un-doubled. This however can be bypassed by modifying the definition of a chiral rotation on the lattice to

$$\psi \rightarrow \exp\left(i\epsilon\gamma_5\left(1-aD\right)\right)\psi, \tag{6.34}$$

$$\overline{\psi} \rightarrow \overline{\psi}\exp\left(i\epsilon\left(1-aD\right)\gamma_5\right). \tag{6.35}$$

which becomes the usual transformation in the limit $a \rightarrow 0$. $D$ is the Dirac operator used in the action, however, the requirement that the Langrangian is unaltered by chiral-rotations, $\delta\mathcal{L} = 0$, leads to a new commutation relation,

$$\gamma_5 D + D\gamma_5 = 2aD\gamma_5 D \tag{6.36}$$

known as the Ginsparg-Wilson relation [67]. This coupled with the modified chiral rotations allow for un-doubled chiral fermions.

### 6.3.3 Domain-wall Fermions

The Domain-wall fermion prescription for the description of chiral fermions on the lattice originated with ideas by Kaplan [68], which were developed into the method which we use in this work by Shamir [69]. In the continuum (a system with no discretisation and no finite volume effects), domain-wall fermions are constructed with Dirac fermions in five dimensions, with a mass term that depends on the fifth dimensional coordinate, $s$. This mass term is chosen to be a step function, which results in a single massless fermion of a given chirality bound to the mass defect (this chiral mode decays exponentially in $s$ in the fifth-dimension).

This idea transfers to the discrete lattice and if a Wilson term is included to remove the usual lattice doublers, we have a description that is both chiral and un-doubled. For the lattice implementation, we introduce Dirichlet boundary conditions at either end of the fifth-dimension at $s = 0$ and $s = L_s - 1$, where $L_s$ is the extent of the fifth-dimension. The boundary conditions are chosen so that opposite chiral modes live on the two boundaries. There will be an overlap between the two chiral modes because they decay exponentially away from the boundaries. The resulting chiral symmetry breaking is governed by the size of $L_s$. At leading order, the residual chiral symmetry breaking due to the overlap is given by the additive quark mass renormalisation $m_{\text{res}}$. At finite $L_s$, the Ginsparg-Wilson condition eq. (6.36) does not hold exactly, but is recovered for $L_s \to \infty$. There is, hence, a compromise to make between the degree of chiral symmetry and the additional cost of simulating with an increasingly large fifth dimension. The five-dimensional domain-wall fermion action is given by,

$$S_{\text{DW}} = -\sum_{x,x',s,s'} \overline{\Psi}(x,s) M_{\text{DW}}(x,s;x',s') \Psi(x',s') \tag{6.37}$$

where the fifth dimension is labelled by $s$, which runs from 0 to $L_s - 1$ and $\overline{\Psi}(x,s)$ and $\Psi(x,s)$ are the five-dimensional fermion fields and are related to the four-dimensional fermion fields

$$\begin{aligned} \psi(x) &= (1-\gamma_5)\,\Psi(x,0) + (1+\gamma_5)\,\Psi\left(x, L_s - 1\right), & (6.38)\\ \overline{\psi}(x) &= \overline{\Psi}\left(x, L_s - 1\right)(1-\gamma_5) + \overline{\Psi}(x,0)\,(1+\gamma_5)\,. & (6.39) \end{aligned}$$

The matrix $M_{\text{DW}}(x,s;x',s')$ consists of two parts: $D^{\|}(x,x')$ which is in four-dimensions and is in fact the Wilson action with $r = 1$ and a negative mass $M^5$, referred to as the Domain wall height, and $D^{\perp}(s,s')$ which is in the extra fifth dimension. $m_f$ is the four-dimensional bare quark mass which breaks the chiral symmetry. This is seen in eq. (6.42) as it explicitly couples the $s = 0$ and $s = L_s - 1$ domain-walls.

$$M_{\text{DW}}(x,s;x',s') = \delta_{s,s'} D^{\|}(x,x') + \delta_{x,x'} D^{\perp}(s,s') \tag{6.40}$$

$$\begin{aligned} D^{\|}(x,x') &= \frac{1}{2}\sum_{\mu=1}^{4}\Big[(1-\gamma_\mu)\,U_\mu(x)\delta_{x+\hat{\mu},x'} + (1+\gamma_\mu)\,U_\mu^\dagger(x')\delta_{x'+\hat{\mu},x}\Big] \\ &+ (M_5 - 4)\,\delta_{x,x'} & (6.41)\\ D^{\perp}(s,s') &= \left[(1-\gamma_5)\,\delta_{s+1,s'} + (1+\gamma_5)\,\delta_{s-1,s'} - 2\delta_{s,s'}\right] \\ &- m_f\left[(1-\gamma_5)\,\delta_{s,L_s-1}\delta_{0,s'} + (1+\gamma_5)\,\delta_{s,0}\delta_{L_s-1,s'}\right] & (6.42) \end{aligned}$$

## 6.4 Twisted Boundary Conditions

Twisted boundary conditions allow us to finely tune the momenta used in calculating correlation functions. The initial study into using twisted boundary conditions for quark fields was performed by Bedaque in [70]. This was developed into the form that is used for our calculations (specifically partially twisted boundary conditions) in [71] and was later studied numerically on the lattice to investigate its applicability for calculations [72]. They have now become widely used in $K_{l3}$ and pion form factor calculations [73].

In a system of finite size the boundary conditions determine the spectrum of available momenta. The effect of the boundary conditions is to quantise the momenta. A popular choice are periodic boundary conditions,

$$\phi(x_i + L) = \phi(x_i) \qquad i = 1, 2, 3, \tag{6.43}$$

which through a Fourier transform become,

$$\int \phi(p) e^{-ip(x+L)} \mathrm{d}^4 p = \int \phi(p) e^{-ipx} \mathrm{d}^4 p. \tag{6.44}$$

The periodic boundary conditions therefore correspond to the quantised momenta

$$e^{ip_i L} = 1 \Rightarrow p_i = \frac{2\pi n_i}{L} \qquad i = 1, 2, 3, \tag{6.45}$$

Extending this to a generalised set of boundary conditions, that depend upon a three vector $\theta$,

$$\phi(x_i + L) = e^{i\theta_i} \phi(x_i) \qquad i = 1, 2, 3, \tag{6.46}$$

we now see that

$$e^{i(p_i - \theta_i / L)L} = 1 \Rightarrow p_i = \frac{\theta_i}{L} + \frac{2\pi n_i}{L} \qquad i = 1, 2, 3. \tag{6.47}$$

The momenta are still quantised, as for the periodic case, but they are shifted by a factor $\theta$ which is tunable and a continuous range of momenta is now accessible. For a meson composed of a quark twist angle $\theta_1$ and anti-quark of twist angle $\theta_2$ the momentum is

$$p = \frac{2\pi}{L}n - \frac{\theta_1 - \theta_2}{L}, \tag{6.48}$$

with dispersion relation

$$E_p^2 = m_p^2 + \left(\frac{2\pi}{L}n - \frac{\theta_1 - \theta_2}{L}\right)^2. \tag{6.49}$$

For our lattices $2\pi/(La)$ is rather large ($\sim$ 500 MeV) and so the momentum resolution is not that great, twisting provides a technique for improving this otherwise restrictive momentum resolution from periodic boundary conditions. This property can equivalently be achieved through applying a constant background vector field which couples to the quark fields with a charge determined by the twist angle. This is the method which is used in practice for our simulations. This allows us to calculate twisted propagators by transforming the gauge links and then performing our standard inversions using the transformed gauge field. As for the periodic boundary conditions, the finite volume effects must be considered. For the general case of twisted boundary conditions (any $\theta$), the finite volume effects were studied using chiral perturbation theory with a background field in [71], where it was found that processes without any final state interactions (such as matrix elements of local operators with either vacuum and/or single hadron external states) have finite volume effects that are exponentially suppressed by the volume ($\sim e^{-m_P L}$). This is the same as for periodic boundary conditions, which is not surprising as the periodic boundary conditions are just a special case where $\theta = 0, 2\pi, ....$

Whilst twisted boundary conditions' use for generating arbitrary hadronic momenta is extremely favourable, every choice of twist angle (boundary condition), in principle, requires the generation of a new set of gauge field configurations, which would make this method prohibitively expensive. Partially twisted boundary conditions avoid this problem by only applying the twist angles to the valence quark fields and using periodic boundary conditions for the sea quark fields [71, 74]. This does, however, break the sea-valence symmetry, which is a finite volume effect.

Applying different twist angles to the $u$- and $d$-quark fields breaks isospin symmetry and applying different twist angles in different directions also breaks the cubic symmetry. However, as in [71], it is expected that, for most physical quantities with at most a single hadron in the initial or final states, the finite volume effects are exponentially suppressed by the volume, which is the case for this work. This breaking is considered to be analogous to the violation of unitarity in partially quenched LQCD [71]. Matrix elements with multi-particle states are more complicated and involve both exponential and power finite volume corrections.

## 6.5 Correlation Functions

In order to calculate observables, we will need to consider vacuum expectation values of operators or, equally, correlation functions. For example, the two-point correlation function is constructed as

$$\langle 0| T \left[ \sum_x \mathcal{O}_f(x,t) \mathcal{O}_i(0,0) \right] |0\rangle \qquad t > 0. \tag{6.50}$$

Let us consider the case of the pion for which we may choose,

$$\mathcal{O}_i(x,t) = \mathcal{O}_f(x,t) = A_4(x,t) = \overline{\psi}(x,t)\gamma_4\gamma_5\psi(x,t). \tag{6.51}$$

These operators possess the correct quantum numbers to create a pion at the origin and annihilate it at position $x$ at time $t$. These operators will, however, also produce all other eigenstates of the Hamiltonian with the same quantum numbers as the pion, and so it is, in fact, a linear combination of states that is created and annihilated. We can rewrite eq. (6.50) using $\mathcal{O}_i(x,t) = e^{i(\hat{\mathbf{p}}.\mathbf{x} - \hat{p}_4 t)}\mathcal{O}(0)e^{-i(\hat{\mathbf{p}}.\mathbf{x} - \hat{p}_4 t)}$, where $\hat{p}$ is the energy-momentum operator and where we also insert a complete set of states

$$\langle 0| T \left[ \sum_x \mathcal{O}_f(x,t) \mathcal{O}_i(0,0) \right] |0\rangle = \sum_n \frac{\langle 0|\mathcal{O}_f|n\rangle\langle n|\mathcal{O}_i|0\rangle}{2E_n} e^{-E_n t} \tag{6.52}$$

The $\sum_x$ projects out the zero momentum states, and so we can read $E_n$ as $M_n$. We explicitly see the sum over all states, $n$, that contribute to the amplitude. The factor $e^{-E_n t}$ will suppress states with large energies (or mass at zero momentum) at large Euclidean times [61]. Thus, if we wait for a sufficiently large time, the pion state will be isolated. We can also improve the overlap of the operator with the pion state (or any state of interest) and hence the quality of our signal by making a suitable choice of operator that limits the number of states in the linear combination. Such an operator will be more complicated than those in this example and is likely to be de-localised or "smeared".

## 6.6 Calculation of Bare Moments from Lattice Correlation Functions

In chapters 8 and 9 we will calculate the PDAs and structure functions from their moments (eq. (4.14)-(4.17) and eq. (3.15)). In order to do so, we will require expressions in terms of Euclidean lattice correlation functions, which are obtainable through Monte Carlo integration of the Euclidean QCD path integral. If we consider a generic meson with valence quark content $\overline{q}_1 q_2$, where $q_x \in \{q, s\}$ (and $q = u = d$), we have the following constructions of the pseudoscalar, vector and axial interpolating operators respectively:

$$\begin{aligned} P(x) &\equiv \overline{q}_2(x)\gamma_5 q_1(x), & (6.53)\\ V_\mu(x) &\equiv \overline{q}_2(x)\gamma_\mu q_1(x), & (6.54)\\ A_\mu(x) &\equiv \overline{q}_2(x)\gamma_\mu\gamma_5 q_1(x). & (6.55)\end{aligned}$$

For the lattice calculation, it is also necessary to write the double-headed covariant derivative contained in eqs. (4.14)-(4.17) as lattice difference operators:

$$\begin{aligned} \overrightarrow{D}_\mu \psi(x) &= \frac{1}{2a}\left[U(x, x + a\hat{\mu})\psi(x + a\hat{\mu}) - U(x, x - a\hat{\mu})\psi(x - a\hat{\mu})\right], & (6.56)\\ \overline{\psi}(x)\overleftarrow{D}_\mu &= \frac{1}{2a}\left[\psi(x + a\hat{\mu})U(x + a\hat{\mu}, x) - \psi(x - a\hat{\mu})U(x - a\hat{\mu}, x)\right]. & (6.57)\end{aligned}$$

These derivatives are used in the following operators with which we extract the moments:

$$\begin{aligned}
\mathcal{O}_{\{\rho\mu\}}(x) &\equiv \overline{q}_2(x)\gamma_{\{\rho}\overleftrightarrow{D}_{\mu\}}q_1(x), & (6.58)\\
\mathcal{O}_{\{\rho\mu\nu\}}(x) &\equiv \overline{q}_2(x)\gamma_{\{\rho}\overleftrightarrow{D}_{\mu}\overleftrightarrow{D}_{\nu\}}q_1(x), & (6.59)\\
\mathcal{O}^5_{\{\rho\mu\}}(x) &\equiv \overline{q}_2(x)\gamma_{\{\rho}\gamma_5\overleftrightarrow{D}_{\mu\}}q_1(x), & (6.60)\\
\mathcal{O}^5_{\{\rho\mu\nu\}}(x) &\equiv \overline{q}_2(x)\gamma_{\{\rho}\gamma_5\overleftrightarrow{D}_{\mu}\overleftrightarrow{D}_{\nu\}}q_1(x), & (6.61)
\end{aligned}$$

where the braces indicate a symmeterisation of the enclosed Lorentz indices, $\{\mu_1 ... \mu_n\} \equiv \frac{1}{n!}\sum_{\text{permutations } s} \mu_{s(1)}...\mu_{s(n)}$.

## 6.7 Mixing of Lattice Operators

The analytic continuation that is used in going from Minkowski to Euclidean space alongside the discretisation of space-time, required to formulate QCD on the lattice, replaces the familiar Lorentz group with the hypercubic group $H(4)$. The lattice operators should therefore be classified according to their behaviour under the $H(4)$ group consisting of reflections and $\pi/2$ rotations, and under the discrete symmetries, parity $P$ and charge conjugation $C$. Unfortunately, this leads to increased possibilities for operator mixing compared to the continuum.

We would, of course, like to avoid mixing with lower dimensional operators wherever possible. This is achievable, to some extent, through careful choices of the operators' indices. We must, however, also bear in mind that we pay for every additional non-vanishing momentum component used with a degradation of the statistical signal.

The operators $\mathcal{O}_{\{\rho\mu\}}(x)$ and $\mathcal{O}^5_{\{\rho\mu\}}(x)$ for $\rho \neq \mu$, transform, in the notation of [75], under the six dimensional $6^-$ and $6^+$ irreducible representations of $H(4)$. This, alongside charge conjugation, ensures that for these operators there is no mixing with equal or lower dimensional operators. We may also consider $\mathcal{O}_{\mu\mu}(x)$ and $\mathcal{O}^5_{\mu\mu}(x)$, which transform as four-dimensional reducible representations that contain a singlet, and three traceless operators:

$$\frac{1}{2}\left(\mathcal{O}_{11}^{(5)}+\mathcal{O}_{22}^{(5)}-\mathcal{O}_{33}^{(5)}-\mathcal{O}_{44}^{(5)}\right), \tag{6.62}$$

$$\frac{1}{\sqrt{2}}\left(\mathcal{O}_{33}^{(5)}-\mathcal{O}_{44}^{(5)}\right), \tag{6.63}$$

$$\frac{1}{\sqrt{2}}\left(\mathcal{O}_{11}^{(5)}-\mathcal{O}_{22}^{(5)}\right), \tag{6.64}$$

which transform as the three-dimensional irreducible representation $(3,1)^-$ and $(3,1)^+$ for the operator with- and without-$\gamma_5$ respectively. We can construct an operator which involves the subtraction of a trace term in order to avoid mixing with the singlet (proportional to $1/a(\overline{\psi}\psi)$),

$$\mathcal{O}_{44}^{(5)}-\frac{1}{3}\left(\mathcal{O}_{11}^{(5)}+\mathcal{O}_{22}^{(5)}+\mathcal{O}_{33}^{(5)}\right), \tag{6.65}$$

but this, in principle, involves the subtraction of a power divergence, which may lead to large numerical cancellations and hence large statistical errors.

The second moments, $\mathcal{O}_{\{\rho\mu\nu\}}(x)$ and $\mathcal{O}^5_{\{\rho\mu\nu\}}(x)$, with distinct and different indices, transform as the $\overline{(1/2,1/2)}^+$ and $\overline{(1/2,1/2)}^-$ four-dimensional irreducible representations respectively. Unfortunately, charge conjugation allows the operators $\mathcal{O}_{\{\rho\mu\nu\}}(x)$ and $\mathcal{O}^5_{\{\rho\mu\nu\}}(x)$ to mix with total derivative terms

$$\partial_{\{\rho}\partial_{\mu}\left(\overline{q}_2(x)\gamma_{\nu\}}\gamma_5 q_1(x)\right) \quad \text{and} \quad \partial_{\{\rho}\partial_{\mu}\left(\overline{q}_2(x)\gamma_{\nu\}}q_1(x)\right) \tag{6.66}$$

respectively. It is necessary to calculate these terms for the distribution amplitude calculation because it involves non-forward matrix elements, for which the total derivative terms are non-zero.

A detailed investigation of the operator mixing under the hypercubic $H(4)$ group for operators of the form eq. (6.58)-(6.61) was performed in [76].

## 6.8 Simulation parameters

The numerical calculations of the structure function and PDA moments, in the following sections, are based upon gauge field configurations taken from the joint data sets used in the broader RBC/UKQCD collaboration's domain-wall fermion phenomenology programme. The configurations were generated with $N_f = 2 + 1$ flavours of dynamical domain wall fermions and with the Iwasaki gauge action. The Rational Hybrid Monte Carlo (RHMC) algorithm [77] was used in order to benefit from its easy introduction of single-quark flavours (the strange-quark in our case). Other algorithms often require the fermions to occur in pairs (such as the HMC algorithm). RHMC also provides a reduction in the computation required for LQCD calculations over the HMC algorithm. The configurations were generated on QCDOC computers [78–80] running the Columbia Physics System (CPS) software [81] and the BAGEL [82, 83] assembler generator. Measurements for the calculations were performed using the UKHADRON software package that makes use of both the BAGEL DWF inverter [82, 83] and elements of the SciDAC software library stack, including the CHROMA LQCD library [84] and QDP++.

For the numerical calculations we use three different sets of lattice parameters. First, we have lattices with $16^3 \times 32$ and $24^3 \times 64$ points with a common lattice spacing $a^{-1} = 1.73(3)$GeV, thus allowing the study of finite volume effects. The bare gauge coupling $\beta = 2.13$ ($\beta = 6/g^2$ where $g$ is the bare lattice coupling, see section 6.2.2) is common to both lattices, as are the unitary masses: $am_s = 0.04$ (strange quark) and the range of light quark masses $am_l = 0.01$, 0.02 and 0.03. On the $24^3 \times 64$, ensemble there is an additional light quark mass $am_l = 0.005$. In order to study discretisation effects, the third $32 \times 64$ point lattice has a finer lattice spacing $a^{-1} = 2.28(3)$GeV. This ensemble has the bare gauge coupling $\beta = 2.25$ that is chosen alongside the number of points in order to construct a lattice with a volume comparable to the $24^3 \times 64$ ensemble. The available masses for this ensemble are the unitary (partially quenched) strange mass $am_s = 0.03$ (0.025) and the unitary light-quarks $am_l = 0.004$, 0.006 and 0.008. All of the datasets have a fifth dimension: $L_s a = 16$. The remnant chiral symmetry

| $a^{-1}$ (GeV) | $a$ (fm) | $am_{\rm res}$ | $a\tilde{m}_q$ | $a\tilde{m}_s$ | $a\tilde{m}_{ud} : a\tilde{m}_s$ |
|---|---|---|---|---|---|
| 1.729(28) | 0.1141(18) | 0.003152(43) | 0.001300(58) | 0.0375(16) | 1:28.8(4) |
| 2.221(29) | 0.08883(12) | 0.0006664(76) | 0.001040(31) | 0.0292(08) | 1:28.08(19) |

**Table 6.1:** *Lattice scale and physical unrenormalised quark masses in lattice units for both the* $24^3$ *(top row) and* $32^3$ *(bottom row) ensembles, where* $\tilde{m}_X \equiv m_X + m_{res}$ *[3].*

breaking, from the finite fifth dimension, requires the residual mass to be taken account of additively in the quark masses. The chiral symmetry breaking parameters for the $24^3 \times 64$ (and $16^3 \times 32$) and $32^3 \times 64$ ensembles are, in the chiral limit, $am_{res} = 0.00315(4)$ and $am_{res} = 0.00067(8)$ respectively.

The lattice scale $1/a$ and quark masses $m_q$, $m_s$ are not known a priori. They have to be determined through a comparison of lattice results for three quantities with the corresponding physical values. This was done in [3, 85]. The pseudoscalar masses, $m_\pi$ and $m_K$, are taken to be two of these. The final choice is the mass of the $\Omega$ baryon, a state composed of three valence strange-quarks. This choice has the advantage that there are no non-analytic light-quark mass terms at NLO in chiral perturbation theory [86, 87]. The three lattice parameters are determined iteratively, starting with a guess for the quark masses. These are then used to obtain the mass of the $\Omega$ through a chiral extrapolation, which is then set to its physical value through an adjustment in the lattice scale. The new lattice scale is used to adjust the quark masses by requiring $m_\pi$ and $m_K$ to take their physical values. This is repeated until the three parameters stabilise [85]. The values for $1/a$, $a$, $m_q$ and $m_s$, after their iterative determination, are given for the ensembles used in this calculation in table 6.1. The physical quark values $a\tilde{m}_q$ and $a\tilde{m}_s$ (table 6.1) are the points to which we must extrapolate in order to obtain physical results. The extrapolation for the $24^3$ ensemble to the physical point is performed using the following un-physical light-quark masses, which correspond to the pion masses:

$$m_\pi \simeq \begin{cases} 670 \text{ MeV} & am_q = 0.03 \\ 555 \text{ MeV} & am_q = 0.02 \\ 415 \text{ MeV} & am_q = 0.01 \\ 330 \text{ MeV} & am_q = 0.005, \end{cases} \tag{6.67}$$

and, for the $32^3$ extrapolation the un-physical unitary quark masses, correspond to:

$$m_\pi \simeq \begin{cases} 390 \text{ MeV} & am_q = 0.008 \\ 345 \text{ MeV} & am_q = 0.006 \\ 290 \text{ MeV} & am_q = 0.004, \end{cases} \tag{6.68}$$

see fig. 6.1. More detailed information on the specifics of the three ensembles can be found in [3, 85, 88].

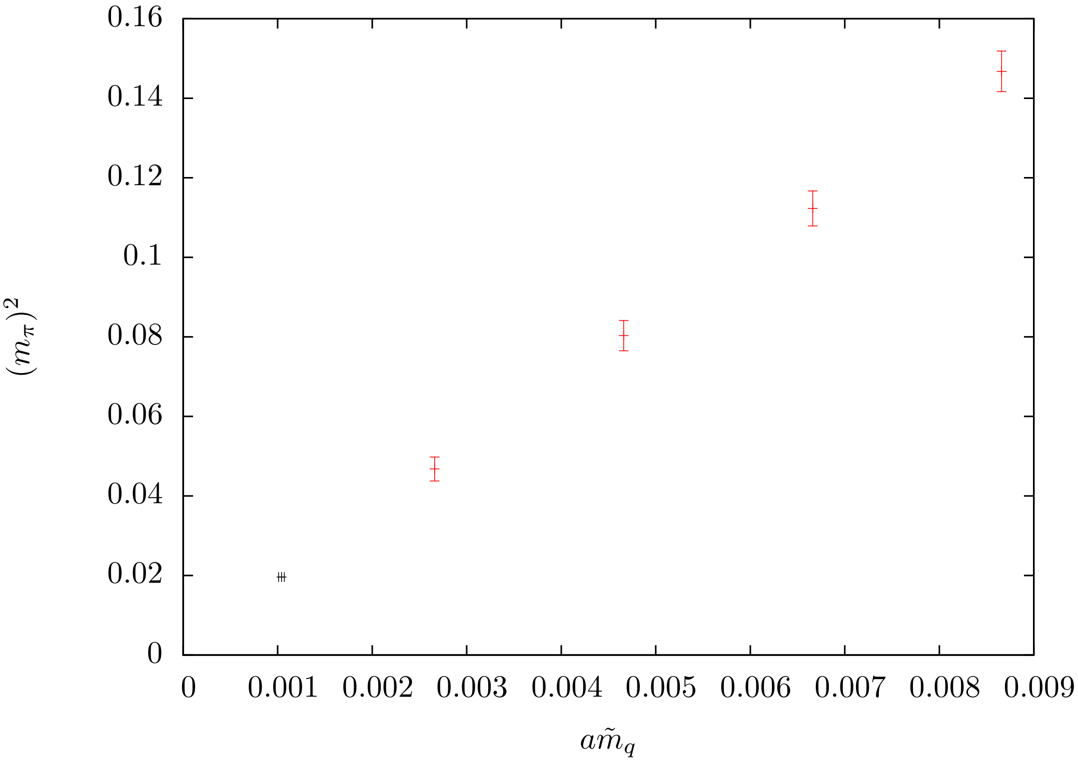

**Figure 6.1:** *Plot demonstrating the relationship between the lattice quark mass* $a\tilde{m_q} = am_q + am_{res}$ *and the squared pion mass* $(m_\pi)^2$ *for the* $32^3$ *ensemble. The pion mass is given in* $GeV$*. The red points correspond to the un-physical quark masses used in our simulations. The black point corresponds to the physical pion mass* $\sim 140MeV$ *(its* $a\tilde{m_q}$ *value is given in table 6.1). Note that the* $am_q = 0.002$ *point included in this plot is excluded from the calculations performed in this thesis.*

# Chapter 7

# Renormalisation

The work presented in this section closely follows that published in [1]. The additional results using the $32^3$ lattice and the use of partially twisted boundary conditions for the calculation of non-perturbative renormalisation constants will appear in a forthcoming publication.

Evaluating the moments of PDAs and structure functions requires the calculation of the matrix elements that appear in the operator product expansion. In order to determine finite answers in the continuum limit it is necessary to renormalise the operators that appear in these matrix elements. The renormalised matrix elements need to be multiplied by the perturbative short-distance Wilson coefficients. Together these are an observable quantity, which should be independent of the renormalisation scheme used. However, the coefficients and the renormalisation constants for the matrix elements are required to be in the same scheme, otherwise the scale dependence will not cancel. The Wilson coefficients may be calculated from perturbation theory in the continuum, usually in the $\overline{\mathrm{MS}}$ dimensional regularisation scheme and so we should convert our bare lattice operators to continuum $\overline{\mathrm{MS}}$ operators, in order for our results to be phenomenologically useful.

For small lattice spacing, $a$, and a sufficiently large renormalisation scale, $\mu$, it is possible to perform the renormalisation of the bare lattice operators using lattice perturbation theory. This, however, frequently suffers from large coefficients that lead to a slow convergence of the perturbative series. An alternative method that uses a nonperturbative prescription for the renormalisation through Monte Carlo simulations was introduced in [89].

In order to convert our bare lattice results to results in the $\overline{\text{MS}}$ scheme, we determine the renormalisation factors non-perturbatively in the modified Regularisation Independent Momentum (RI′/MOM) scheme, followed by a conversion to $\overline{\text{MS}}$ with three-loop continuum perturbation theory [90, 91]. There is a contribution to the second moment for the PDAs from mixing with a total derivative operator, which, due to the current non-perturbative scheme, we are required to calculate perturbatively.

## 7.1 Perturbative Renormalisation

The calculation of the perturbative renormalisation constants is described in [1]. They were used for the $24^3$ results in the thesis [92], and are also applied here for the $32^3$ results.

Lattice operators are chosen so that, at tree level, they have the same matrix elements as continuum operators. This does not persist at higher orders with loops. At one loop [93],

$$\langle q|O_i^{\text{lat}}|q\rangle = \sum_j \left(\delta_{ij} + \frac{g_0^2}{16\pi^2}\left(-\gamma_{ij}^{(0)}\log a^2p^2 + R_{ij}^{\text{lat}}\right)\right)\langle q|O_j^{\text{tree}}|q\rangle, \tag{7.1}$$

$$\langle q|O_i^{\overline{\text{MS}}}|q\rangle = \sum_j \left(\delta_{ij} + \frac{g_{\overline{\text{MS}}}^2}{16\pi^2}\left(-\gamma_{ij}^{(0)}\log \frac{p^2}{\mu^2} + R_{ij}^{\overline{\text{MS}}}\right)\right)\langle q|O_j^{\text{tree}}|q\rangle, \tag{7.2}$$

where $R_{ij}^{\text{lat}}$ and $R_{ij}^{\overline{\text{MS}}}$ are the lattice and continuum one loop renormalisation constants that are determined through applying the appropriate Feynman rules and evaluating the resulting diagrams. The lattice and $\overline{\text{MS}}$ renormalisation constants do not have to have the same value because the lattice propagators and vertices differ from the continuum when the loop momentum is $\mathcal{O}(1/a)$. In fact, whilst the evaluation of the relevant Feynman diagrams in the continuum is relatively straightforward, for the lattice, the expressions tend to be very complicated and require a numerical evaluation.

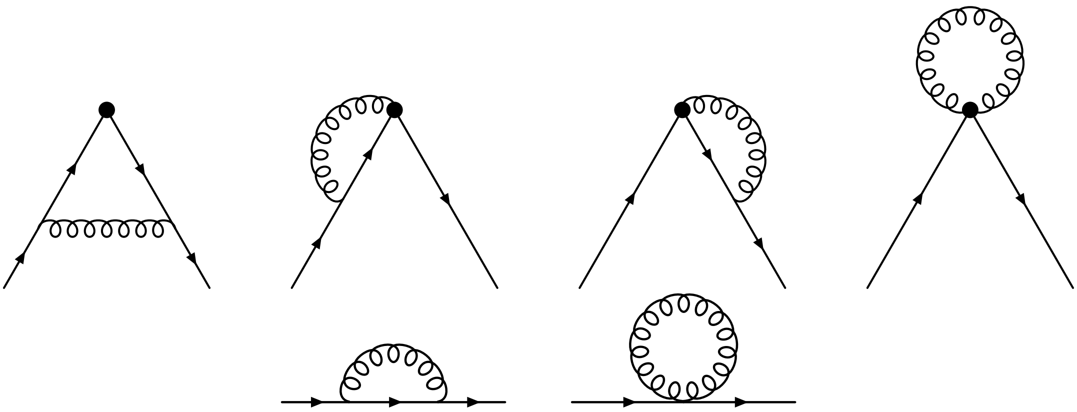

**Figure 7.1:** *Feynman diagrams required for the perturbative evaluation of the matching factors at one loop. The upper diagrams are for the vertex renormalisation and the lower diagrams are for the wavefunction renormalisation [1].*

We can connect the lattice values to the continuum physical results

$$\langle q|O_i^{\overline{\mathrm{MS}}}|q\rangle = \sum_j \left(\delta_{ij} - \frac{g_0^2}{16\pi^2}\left(-\gamma_{ij}^{(0)}\log a^2\mu^2 + R_{ij}^{\mathrm{lat}} - R_{ij}^{\overline{\mathrm{MS}}}\right)\right)\langle q|O_j^{\mathrm{lat}}|q\rangle, \qquad (7.3)$$

where the $\gamma_{ij}^{(0)}$ are anomalous dimensions and the differences $\Delta R_{ij} = R_{ij}^{\mathrm{lat}} - R_{ij}^{\overline{\mathrm{MS}}}$ enter in the matching factors

$$Z_{ij}(a\mu, g_0) = \delta_{ij} - \frac{g_0^2}{16\pi^2}\left(-\gamma_{ij}^{(0)}\log a^2\mu^2 + \Delta R_{ij}\right). \qquad (7.4)$$

The superscript $\overline{\mathrm{MS}}$ refers to terms from the continuum calculation, whereas those without superscripts are from the lattice. Once the bare lattice values have been matched to the continuum at the lattice scale $\mu a = 1$, using eq. (7.4), the result may be run to the desired scale using continuum perturbation theory.

For the moments of the PDAs (and structure functions), we need to evaluate the Feynman diagrams contained in fig. 7.1 in order to calculate the matching factors discussed above. We define for the first- and second-moment PDA operators

$$\begin{aligned}
\mathcal{O}_{\{\rho\mu\}}^{\overline{\mathrm{MS}}}(\mu) &= Z_{\mathcal{O}_{\{\rho\mu\}}}(\mu a)\mathcal{O}_{\{\rho\mu\}}^{\mathrm{latt}}(a), && (7.5)\\
\mathcal{O}_{DD}^{\overline{\mathrm{MS}}}(\mu) &= Z_{DD,DD}(\mu a)\mathcal{O}_{DD}^{\mathrm{latt}}(a) + Z_{DD,\partial\partial}(\mu a)\mathcal{O}_{\partial\partial}^{\mathrm{latt}}(a), && (7.6)
\end{aligned}$$

where we note that for the second moment we must take account of the mixing with the total derivative. The operators have the form

$$\begin{aligned}
\mathcal{O}_{\{\rho\mu\}} &= \overline{\psi}\gamma_{\{\mu}\gamma_5 \overleftrightarrow{D}_{\rho\}}\psi, && (7.7)\\
\mathcal{O}_{DD} &= \overline{\psi}\gamma_{\{\mu}\gamma_5 \overleftrightarrow{D}_{\nu} \overleftrightarrow{D}_{\rho\}}\psi, && (7.8)\\
\mathcal{O}_{\partial\partial} &= \partial_{\{\nu}\partial_{\rho}\overline{\psi}\gamma_{\mu\}}\gamma_5\psi. && (7.9)
\end{aligned}$$

It should be noted that, owing to the chiral symmetry of the domain wall fermion action, the results obtained from these operators will also apply to operators without the $\gamma_5$. The renormalisation factors for the operators are given by

$$\begin{aligned}
Z_{\mathcal{O}_{\{\rho\mu\}}}(\mu a) &= \frac{1}{(1-w_0^2)Z_w}\left[1+\frac{\alpha C_F}{4\pi}\left(-\frac{16}{3}\ln(\mu a)+c\right)\right], && (7.10)\\
Z_{DD,DD}(\mu a) &= \frac{1}{(1-w_0^2)Z_w}\left[1+\frac{\alpha C_F}{4\pi}\left(-\frac{25}{3}\ln(\mu a)+c_{DD}\right)\right], && (7.11)\\
Z_{DD,\partial\partial}(\mu a) &= \frac{1}{(1-w_0^2)Z_w}\frac{\alpha C_F}{4\pi}\left(\frac{5}{3}\ln(\mu a)+c_{\partial\partial}\right), && (7.12)
\end{aligned}$$

which have the form of eq. (7.4) and where

$$\begin{aligned}
c &= \Sigma_1^{\overline{\rm MS}} - \Sigma_1 + V^{\overline{\rm MS}} - V, && (7.13)\\
c_{DD} &= \Sigma_1^{\overline{\rm MS}} - \Sigma_1 + V_{DD}^{\overline{\rm MS}} - V_{DD}, && (7.14)\\
c_{\partial\partial} &= \Sigma_1^{\overline{\rm MS}} - \Sigma_1 + V^{\overline{\rm MS}} - V. && (7.15)
\end{aligned}$$

In each of the eqs.(7.10)-(7.12) we see the normalisation factor $(1-w_0^2)Z_w$. This contains $Z_w$, a correction to the normalisation factor $(1-w_0^2)$ of the physical quark fields in the domain-wall fermion formulation. It stems from an additive renormalisation of the domain-wall height $M = 1 - w_0$.

$$Z_w = 1 + \frac{\alpha C_F}{4\pi} z_w, \qquad z_w = \frac{2w_0}{1-w_0^2}\Sigma_w. \qquad (7.16)$$

The $\Sigma_1$ terms are extracted from the wavefunction renormalisation (lower) diagrams in fig. 7.1, whereas the $V$ vertex terms come from the upper amputated two point functions. For the continuum $\overline{\rm MS}$ scheme factors, it is necessary to evaluate the first three upper Feynman graphs, while for lattice perturbation theory there is an additional operator tadpole diagram to worry about (fourth upper Feynman diagram in fig. 7.1). The covariant derivative terms, subscript $DD$, may be extracted by considering equal incoming and outgoing momenta, whereas the total derivative contributions $\partial\partial$ may be extracted by setting incoming and outgoing momenta to be equal and opposite. The $\overline{\mathrm{MS}}$ factors in Naïve dimensional regularisation (NDR) in Feynman gauge with a gluon mass IR regulator are

$$\Sigma_1^{\overline{\mathrm{MS}}} = \frac{1}{2}, \qquad V^{\overline{\mathrm{MS}}} = -\frac{25}{18}, \tag{7.17}$$

$$V_{DD}^{\overline{\mathrm{MS}}} = -\frac{121}{72}, \qquad V_{\partial\partial}^{\overline{\mathrm{MS}}} = \frac{41}{72}. \tag{7.18}$$

The lattice factors are also evaluated in Feynman gauge with a gluon IR regulator and with the appropriate simulation parameters, i.e. using domain wall fermions and an Iwasaki gauge action. The results of this can be found tabulated in Table VI in [1], where the various factors are given for a range of the domain wall height M. For our simulations we use $M = 1.8$ which (along with other choices of M) corresponds to a rather large value for the one-loop coefficient [94, 95] $z_w \approx 112$ (Table VII in [1]). This indicates the need for mean-field improvement, which is now briefly discussed.

Lattice perturbation theory calculations require the evaluation of additional terms that do not occur in the continuum. The exponentiated form of the gauge links

$$U_\mu(x) = e^{iagA_\mu(x)} = 1 + iagA_\mu(x) - \frac{a^2g^2}{2}A_\mu^2(x) + ..., \tag{7.19}$$

lead to quark-gluon vertices with arbitrarily many gluons. All but the lowest are artefacts of the lattice, for which the contraction of the two gluons in the third term of eq. (7.19) leads to tadpole diagrams (fourth upper Feynman diagram in fig. 7.1). Owing to UV divergences in the tadpole loops, they are not suppressed by powers of $a^2$ and instead only by powers of $g^2$. It is because of the tadpole artefacts that we observe large perturbation theory coefficients [58]. The mean-field (tadpole) improvement procedures [95] work by separating the UV and IR parts of the lattice fields and integrating out the UV

$$e^{iagA_\mu(x)} = e^{iag(A_\mu^{IR}+A_\mu^{UV})} = ue^{iagA_\mu^{IR}(x)} = u\tilde{U}_\mu(x). \tag{7.20}$$

After this there are a new set of expansion parameters $\tilde{g}^2 = g^2/u^4$, $\tilde{\kappa} = \kappa u$, $\tilde{U} = U/u$ and $\tilde{\psi} = \psi/\sqrt{2\kappa u}$, for which the theory looks the same as before, except for the scaling of the gauge link [58].

We follow the mean field improvement prescription in section VI of [95]. The first step is to determine the mean field value for the domain wall height from the tadpole factor,

$$M^{MF} = M - 4(1 - P^{1/4}), \tag{7.21}$$

where $P$ is the average plaquette value in the chiral limit of our simulations. In the mean-field prescription, the physical quark normalisation factor becomes $[1-(w_0^{MF})^2]Z_w^{MF}$, where

$$\begin{aligned} Z_w^{MF} &= 1 + \frac{\alpha C_F}{4\pi} z_w^{MF}, && (7.22)\\ z_w^{MF} &= \frac{2w_0^{MF}}{1-(w_0^{MF})^2}(\Sigma_w + 32\pi^2 T_{MF}), && (7.23) \end{aligned}$$

where $T_{MF} = 0.0525664$ for the Iwasaki gauge action [95] and is the mean field tadpole factor. The factors $\Sigma_w$, $\Sigma_1$, $V$, $V_{DD}$ and $V_{\partial\partial}$ can then be evaluated at $M_{MF}$. The mean-field improvement also introduces factors of the mean link $u = P^{1/4}$ and its perturbative expansion

$$u_{pt} = 1 - \frac{\alpha C_F}{4\pi} 8\pi^2 T_{MF} \tag{7.24}$$

in the operators. For the operator with two covariant derivatives, it appears as $u_{pt}/u$, whereas for the two total derivatives, it appears as the inverse $u/u_{pt}$. It

|  | $P$ | $P^{1/4}$ | $M^{MF}$ | $Z_w^{MF}$ | $\Sigma^{MF}$ | $V^{MF}$ | $V_{DD}^{MF}$ | $V_{\partial\partial}^{MF}$ |
|---|---|---|---|---|---|---|---|---|
| $24^3$ | 0.58813(4) | 0.875726 | 1.3029 | 5.25088 | 3.9731 | -4.1907 | -10.045 | -0.1696 |
| $32^3$ | 0.615587(3) | 0.885773 | 1.3431 | 6.13245 | 3.9800 | -4.1772 | -10.023 | -0.1898 |

**Table 7.1:** *Values for various mean-field parameters for the* $24^3$ *and* $32^3$ *ensembles [1].*

follows that the matching factors are

$$\begin{aligned}
Z^{MF}_{\mathcal{O}_{\{\rho\mu\}}} &= \frac{1}{(1-(w_0^{MF})^2)Z_w^{MF}}\left[1+\frac{\alpha C_F}{4\pi}\left(-\frac{16}{3}\ln(\mu a)+c^{MF}\right)\right], \quad (7.25)\\
Z^{MF}_{DD,DD}(\mu a) &= \frac{1}{u}\frac{1}{(1-(w_0^{MF})^2)Z_w^{MF}}\\
&\quad \left[1+\frac{\alpha C_F}{4\pi}\left(-\frac{25}{3}\ln(\mu a)+c^{MF}_{DD}-8\pi^2 T_{MF}\right)\right], \quad (7.26)\\
Z_{DD,\partial\partial}(\mu a) &= u\frac{1}{(1-(w_0^{MF})^2)Z_w^{MF}}\frac{\alpha C_F}{4\pi}\left(\frac{5}{3}\ln(\mu a)+c_{\partial\partial}\right), \quad (7.27)
\end{aligned}$$

where the $c^{MF}$ factors have the same structure as their non-MF counterparts, and can be evaluated at the value of $M_{MF}$.

To evaluate the mean-field renormalisation constants, we use the mean-field improved coupling defined through the plaquette value [96]

$$\frac{1}{g^2_{MF}}(\mu) = \frac{P}{g_0^2}+d_g+c_p+\frac{22}{16\pi}{}^2\ln(\mu a)+N_f\left[d_f-\frac{4}{48\pi^2}\ln(\mu a)\right], \tag{7.28}$$

where $N_f = 3$ is the number of dynamical quark flavours. The values for $d_f$ are a function of the domain wall mass ( [1] table VII) and the other factors depend on the gauge action, which, for the Iwasaki gauge, are $c_p = -0.1401$ and $d_g = 0.1053$ [95]. In addition, we also determine the renormalisation constants using the continuum $\overline{\mathrm{MS}}$ coupling, calculated from the four-loop beta function [97]

$$\frac{\partial a_s}{\partial \ln \mu^2} = -\beta_0 a_s^2-\beta_1 a_s^3-\beta_2 a_s^4-\beta_3 a_s^5+\mathcal{O}(a_s^6) \tag{7.29}$$

where

$$\begin{aligned}
\beta_0 &= \frac{1}{4}\left(11 - \frac{2}{3}N_f\right), &(7.30)\\
\beta_1 &= \frac{1}{16}\left(102 - \frac{38}{3}N_f\right), &(7.31)\\
\beta_2 &= \frac{1}{64}\left(\frac{2857}{2} - \frac{5033}{18}N_f + \frac{325}{54}N_f^2\right), &(7.32)\\
\beta_3 &= \frac{1}{256}\left[\frac{149753}{6} + 3564\zeta_3 - \left(\frac{1078361}{162} - \frac{6508}{27}\zeta_3\right)N_f\right.\\
&\quad \left. + \left(\frac{50065}{162} + \frac{6472}{81}\zeta_3\right)N_f^2 + \frac{1093}{729}N_f^3\right], &(7.33)
\end{aligned}$$

and $a_s = \alpha/\pi$. In order to determine the coupling at any scale for the three flavour case we start from the world average value for $\mu = M_z$, $\alpha_s^{(5)}(M_z) = 0.1184 \pm 0.0007$ [98], where the superscript refers to it being for five flavours. We follow the procedure in [97] and run $\alpha_s$ across the $m_b$ and $m_c$ thresholds whilst respecting the following conditions

$$\alpha_s^{(5)}(m_b) = \alpha_s^{(4)}(m_b) \qquad \text{and} \qquad \alpha_s^{(4)}(m_c) = \alpha_s^{(3)}(m_c). \tag{7.34}$$

It is now possible to calculate the coupling constant for any scale with three dynamical flavours.

We use the mean field and continuum $\overline{\text{MS}}$ coupling to evaluate the matching factor eqs. (7.25)-(7.27). Our PDA and structure function calculations are, however, ratios of correlation functions and we, therefore, also evaluate the mean field improved expression for the axial vector current renormalisation, $Z_A$, [95] so that we may take ratios of the renormalisation factors, which has the added advantage that the factors of $1/(1-(w_0^{MF})^2)Z_w^{MF}$ cancel. The difference between the results for the two values of the coupling provide a systematic error. The results are calculated separately for both the $24^3$ and $32^3$ ensembles and are displayed in $\overline{\text{MS}}$ at $\mu a = 1$ in table 7.2 for both the $24^3$ and $32^3$ ensembles. Our final results are given in $\overline{\text{MS}}$ at $\mu = 2\text{GeV}$ in table 7.3.

The results in this section are suggestive of the need for a nonperturbative approach; whilst the mean field improved value $z_w^{MF} \approx 5$ is a vast improvement on

| | $Z^{MF}_{\mathcal{O}_{\{\rho\mu\}}}$ | $Z^{MF}_{DD,DD}$ | $Z^{MF}_{DD,\partial\partial}$ | $Z^{MF}_{A}$ | $\frac{Z^{MF}_{\mathcal{O}_{\{\rho\mu\}}}}{Z^{MF}_{A}}$ | $\frac{Z^{MF}_{DD,DD}}{Z^{MF}_{A}}$ | $\frac{Z^{MF}_{DD,\partial\partial}}{Z^{MF}_{A}}$ |
|---|---|---|---|---|---|---|---|
| $\alpha^{MF}_{32}$ | 1.0089 | 1.1679 | 0.0122 | 0.8294 | 1.2165 | 1.4082 | 0.0141 |
| $\alpha^{\overline{\mathrm{MS}}}_{32}$ | 0.9435 | 1.1093 | 0.0187 | 0.7377 | 1.2790 | 1.5037 | 0.0254 |
| $\alpha^{MF}_{24}$ | 0.9896 | 1.1604 | 0.0122 | 0.8009 | 1.2356 | 1.4488 | 0.0152 |
| $\alpha^{\overline{\mathrm{MS}}}_{24}$ | 0.9162 | 1.0966 | 0.0202 | 0.6934 | 1.3214 | 1.5815 | 0.0291 |

**Table 7.2:** $32^3$, *$\mu a = 1$ perturbative results for renormalisation factors for both the coupling determined using a mean field approach and through the continuum $\overline{MS}$ running for three flavours.*

| | $Z^{MF}_{\mathcal{O}_{\{\rho\mu\}}}$ | $Z^{MF}_{DD,DD}$ | $Z^{MF}_{DD,\partial\partial}$ | $Z^{MF}_{A}$ | $\frac{Z^{MF}_{\mathcal{O}_{\{\rho\mu\}}}}{Z^{MF}_{A}}$ | $\frac{Z^{MF}_{DD,DD}}{Z^{MF}_{A}}$ | $\frac{Z^{MF}_{DD,\partial\partial}}{Z^{MF}_{A}}$ |
|---|---|---|---|---|---|---|---|
| $\alpha^{MF}_{32}$ | 1.0184 | 1.1878 | 0.0090 | 0.8243 | 1.2355 | 1.4410 | 0.0109 |
| $\alpha^{\overline{\mathrm{MS}}}_{32}$ | 0.9535 | 1.1360 | 0.0141 | 0.7229 | 1.3190 | 1.5714 | 0.0194 |
| $\alpha^{MF}_{24}$ | 0.9791 | 1.1383 | 0.0156 | 0.8062 | 1.2144 | 1.4119 | 0.0194 |
| $\alpha^{\overline{\mathrm{MS}}}_{24}$ | 0.9054 | 1.0664 | 0.0251 | 0.7107 | 1.2739 | 1.5004 | 0.0353 |

**Table 7.3:** $24^3$ *and* $32^3$, *$\mu = 2GeV$ perturbative results for renormalisation factors for both the coupling determined using a mean field approach and through the continuum $\overline{MS}$ running for three flavours.*

| | $\frac{Z^{MF}_{\mathcal{O}_{\{\rho\mu\}}}}{Z^{MF}_{A}}$ | $\frac{Z^{MF}_{DD,DD}}{Z^{MF}_{A}}$ | $\frac{Z^{MF}_{DD,\partial\partial}}{Z^{MF}_{A}}$ |
|---|---|---|---|
| $32^3$ | 1.28(4) | 1.51(6) | 0.015(4) |
| $24^3$ | 1.24(3) | 1.46(4) | 0.027(8) |

**Table 7.4:** $24^3$ *and* $32^3$, *$\mu = 2GeV$ perturbative results for ratios of renormalisation factors in $\overline{MS}$.*

the un-improved value, it is still rather large to justify working only to one loop. We also observe from table 7.3 that the matching factors $Z$ deviate substantially from unity, suggesting that our one loop lattice perturbation theory results are not reliable. Furthermore, the two choices in the coupling, which differ at higher order than calculated here, lead to a large difference in the matching factors, again suggesting that a higher order perturbative calculation is needed. The natural progression is to therefore calculate these factors non-perturbatively. Our implementation of a non-perturbative scheme means we have to rely upon the perturbative results in table 7.4 for the renormalisation factor for the mixing of the total derivative term. However, work is currently in progress to calculate this term non-perturbatively, and will be discussed later in this chapter.

## 7.2 Non-Perturbative Renormalisation

The non-perturbative calculation of the renormalisation constants utilises the Rome-Southampton RI$'$/MOM scheme [89]. The renormalised operator $\mathcal{O}(\mu)$ which depends on a scale $\mu$, is defined by the introduction of a renormalisation constant,

$$\mathcal{O}(\mu) = Z_{\mathcal{O}}\left(\mu a, g(a)\right)\mathcal{O}(a), \tag{7.35}$$

where $Z_{\mathcal{O}}$ may be determined through the application of a simple renormalisation condition, eq. (7.36) below, that is independent of the regularisation scheme used and may be applied to both the continuum and the lattice. This provides the means for scheme changes, and is what will ultimately allow the matching to $\overline{\text{MS}}$.

$$\Lambda_{\mathcal{O}}(p) = Z_{\mathcal{O}}(\mu a) Z_q^{-1}(\mu a) \Lambda_{\mathcal{O}}^{\text{bare}}(pa)|_{p^2=\mu^2} = \Lambda_{\mathcal{O}}^{\text{tree}}(p), \tag{7.36}$$

where $Z_q$ is the quark wavefunction renormalisation defined by $\psi = Z_q^{1/2}\psi_{\text{bare}}$. The renormalised (bare) vertex amplitudes $\Lambda_{\mathcal{O}}$ ($\Lambda_{\mathcal{O}}^{\text{bare}}$) are constructed from the amputated forward Green's function $G_O(p)$ of a two fermion bare lattice operator $\mathcal{O}(a)$ computed between off shell quark states with momentum $p$, where $p^2 = \mu^2$, traced with a suitable projector $P_{\mathcal{O}}$

$$\Lambda_{\mathcal{O}}(p) = \mathrm{Tr}[\Pi_{\mathcal{O}}(p) P_{\mathcal{O}}], \tag{7.37}$$

where,

$$\Pi_{\mathcal{O}}(p) = \langle S(p) \rangle^{-1} \langle G_{\mathcal{O}}(p) \rangle \langle S(p) \rangle^{-1} \tag{7.38}$$

The projector $P_{\mathcal{O}}$ depends on the operator and is chosen to isolate the tree level contribution to the vertex amplitude. $S(p)$ is the quark propagator and the angle brackets define the average taken over gauge field configurations.

$$\begin{aligned} G_{\mathcal{O}} &= \langle \psi(p) \mathcal{O}(0) \overline{\psi}(p) \rangle, & (7.39) \\ \mathcal{O}(0) &= \sum_{x,x'} \overline{\psi}(x) J_{\mathcal{O}}(x,x') \psi(x'). & (7.40) \end{aligned}$$

We can use any conveniently calculable amplitude, since the renormalisation constant is a property of the operator and not of particular matrix elements of the operator. The somewhat unphysical construction of the vertex amplitude, containing external quark propagators that are not gauge invariant, requires gauge-fixing for which we choose Landau gauge. The current $J_{\mathcal{O}}$ contains the appropriate Dirac structure and, as for the calculation of the moments, may be non-local if the operator contains derivatives. For example a right covariant derivative in the vector case would correspond to

$$J_{\mathcal{O}_{\rho\mu}}(x,x') = \gamma_\rho \frac{1}{2} (U(x,x') \delta_{x',x+\hat{\mu}} - U(x,x') \delta_{x',x-\hat{\mu}}). \tag{7.41}$$

The renormalisation procedure defined above has been done for forward matrix elements with equal incoming and outgoing quark momenta $p = p'$ (often described as the exceptional case). For our calculation this has the disadvantage that the exceptional momenta lead to $q = p - p' = 0$ for which matrix elements of operators containing total derivatives vanish, making $Z_{DD,\partial\partial}$ inaccessible in our non-perturbative calculations. In general, the renormalisation conditions may be defined at different external quark momenta $p$ and $p'$ where taking $p \neq p'$ would allow the calculation of the mixing term $Z_{DD,\partial\partial}$. Until recently the required perturbative matching calculation had not been performed for this class of momentum choice. For the choice $p^2 = p'^2 = q^2$ the continuum calculation has been performed in [99, 100] and work is currently under way to calculate $Z_{DD,\partial\partial}$ (as well as $Z_{\mathcal{O}_{\rho\mu}}$ and $Z_{DD,DD}$) non-perturbatively.

The range of allowed momenta are constrained to a window. In order to obtain a physical quantity, a cancellation of the renormalisation scale between the matrix element of the renormalised operator $\mathcal{O}(\mu)$ and the appropriate Wilson coefficient is required. The Wilson coefficient is calculated in the continuum through an expansion in $\alpha_s$ at a scale of order $\mu$. This must be large enough ($\mu \gg \Lambda_{QCD}$) for perturbation theory to be applicable, and thus the NPR calculation must also respect this constraint for the matching to be possible. At the other end, it is desirable to find a scale $\mu$ that is low enough so that calculations do not suffer from the contamination of discretisation effects. Thus, only within the window

$$\Lambda_{QCD} \ll \mu \ll a^{-1}, \tag{7.42}$$

where $a$ is the lattice spacing used in the simulations, can the non-perturbative and lattice artefacts be small simultaneously [89].

Our NPR calculation uses momentum sources [101], which result in a volume average over the lattice and hence in smaller statistical errors than obtained through the use of point sources [97]. The Green's function in momentum space is,

$$G_{\mathcal{O}}(p) = \sum_{x,x'} \langle \gamma_5 S^{\dagger}(p)_x \gamma_5 J_{\mathcal{O}}(x,x') S(p)_{x'} \rangle \tag{7.43}$$

where, instead of using the quark propagator $S(x|y)$ that is obtained through an inversion of the Dirac matrix $M$ on a point source

$$\sum_x M(x',x) S(x|y) = \delta_{x',y}, \tag{7.44}$$

the momentum-space propagator $S(p)_x = \sum_y S(x|y) e^{ipy}$ is used, which is obtained through inverting with a momentum source [101]

$$\sum_x M(x', x) S(p)_x = e^{ipx'}. \tag{7.45}$$

This is defined on all lattice sites corresponding to the off-shell quarks used in the Green's function. For this approach, a separate inversion is required for each choice of momenta used in the simulation. This limitation is outweighed by the reduction in the number of configurations required by our calculations, due to the improvement in the statistical accuracy as a result of the the volume averaging. Therefore, as long as we are parsimonious in the momenta used, the statistical fluctuations are reduced with a lower overall computational cost.

### 7.2.1 Projectors

The PDA calculations require the renormalisation of operators with up to two derivatives $\mathcal{O}^{(5)}_{\{\mu_1 \cdots \mu_n\}}$ where $n = 1,\ 2$ or 3 for 0, 1 and 2 derivatives. The projectors required for the operators containing derivatives are more complicated than for the case of the bilinears. For the final conversion to $\overline{\text{MS}}$ as well as to account for the running (to $\mu =$ 2GeV), we use readily available continuum calculations [90, 91]. For this to be possible, our projectors must match the RI$'$/MOM scheme and vertex functions used in the continuum calculations. The amputated Green's function decomposes into the following terms allowed by Lorentz symmetry, where all indices are distinct [90, 91]:

$$G_{\mathcal{O}}(p) = \Sigma_1(p) \gamma_{\{\mu_1} p_{\mu_2} \cdots p_{\mu_n\}} + \Sigma_2(p) p_{\mu_1} \cdots p_{\mu_n} \not{p}. \tag{7.46}$$

Only the contribution from $\Sigma_1$ is used in the RI$'$/MOM scheme, and so our projectors, which depend upon both the momentum entering the Green's function as well as its fixed indices $(\mu_i)$, should be crafted in such a way as to isolate this term. For the case of vectors (axial-vector operators may be treated analogously, with the appropriate insertion of $\gamma_5$) the multiplication of $G_{\mathcal{O}}$ with $\gamma_{\mu_i}$ picks up contributions of both $\Sigma_1$ and $\Sigma_2$, whereas a projection with $\gamma_\rho$, where $\rho \neq \{\mu_i\}$ is sensitive to only $\Sigma_2$ (when $n \leq 3$). We should, therefore, be able to design a projector that isolates $\Sigma_1$ in eq. (7.46) from the difference of two Dirac matrices with appropriate normalisation and momentum factors. The projectors are simplified in the case where there are one or more components of zero momentum. For fixed indices $\mu_i$ ($i = 1, ..., n$) of the Green's function, we can construct $n$ different projectors $P_{\mathcal{O},i}$ by starting from any of the $\gamma_{\mu_i}$

$$P_{\mathcal{O},i} = \frac{\gamma_{\mu_i} - \gamma_\rho \frac{\overline{p}_{\mu_i}}{\overline{p}_\rho}}{\mathcal{N} \prod_{j \neq i, j=1}^{n} \overline{p}_{\mu_j}}, \qquad \text{with} \quad i = 1, ..., n. \tag{7.47}$$

The normalisation $\mathcal{N}$ is chosen so that $\Lambda_{\mathcal{O}}^{\text{tree}}(p) = 1$, and $\rho \notin \{\mu_i\}$ such that its momentum component $\overline{p}_\rho$ is as small as possible in order to reduce discretisation errors. The quantities $\overline{p}_\mu = \sin p_\mu$ are used to better account for the lattice momenta. The $n$ different projectors with all possible combinations of the Green's functions result in a total of 4, 12 and 12 ($n$ = 1, 2 and 3) choices to compute the vertex amplitude eq. (7.37). Each of the choices should, of course, provide the same result for the final renormalisation constant up to the lattice artefacts that occur due to the breaking of the continuum $O(4)$ symmetry. As a result of the different magnitudes of momentum components, the expected discretisation errors depend upon the directions selected by the projector.

### 7.2.2 Results for the Renormalisation Factors

To determine the renormalisation constant for the operator $Z_{\mathcal{O}}$ from the renormalisation condition eq. (7.36) requires the quark-field renormalisation $Z_q$ as an input. However, for our calculation, we are interested in ratios of the (one or two) derivative operators with operators containing no-derivatives - the vector and axial-vector bilinears. Due to the chiral symmetry of the domain-wall formalism, we could use either the vector or axial-vector bilinears and so we average $\Lambda_{\gamma_\rho}$ and $\Lambda_{\gamma_\rho}^5$ (as per [59]) for our final answer. Using the ratio results in an explicit cancellation of the quark-field renormalisation factors

$$\frac{Z_{\mathcal{O},n=2,\ 3}(\mu a)}{Z_{\mathcal{O},n=1}(\mu a)} = \left. \frac{\Lambda^{\text{bare}}_{\mathcal{O},n=1}(\mu a)}{\Lambda^{\text{bare}}_{\mathcal{O},n=2,3}(\mu a)} \right|_{p^2=\mu^2} . \tag{7.48}$$

The results should be independent of index choice and size of momentum components used for the projector. However, the reduced statistical errors due to the momentum source approach reveal the effects of lattice artefacts [102]. This can be observed by considering the different projectors for a given momenta $p_\mu$ of the external quarks, see fig 7.2. For our best answer we combine all choices and we account for the observed spread in the data through a systematic error.

The renormalisation constants are extracted in the following way. For each momentum choice (table. 7.5) a linear extrapolation in the un-physical light quark masses $m_q$ is performed down to the chiral limit $m_q = -m_{res}$ fig. 7.3. It is at the chiral limit that we are able to remove the running of our data points and match to the continuum scheme. The existing continuum results [90, 91] allow us to take our RI$'$/MOM scheme results at the scale $\mu^2 = p^2$ to a common scale $\mu^2 = (2\text{ GeV})^2$ and convert to $\overline{\text{MS}}$. The values that are obtained can then be linearly interpolated to $p^2 = (2\text{ GeV})^2$ to obtain $Z_{\mathcal{O},n=2,3}/Z_{\mathcal{O},n=1}$ at a scale $\mu = 2$ GeV. Fig 7.4 show the renormalisation factors before and after the running is removed. Once the running has been removed and the data points are at a common scale, they should have equal values. We observe that the data points are very flat, indicating that both the scale conversion and the momentum window are valid.

The central value for $Z_{\mathcal{O},n=2,3}/Z_{\mathcal{O},n=1}$ is computed from the averaged value of all projectors and index contributions. The statistical error is estimated through a bootstrap analysis. This error is inflated with $\sqrt{\chi^2/\text{d.o.f.}}$ (the PDG scale factor [103]) from the interpolation. The systematic errors arise from a few different effects, which we will now explore.

The lattice artefact error is estimated by analysing the data for each of the individual projector index and momentum component choices, from which we choose the highest and lowest values. This is done for each of the momenta and

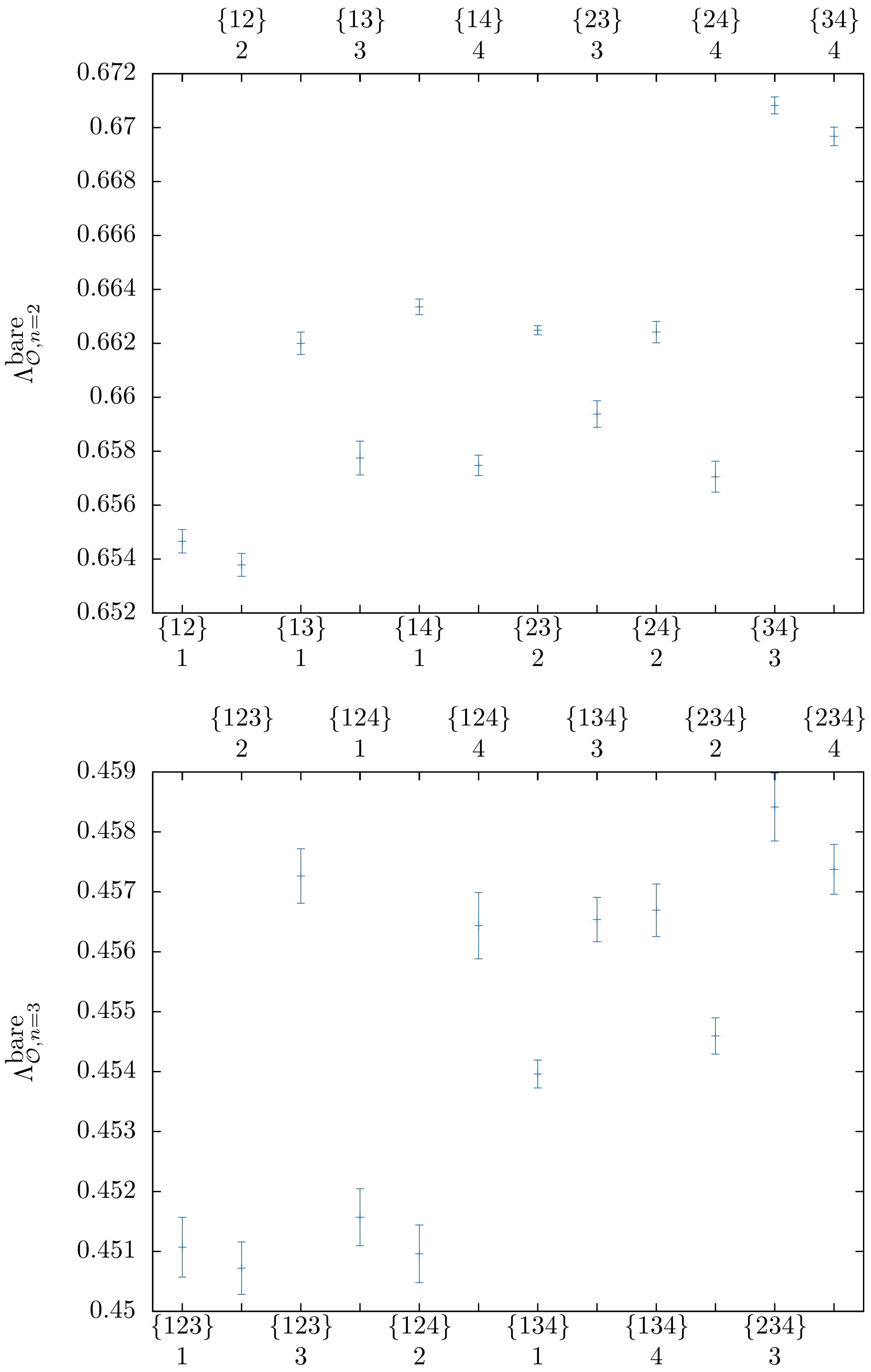

**Figure 7.2:** *Results for* $\Lambda^{bare}_{\mathcal{O},n=2}$ *and* $\Lambda^{bare}_{\mathcal{O},n=3}$ *are shown in the top and bottom panels respectively for a single momentum* $(ap)^2 = 1.78201$ *where* $p^T = (2, 2, 3, 8)$*. The labels above and below show the Green's function indices in the brackets with the projector's index below. The disagreement demonstrates the lattice artefacts [1].*

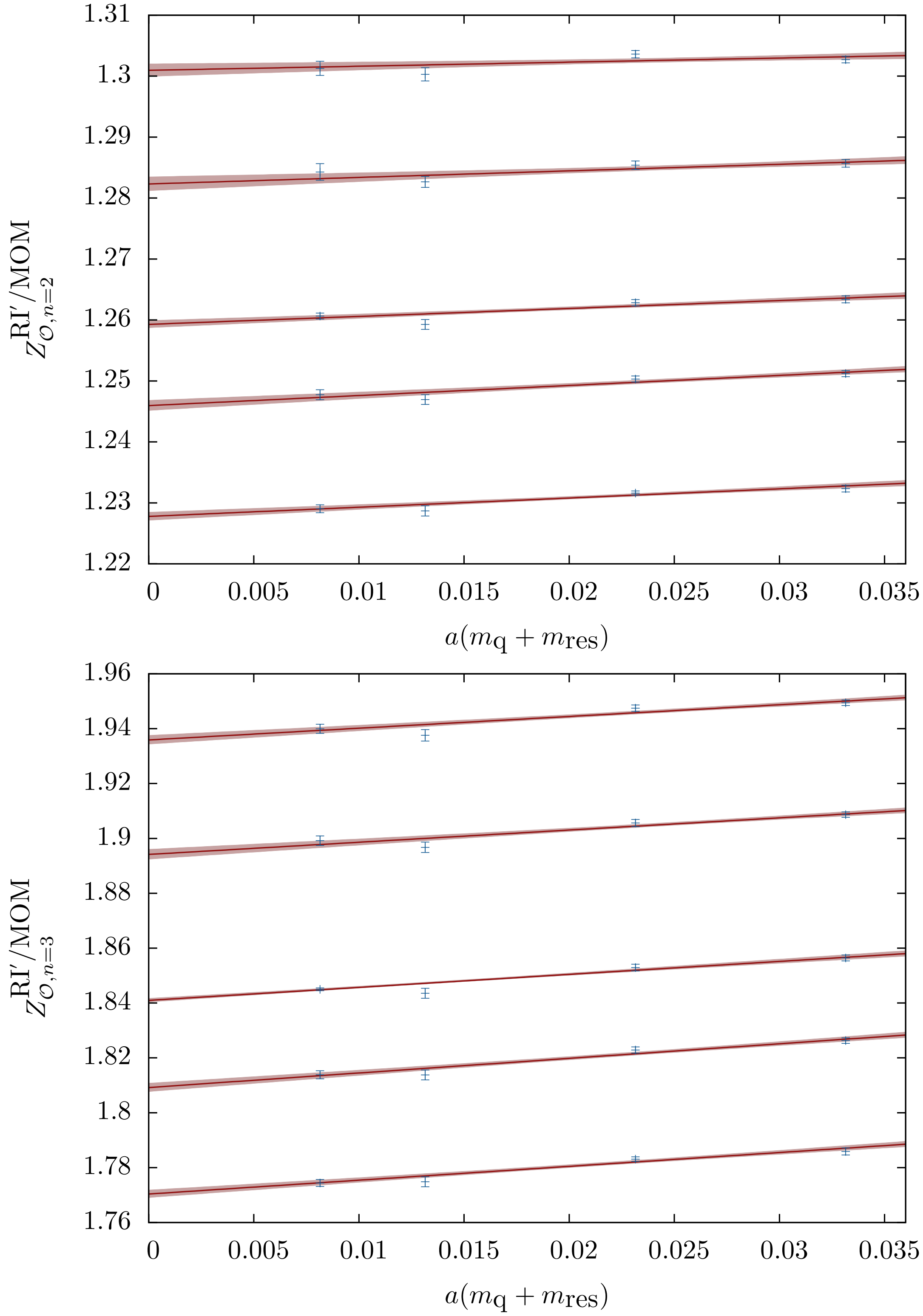

**Figure 7.3:** *Linear extrapolation of the renormalisation factors to the chiral limit for the* $n = 2$ *and* $n = 3$ *operators, top and bottom panels respectively. The momentum is increasing from top to bottom:* $(ap)^2 = 1.2947$, 1.4392, 1.6374, 1.7820, 1.9801 *[1].*

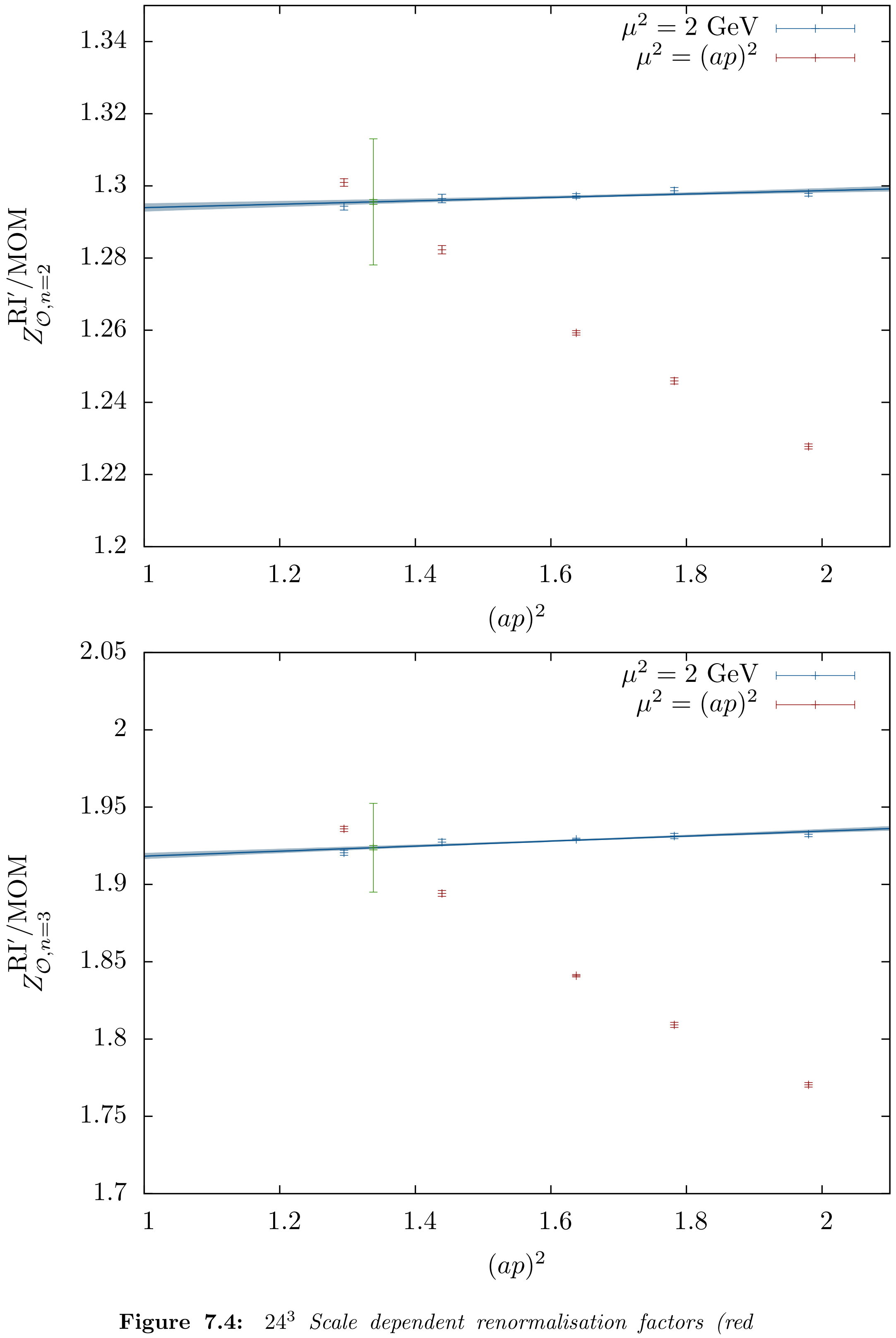

**Figure 7.4:** $24^3$ *Scale dependent renormalisation factors (red data-points) and fixed ($\mu = 2GeV$) scale renormalisation factors (blue data-points) with the running removed, both given in the RI′/MOM scheme. The linear interpolation to the final result with statistical error band is also shown, as are the systematic and statistical errors on the interpolated point (green data-point) [1].*

"highest" and "lowest" interpolations are performed separately. The larger difference between these and the central value is taken to be the systematic error for the discretisation effects and is refered to as the "spread" error.

The perturbative matching in the continuum is calculated to three-loops and we account for the missing higher order terms through the slope of the interpolation, using the difference of the results at $p^2 = (2\text{ GeV})^2$ and $(0\text{ GeV}^2)$, which we refer to as the "slope" error. Whilst some of this error will be down to the truncated perturbative expansion, there are also some entangled discretisation effects and so there is, to some extent, double counting of the discretisation effects.

A further effect, that we have already mentioned, is due to the good, but nonetheless approximate, chiral symmetry of the domain-wall formalism. This is evident from the difference in the final result when determined via $\frac{1}{2}(\Lambda_A + \Lambda_V)$ or from $\Lambda_A$ $(n = 1)$. The systematic error is estimated by this difference and is labelled as "V-A".

The final systematic error is due to the un-physical strange-quark mass used in the simulations, and our failure to extrapolate this to its physical value. This error, refered to as $\Delta m_s$, is estimated from the linear dependence (slope) in the chiral extrapolations multiplied by the strange-quark mass, as well as by a factor of $\frac{1}{2}$ to account for the fact that there is only one strange-quark mass compared to the two light-quark masses. The total systematic error is obtained by adding all four individual systematic effects in quadrature.

The final results for the renormalisation factors are obtained using the $n = 2$ and 3 operators with vector-like billinears, although the results from axial-vector operators are almost identical. The NPR calculation has been performed for all three ensembles, however the form of momenta is different for these (table. 7.5). For all of the ensembles, the momenta are chosen to be within the window eq. (7.42). For the $16^3$ and $24^3$ ensembles (with the same lattice spacing) the momenta were chosen from the experience gained from [97] which identified that, by limiting the magnitude of $\sum p_\mu^4$ for fixed $p^2$ [102], the hypercubic artefacts are reduced. This results in momentum choices that are close to the diagonal of the lattice. In

| | | | | | |
|---|---|---|---|---|---|
| $16^3 \times 32$ | $(1,1,2,3)$ | $(1,1,2,4)$ | $(1,2,2,1)$ | $(1,2,2,3)$ | $(1,2,2,4)$ |
| $24^3 \times 64$ | $(2,2,2,7)$ | $(2,2,2,8)$ | $(2,2,3,7)$ | $(2,2,3,8)$ | $(2,3,3,7)$ |
| $32^3 \times 64$ | $(3,2,2,2)$ | $(3,2,-1,-4)$ | $(4,0,-5,-6)$ | $(4,3,1,-8)$ | $(4,-5,0,-6)$ |
| | $(4,3,-1,-8)$ | $(4,-5,0,-6)$ | $(-4,-4,1,2)$ | $(4,0,-2,4)$ | $(4,2,2,0)$ |
| | $(4,4,3,2)$ | $(-4,-1,-4,2)$ | | | |

**Table 7.5:** *Momenta used for the three ensembles. Where we give* $n_\mu^T$ *for momenta* $p_\mu = 2\pi n_\nu / La$ *and* $L \to T$ *for time components.* $a^{-1} = 1.73(3)\,GeV$ *for the* $16^3$ *and* $24^3$ *lattices, and* $a^{-1} = 2.28(3)\,GeV$ *for the* $32^3$ *lattice.*

| | $Z_{\mathcal{O}_{\{\rho\nu\}}}/Z_A$ | | $Z_{DD,DD}/Z_A$ | |
|---|---|---|---|---|
| | $16^3 \times 32$ | $24^3 \times 64$ | $16^3 \times 32$ | $24^3 \times 64$ |
| central value | 1.54575 | 1.52893 | 2.06064 | 2.02800 |
| statistical error | 0.00249 | 0.00081 | 0.00482 | 0.00149 |
| spread | 0.02968 | 0.01809 | 0.03702 | 0.01534 |
| slope | 0.00470 | 0.00743 | 0.00097 | 0.02285 |
| $\Delta m_s$ | 0.00089 | 0.00232 | 0.00469 | 0.00992 |
| $V - A$ | 0.00723 | 0.00602 | 0.00938 | 0.00760 |
| total error | 0.03102 | 0.02061 | 0.03879 | 0.03026 |
| best result | | 1.5289(8)(206) | | 2.028(1)(30) |
| perturbative result | | 1.24(3) | | 1.45(5) |

**Table 7.6:** *Final results for the* $16^3$ *and* $24^3$ *renormalisation factors in* $\overline{MS}$ *at* $\mu = 2\,GeV$*. Results are given for both lattice sizes with all systematic errors. The perturbative results are also shown for comparison [1].*

contrast, the $32^3$ ensemble momentum choices are not close to the diagonal. They were initially designed for a non-exceptional scheme where $p \neq p'$ and $p^2 = p'^2 = q^2$, however, until very recently, the matching was only available for the exceptional case. These momenta were therefore used in our exceptional calculations. The results for the $16^3$ and $24^3$ ensembles are given in table 7.6 and the figures used for their determination (figs. 7.3 and 7.4) were used to illustrate the process above. The $32^3$ results are presented in table 7.8 as part of the twisted momentum discussion (section 7.2.3) for which the interpolation is performed in fig 7.5. For all cases, we note that the renormalisation factors clearly deviate from one and also from the perturbative results, table 7.4. Thus, for these quantities, non-perturbative renormalisation appears imperative.

| $\theta_{tw}$ | 0.00000 | 0.18750 | 0.37500 | 0.56250 | 0.75000 | 0.93750 | 1.12500 | 1.31250 |
|---|---|---|---|---|---|---|---|---|
| $(ap)^2_{24}$ | 1.23370 | 1.31201 | 1.39273 | 1.47586 | 1.56140 | 1.64935 | 1.73971 | 1.83248 |
| $p^2_{24}$ GeV$^2$ | 3.68807 | 3.92218 | 4.16349 | 4.41200 | 4.66772 | 4.93064 | 5.20076 | 5.47809 |
| $(ap)^2_{32}$ | 0.69396 | 0.73801 | 0.78341 | 0.83017 | 0.87829 | 0.92776 | 0.97859 | 1.03077 |
| $p^2_{32}$ GeV$^2$ | 3.60746 | 3.83645 | 4.07249 | 4.31557 | 4.56570 | 4.82287 | 5.08709 | 5.35835 |
| $\theta_{tw}$ | 1.50000 | 1.68750 | 1.87500 | 2.06250 | 2.25000 | -0.18750 | -0.37500 | |
| $(ap)^2_{24}$ | 1.92766 | 2.02524 | 2.12524 | 2.22765 | 2.33247 | 1.15780 | 1.08431 | |
| $p^2_{24}$ GeV$^2$ | 5.76262 | 6.05435 | 6.35329 | 6.65942 | 6.97277 | 3.46117 | 3.24147 | |
| $(ap)^2_{32}$ | 1.08431 | 1.13920 | 1.19545 | 1.25305 | 1.31201 | 0.65126 | 0.60992 | |
| $p^2_{32}$ GeV$^2$ | 5.63666 | 5.92202 | 6.21442 | 6.51387 | 6.82036 | 3.38552 | 3.17062 | |

**Table 7.7:** *Corresponding momentum for the twist angles $\theta_{tw}$ used in the twisted NPR calculation. Stated as both the lattice momenta $(ap)^2$ and the physical momenta $p^2$ for the $24^3$ and $32^3$ ensembles.*

### 7.2.3 Non Perturbative Renormalisation using Twisted Boundary Conditions

The use of twisted boundary conditions allows us to fix the direction of the momenta, whilst varying their size. This has the advantage that we constrain the calculation, for a given base momentum, to a single representation of the $H(4)$ group. The base momentum is defined as the momentum at zero twist. Applying a twist angle preserves the $H(4)$ symmetry of the momentum and thereby reduces the observed splitting for a given projector (or equivalently the averaged projectors) acting on a given set of indices for the Green's function. The base momentum choices for the twisted $24^3$ and $32^3$ calculations are $(0, 3, 3, 0)$ and $(-3, 0, 3, 0)$, once again chosen for a non-exceptional calculation. The twist angles are then applied to the non-zero elements in order to vary the momenta, these are given along with the correponding momenta for both data-sets in table 7.7. Twisting also allows us to tune our momenta within the NPR window, and is thus useful for the comparison of data-sets with two different lattice spacings. The same procedure is used for the twisted NPR calculation as discussed in the previous section, but with modified projectors due to the two components of zero-momenta. The results are displayed for the $32^3$ and $24^3$ data-sets in figs. 7.5 and 7.6 respectively and the numerical results are provided in tables 7.8 and 7.9. There is an obvious improvement in the resolution of the momenta, and with it we also see that the characteristic jumping as a result of the different representations has been removed and is reflected in the reduction of the spread error. The twisting technique does not remove the

| | $Z_{\mathcal{O}_{\{\rho\nu\}}}/Z_A$ | | $Z_{DD,DD}/Z_A$ | |
|---|---|---|---|---|
| | *Untwisted* | *Twisted* | *Untwisted* | *Twisted* |
| central value | 1.50403 | 1.49802 | 1.97286 | 1.97338 |
| statistical error | 0.00143 | 0.00049 | 0.01676 | 0.00044 |
| spread | 0.02044 | 0.00347 | 0.01953 | 0.00199 |
| slope | 0.00965 | 0.00465 | 0.04558 | 0.04069 |
| $\Delta m_s$ | 0.00091 | 0.00281 | 0.00453 | 0.01423 |
| $V - A$ | 0.00474 | 0.00352 | 0.01443 | 0.00732 |
| total error | 0.02316 | 0.00736 | 0.05448 | 0.04377 |

**Table 7.8:** *Final results for the renormalisation factors in* $\overline{MS}$ *at* $\mu = 2GeV$. *Results are given for the* $32^3$ *lattice for both twisted and untwisted momentum choices with all systematic errors.*

| | $Z_{\mathcal{O}_{\{\rho\nu\}}}/Z_A$ | | $Z_{DD,DD}/Z_A$ | |
|---|---|---|---|---|
| | *Untwisted* | *Twisted* | *Untwisted* | *Twisted* |
| central value | 1.52893 | 1.52409 | 2.02800 | 2.04366 |
| statistical error | 0.00081 | 0.00018 | 0.00149 | 0.00035 |
| spread | 0.01809 | 0.00058 | 0.01534 | 0.00117 |
| slope | 0.00743 | 0.00866 | 0.02285 | 0.02884 |
| $\Delta m_s$ | 0.00232 | 0.00324 | 0.00992 | 0.01036 |
| $V - A$ | 0.00602 | 0.00316 | 0.00760 | 0.00475 |
| total error | 0.02061 | 0.00980 | 0.03026 | 0.03103 |

**Table 7.9:** *Final results for the renormalisation factors in* $\overline{MS}$ *at* $\mu = 2GeV$. *Results are given for the* $24^3$ *lattice size for both twisted and untwisted momentum choices with all systematic errors.*

discretisation effects caused by the different representations, if we had of used a different base momentum we would have seen a different curve. In the future we could perform the NPR with two base momenta, in different hypercubic representations, to allow an estimate of the spread systematic error through their difference. We note that the twisted and untwisted data-sets need not be the same due to discretisation effects, this is clear from figs. 7.5 and 7.6.

The twisted data results from this section will be used for the renormalisation of PDAs in section 9. The momenta for both the $24^3$ and $32^3$ data-sets were chosen so that they occupy the same physical range, fig. 7.7 and due to the same “base” momenta we ensure that they occupy the same representation of the hypercubic group. This ensures that the renormalisation factors are consistent when studying any continuum (discretisation) effects.

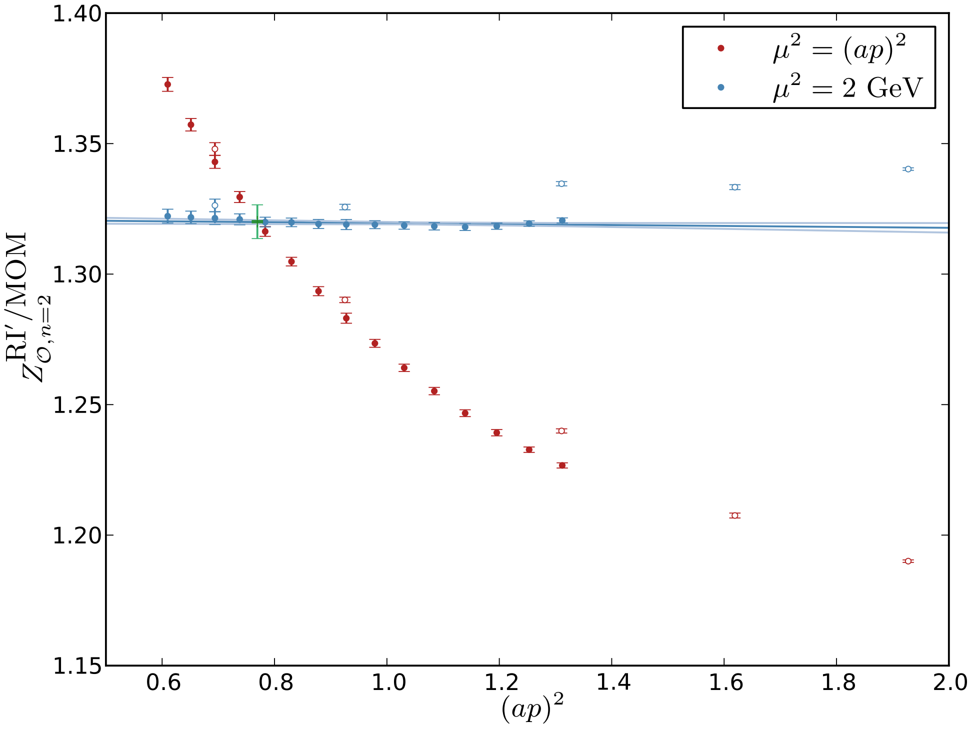

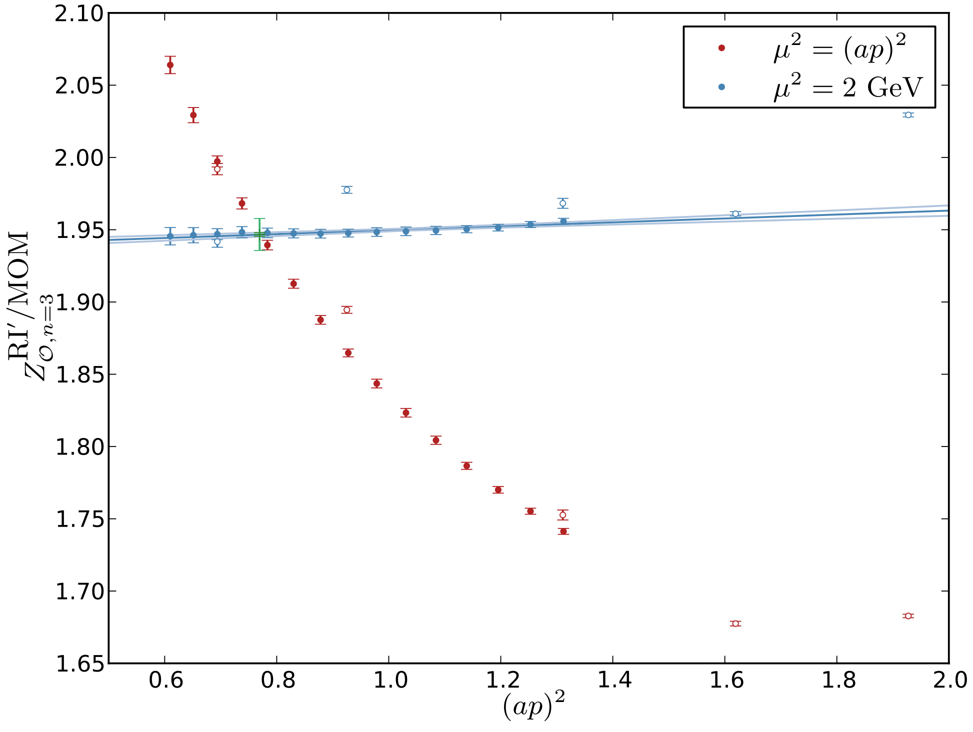

**Figure 7.5:** $32^3$ *Scale dependent renormalisation factors (red data-points) and fixed ($\mu = 2GeV$) scale renormalisation factors (blue data-points) with the running removed, both given in the RI′/MOM scheme. The linear interpolation to the final result with statistical error band is also shown, as are the systematic and statistical errors on the interpolated point (green data-point). The solid points use the twisted data-set and the hollow points are from the untwisted analysis.*

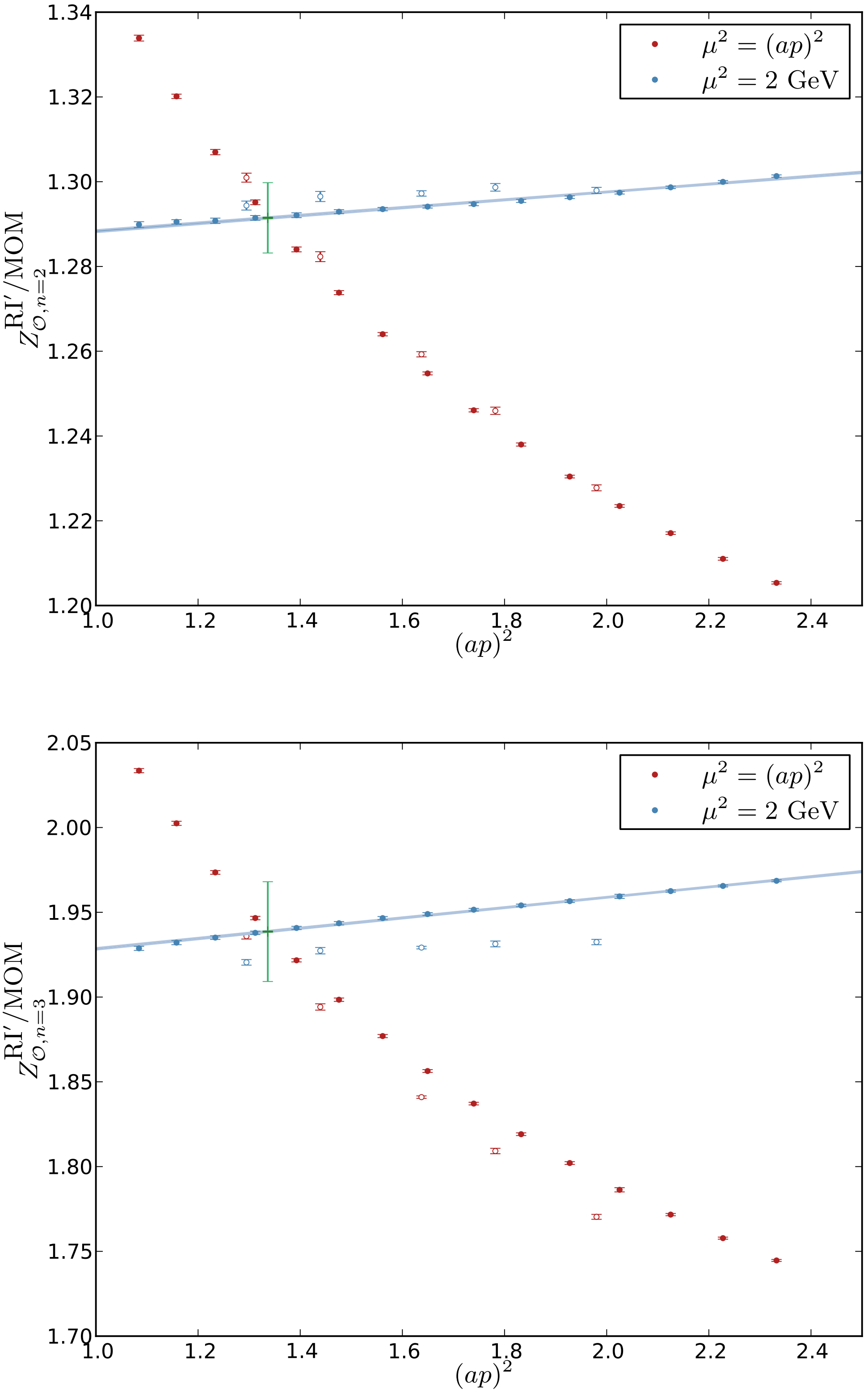

**Figure 7.6:** $24^3$ *Scale dependent renormalisation factors (red data-points) and fixed ($\mu = 2GeV$) scale renormalisation factors (blue data-points) with the running removed, both given in the RI′/MOM scheme. The linear interpolation to the final result with statistical error band is also shown, as are the systematic and statistical errors on the interpolated point (green data-point). The solid points use the twisted data-set and the hollow points are from the untwisted analysis.*

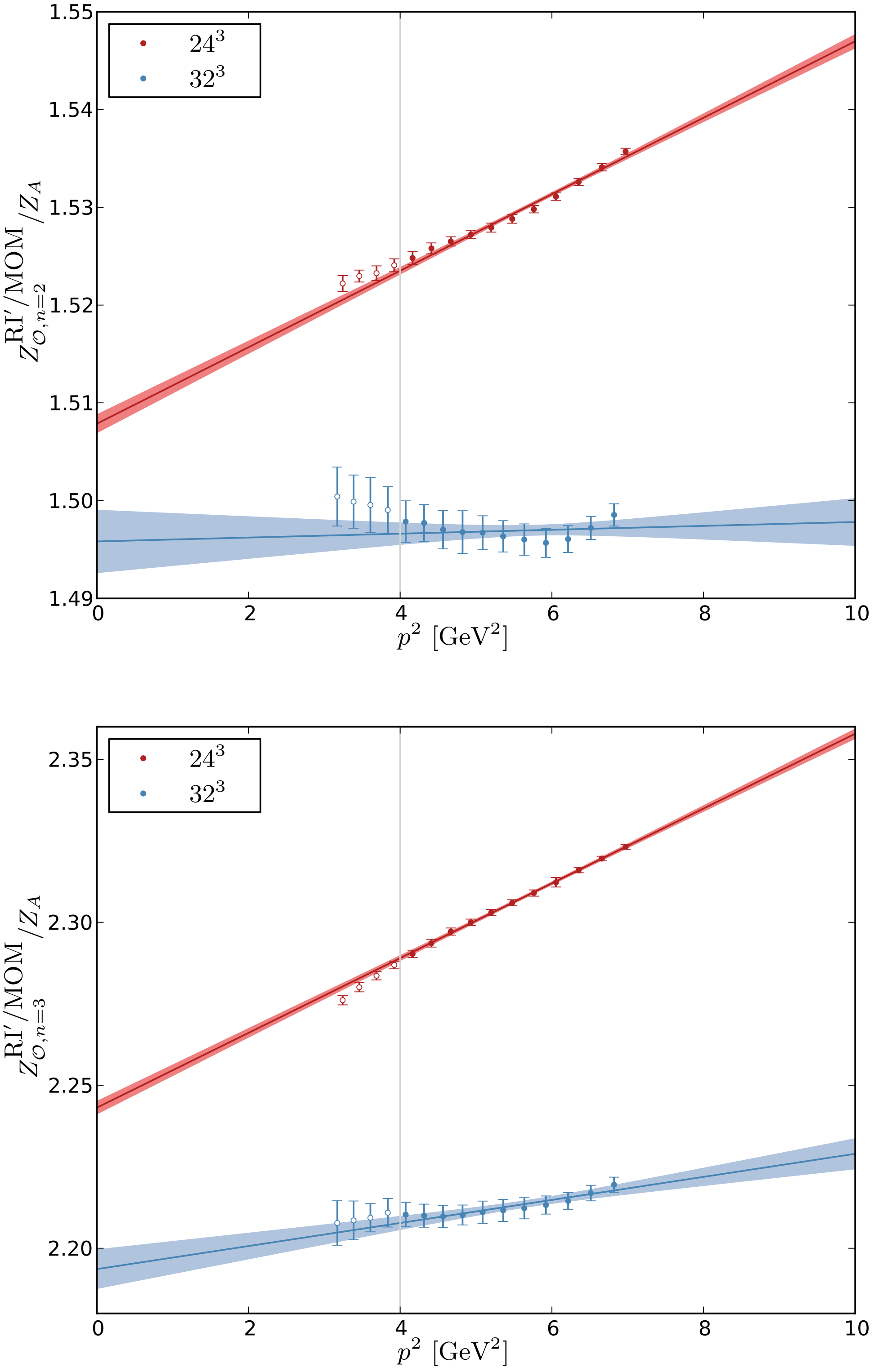

**Figure 7.7:** *Fixed ($\mu = 2GeV$) scale renormalisation factors with the running removed given in the RI′/MOM scheme. Demonstrating the physical range in $p^2$ for the $24^3$ (blue points) and $32^3$ (red points) ensembles. The solid data-points are included in the fit, whereas the hollow data-points are not. These are excluded due to the large coupling at scales below $\mu^2 = 2GeV^2$.*

|  | $Z_{\mathcal{O}_{v2,b}}/Z_A$ |  |
|---|---|---|
|  | $24^3$ | $32^3$ |
| central value | 1.46810 | 1.48364 |
| statistical error | 0.00586 | 0.01555 |
| spread | 0.00175 | 0.01750 |
| slope | 0.03866 | 0.00826 |
| $\Delta m_s$ | 0.00294 | 0.00362 |
| $V-A$ | 0.00439 | 0.00233 |
| total error | 0.03950 | 0.02519 |

**Table 7.10:** *Final results for the $\mathcal{O}_{v2,b}$ renormalisation factors in $\overline{MS}$ at $\mu = 2GeV$.*

### 7.2.4 Renormalisation for Structure Functions

The structure function calculation involves the use of the operator

$$\mathcal{O}_{v2,b} = \mathcal{O}_{44} - \frac{1}{3}(\mathcal{O}_{11} + \mathcal{O}_{22} + \mathcal{O}_{33}), \tag{7.49}$$

where the operator involves the derivative operators described by eq. (7.7) and the Green's functions decompose as in eq. (7.46). However, we now have a linear combination, which requires a different projector than described earlier. The projector

$$P_{\mathcal{O}_{v2,b}} = \frac{3}{4}\left(\frac{\gamma_4}{p_4} - \frac{1}{3}\left(\frac{\gamma_1}{p_1} + \frac{\gamma_2}{p_2} + \frac{\gamma_3}{p_3}\right)\right), \tag{7.50}$$

isolates the $\Sigma_1(p)$ term required for the NPR. The results from this are given for the $24^3$ and $32^3$ ensembles, using untwisted momenta, in fig. 7.8 and table. 7.10.

We observe an increase in the characteristic jumping that reflects the discretisation effects due to using momenta from different representations of the hypercubic group, as well as a decrease in the spread error for the renormalisation of the $\mathcal{O}_{v2,b}$ operator compared to the $\mathcal{O}_{v2,a}$ operator. The decrease in the spread error is due to the procedure, since for this operator we only have a single choice for the indices in the $\mathcal{O}_{v2,b}$ operator (the numerator of the ratio), and so the spread error comes purely from the four possible bilinears in the denominator. We also note that the statistical errors are larger with respect to the total error than before. This is likely to be caused, once again, by the specific $\mathcal{O}_{v2,b}$ operator, which removes the possibility of averaging over equivalent directions. An improvement would come

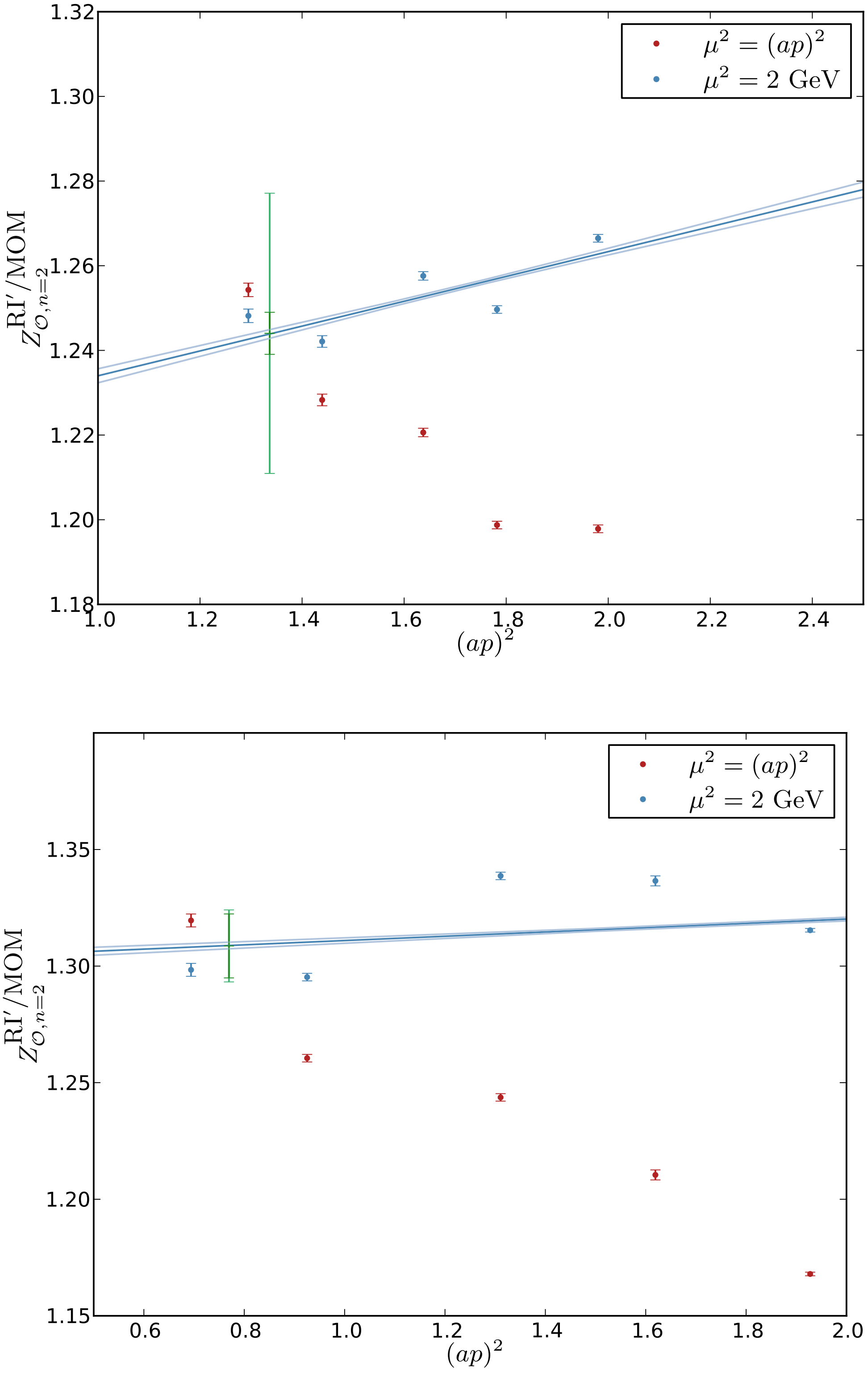

**Figure 7.8:** *$\mathcal{O}_{v2,b}$ operator, $32^3$. Scale dependent renormalisation factors (red data-points) and fixed ($\mu = 2GeV$) scale renormalisation factors (blue data-points) with the running removed, both given in the RI′/MOM scheme. The linear interpolation to the final result with statistical error band is also shown, as are the systematic and statistical errors on the interpolated point (green data-point).*

from using partially twisted boundary conditions, however the existing simulations for this all have a zero component of momentum in the 4-direction, and thus our projector (eq. (7.50)) would not work. For consistancy we use the untwisted results for the renormalisation of both the $\mathcal{O}_{v2,a}$ and $\mathcal{O}_{v2,b}$ operators in the structure function analysis. An interesting extension would therefore be to simulate with partially twisted boundary conditions that have a non-zero component in the 4-direction, to check the scale dependence of the non-perturbative renormalisation constants. This could also provide a more rigorous treatment of the discretisation error.

# Chapter 8

# Pion Structure Functions - Results

## 8.1 Lattice Data

The data available for the calculation of the pion structure functions, is the same as that which was used for $K_{l3}$ calculations in [2] and therefore uses (whilst not necessary for this calculation) partially twisted boundary conditions. This calculation is performed on our $32^3 \times 64$ cubed ensembles with three light-quark masses, $am_q$, as listed in Table 8.1. The twist angles $\theta_x$, $\theta_y$ and $\theta_z$ in table 8.1 show that, for this calculation, we twisted only in a single spatial direction and that we chose to have significantly more measurements, $N_{meas}$, for the lightest light-quark mass in order to offset the usual degradation of the statistical signal that is associated with the lighter quark masses. "Range" refers to the span of configurations that were used and $\Delta$ gives the number of molecular dynamics time steps that separate each consecutive measurement, so that Range/$\Delta = N_{meas}$. This

| $am_q$ | Range | $N_{meas}$ | $\Delta$ | $\theta_x$ | $\theta_y$ | $\theta_z$ |
|---|---|---|---|---|---|---|
| 0.008 | 500-1780 | 65 | 20 | 0.595907938605599 | 0 | 0 |
| 0.006 | 580-2080 | 76 | 20 | 0.68471639616995217 | 0 | 0 |
| 0.004 | 760-3420 | 267 | 20 | 0.78250119320561262 | 0 | 0 |

**Table 8.1:** *Parameters for the* $32^3 \times 64$ *dataset.*

calculation uses three-point functions, indicated in fig. 8.1. The pion is created and destroyed at times $t = 0$ and $t = T/2$ respectively, where $T$ is the temporal extent of the lattice. Spatially the pion states are created with a wall-source and destroyed with a wall-sink (all the initial and final spatial positions are summed over). The operator, $\mathcal{O}(x)$, is inserted at $(y, t)$ and its position is also summed over. The twist angles are applied either side of the current for the quarks $q_{i,f}$, whereas for the spectator quark, $q_s$, $\theta_s = 0$. For this calculation, we are interested in forward matrix elements and so we chose the twist angles to be equal, $\theta_i = \theta_f$. The first twist angle is for the propagator from source to current, while the second twist angle is for the propagator from current to sink.

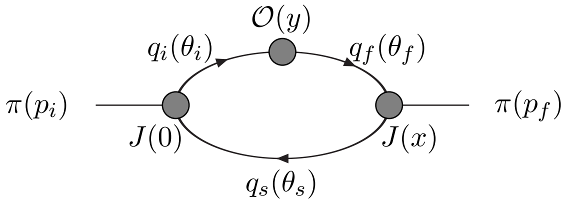

**Figure 8.1:** *Quark flow diagram for the structure function calculation [2].*

## 8.2 Calculation on the Lattice

The local vector current

$$V_\mu(x) = \overline{q}(x)\gamma_\mu q(x) \tag{8.1}$$

is a conserved current in the continuum, however this is not the case on the lattice. On the lattice, using the Iwasaki gauge action, there is an alternative conserved current, $V_\mu^{\text{cons}}$, with a modified structure to the familiar continuum current. This is, however, related multiplicatively to the local vector current $V_\mu$, so that

$$\langle\pi|V_\mu^{\text{cons}}|\pi\rangle = Z_V\langle\pi|V_\mu|\pi\rangle. \tag{8.2}$$

$Z_V$ can be determined perturbatively or determined directly through a comparison of the matrix elements in eq. (8.2). Using a related approach, it is possible to determine $Z_V$ through our structure function results, which will be demonstrated later. Had we have used the conserved lattice vector current, its corresponding renormalisation constant is unity [104].

For the calculation of the average momentum carried by the quarks of a given flavour in the pion $\langle x\rangle_f$, it is necessary to calculate the following matrix element

$$\langle \pi(p)|\mathcal{O}_2^{\{\mu\nu\}}(0)|\pi(p)\rangle = p^{\{\mu}p^{\nu\}}A_2(p), \tag{8.3}$$

where $|\pi(p)\rangle$ is a pion state with momentum p and

$$\mathcal{O}_2^{\{\mu\nu\}}(0) = i^2\overline{\psi}\gamma^{\{\mu}\overleftrightarrow{D}^{\nu\}}\psi - \text{traces} \tag{8.4}$$

There are two cases that we may choose: $\mu = \nu$ and $\mu \neq \nu$. For the case $\mu = \nu$, there are three linearly independent operators, which transform as a three-dimensional irreducible representation of the hypercubic group (section 6.7). The subtraction of the trace removes the singlet component. We do not observe the large statistical errors associated with the subtraction of a power divergence in our calculation. For the case $\mu \neq \nu$, there are six operators which transform in the six-dimensional irreducible representation of the hypercubic group, for which there is no mixing with lower-dimensional operators and hence the subtraction of the trace is avoided. A disadvantage here, however, is that at least one non-zero component of momentum is required for the matrix element to be non-zero, which unavoidably adds noise to the signal. The two choices, $\mu \neq \nu$ and $\mu = \nu$, are respectively (using the notation of [105]):

$$\begin{aligned} \mathcal{O}_{v2,a} &= \mathcal{O}_{\{41\}} && (8.5)\\ \mathcal{O}_{v2,b} &= \mathcal{O}_{44} - \frac{1}{3}\left(\mathcal{O}_{11} + \mathcal{O}_{22} + \mathcal{O}_{33}\right). && (8.6) \end{aligned}$$

For the computation of the required quantities on the lattice, we start with correlation functions. We are interested here in three-point correlation functions involving the operators $\mathcal{O}_{v2,a}$ and $\mathcal{O}_{v2,b}$, the vector current and a two-point correlation function. The three-point correlation function for the vector current is

$$C_V^{\mu}(t_x,t_y) = \sum_{\mathbf{x},\mathbf{y}} e^{i\mathbf{p}.\mathbf{x}} e^{i\mathbf{q}.\mathbf{y}} \langle 0|\mathrm{T}[P^{\dagger}(0)V^{\mu}(y,t_y)P(x,t_x)]|0\rangle, \tag{8.7}$$

which, for large times $t_y$ and $t_x - t_y$ reduces to

$$C_V^{\mu}(t_x,t_y) = \frac{1}{4EE'}\; e^{-E(t_x-t_y)}e^{-E't_y}\;\; |\langle\pi|P(0)|0\rangle|^2 \,(Z_V)^{-1} \left(p+p'\right)^{\mu} F(q^2). \tag{8.8}$$

where $q = p' - p$. For the structure function calculations, we are interested in the forward case $p = p'$ (due to the use of the optical theorem) for which this simplifies further:

$$C_V^{\mu}(t_x,t_y) = \frac{1}{4E^2}\; e^{-Et_x}\;\; |\langle\pi|P(0)|0\rangle|^2 \,(Z_V)^{-1}\, 2\, p^{\mu}, \tag{8.9}$$

where we have used the normalisation condition $F(0) = 1$. $Z_V$ is the renormalisation factor for the local vector current from eq. (8.2). The three-point function for the operator $\mathcal{O}_2^{\mu\nu}$, in the forward case reduces at large times to

$$C_{\mathcal{O}}^{\mu\nu}(t_x,t_y) = \frac{1}{4E^2}\; e^{-Et_x}\;\; |\langle\pi|P(0)|0\rangle|^2\, p^{\mu}p^{\nu} A_2(p), \tag{8.10}$$

where we have used eq. (8.3) to simplify the correlation function. We are now able to build a ratio to extract $\langle x\rangle = A_2/2$, where $E$ and $p^i$ are the energy and spatial momentum left over from the ratio

$$\frac{C_{\mathcal{O}}^{\mu\nu}(t_x,t_y)}{C_V^{\mu}(t_x,t_y)} = \begin{cases} p^i Z_V \langle x\rangle^{\mathrm{bare}}, & \mu = t \quad \nu = i \quad p^i \neq 0 \\ E Z_V \langle x\rangle^{\mathrm{bare}}, & \mu = i \quad \nu = t \quad p^i \neq 0 \\ E Z_V \langle x\rangle^{\mathrm{bare}}, & \mu = \nu \qquad\qquad\; p^i = 0 \end{cases} \tag{8.11}$$

An alternative method to extract the first moment, uses the two point function

$$\begin{aligned} C_{2pt}(t') \quad &= \quad \sum_{\mathbf{x}} e^{i\mathbf{p}.\mathbf{x}} \langle 0|\mathrm{T}[P^{\dagger}(0)P(x,t')]|0\rangle & (8.12) \\ &\xrightarrow{t'=T/2} \quad \frac{2e^{-ET/2}}{2E}\, |\langle\pi|P(0)|0\rangle|^2\,, & (8.13) \end{aligned}$$

which providing $t' = t_x = T/2$,

$$\frac{2C_{\mathcal{O}}^{\mu\nu}(t_x, t_y)}{C_{2pt}(T/2)} = \begin{cases} p^i \langle x \rangle^{\mathrm{bare}}, & \mu \neq \nu \quad p^i \neq 0 \\ E \langle x \rangle^{\mathrm{bare}}, & \mu = \nu \quad p^i = 0. \end{cases} \tag{8.14}$$

Here we do not need to worry about the renormalisation of the vector current. It follows that a comparison between the results from eq. (8.11) and eq. (8.14) should agree with existing results for $Z_V$.

## 8.3 Results

The fits to all ratios eq. (8.11) and eq. (8.14) are shown in figs. 8.2 and 8.3. We have five possibilities for these fits. First, we can use the operator with distinct indices $\mathcal{O}_{v2,a}$ that requires non-zero momenta (fig. 8.2) or the operator $\mathcal{O}_{v2,b}$ which can be used with zero momentum (fig. 8.3) and provides a cleaner signal with smaller error bars. We then have the choice of whether to use a two- or a three-point function in the denominator of the ratio. We see that the three-point function in the denominator provides a signal with less noise. Figs. 8.2 and 8.3 display the chosen fits-ranges for both cases, with errors determined using the bootstrap method. The fit-range was chosen to be stable with respect to small variations in the range, as well as to encompass as much of the plateau as possible. A range of $7 - 25$ proved to be successful for all cases. This range, with stable end points, helps to account for fluctuations within the fit-range, for example the 0.006 mass appears to rise and fall for the $\mathcal{O}_{v2,a}$ operator. We do note that for the $\mathcal{O}_{v2,b}$ operator there is a larger effect from variations of the range, however the results are consistent within errors. The results are given in table 8.2. In order to compare the results from the ratios with two-point correlation functions to the ratios with three-point correlation functions in the denominator, the bare results for the two-point denominator have been multiplied by $Z_V$ in table 8.2 ($\langle x \rangle'^{\mathrm{bare}}_{C_{\mathcal{O}41}/C_{2\mathrm{pt}}} = \langle x \rangle^{\mathrm{bare}}_{C_{\mathcal{O}41}/C_{2\mathrm{pt}}} Z_V$). This is also in anticipation of renormalising the bare moments with the ratio ($Z_{\mathcal{O}^{\mu\nu}}/Z_A$ and $Z_{\mathcal{O}_{v2,b}}/Z_A$), calculated non-perturbatively (and making use of $Z_V = Z_A$).

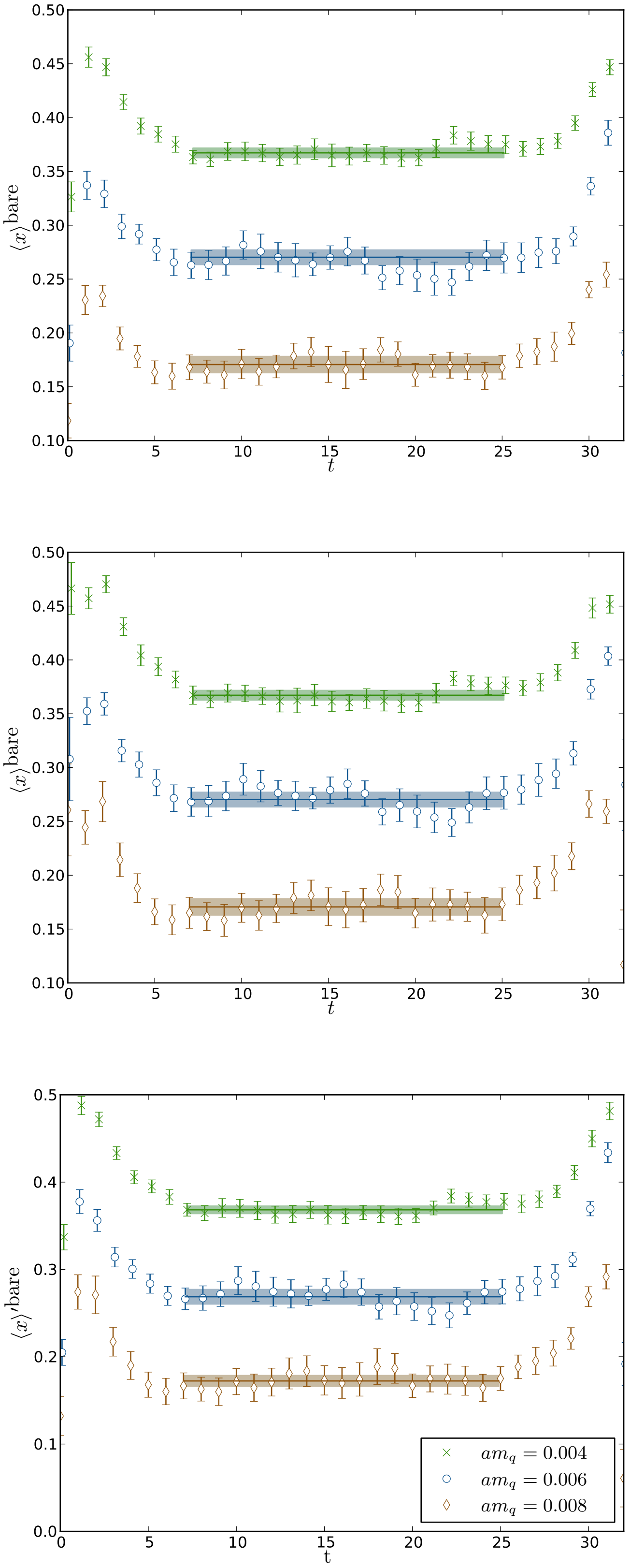

**Figure 8.2:** *Results for the* $\langle x \rangle^{bare}$ *using the* $\mathcal{O}_{v2,a}$ *operator. The top and middle panels use the three-point vector current in the denominator of the ratio (top panel* $V^1$*, middle panel* $V^4$*), whereas the bottom panel uses the two-point correlation function in the denominator. It should be noted that the* $am_q = 0.004$ *and* $0.006$ *datasets have been artificially shifted by* $0.1$ *and* $0.2$ *in the y-axis.*

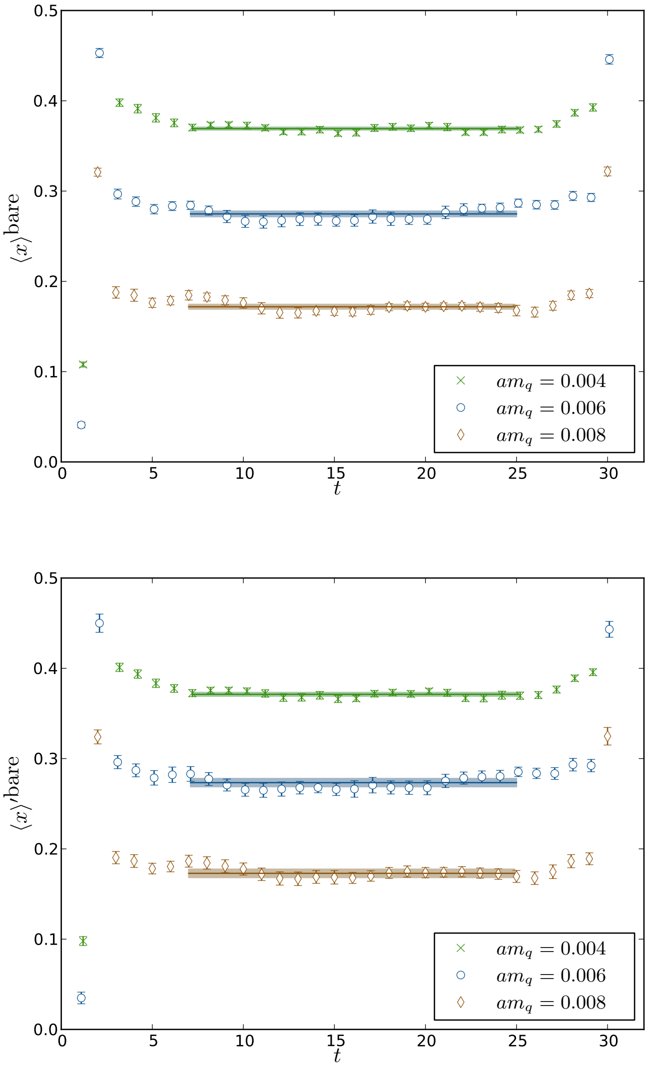

**Figure 8.3:** *Results for the* $\langle x\rangle^{bare}$ *using the* $\mathcal{O}_{v2,b}$ *operator. The top panel uses the three-point vector current in the denominator of the ratio whereas the bottom panel uses the two-point correlation function in the denominator. It should be noted that the* $am_q = 0.004$ *and* $0.006$ *datasets have been artificially shifted by* $0.1$ *and* $0.2$ *in the y-axis.*

| $am_q$ | 0.008 | 0.006 | 0.004 |
|---|---|---|---|
| $\langle x\rangle^{\text{bare}}_{C_{\mathcal{O}41}/C_{V1}}$ | 0.1686(43) | 0.1647(67) | 0.1682(30) |
| $\langle x\rangle^{\text{bare}}_{C_{\mathcal{O}41}/C_{V4}}$ | 0.1706(76) | 0.1703(67) | 0.1672(44) |
| $\langle x\rangle'^{\text{bare}}_{C_{\mathcal{O}41}/C_{2\text{pt}}}$ | 0.1722(62) | 0.1687(83) | 0.1682(43) |
| $\langle x\rangle^{\text{bare}}_{C_{\mathcal{O}44}/C_{V4}}$ | 0.1719(26) | 0.1747(30) | 0.1692(15) |
| $\langle x\rangle'^{\text{bare}}_{C_{\mathcal{O}41}/C_{2\text{pt}}}$ | 0.1729(46) | 0.1734(45) | 0.1712(21) |

**Table 8.2:** *Summary of results for the bare values of the structure function moments on the* $32^3$ *lattice. The errors are statistical. Note that results involving* $C_{2\text{pt}}$ *have been multiplied by* $Z_V = 0.0.74475(12)$ *[3] in anticipation of the renormalisation,* $\langle x\rangle^{bare\prime}_{C_{\mathcal{O}41}/C_{2\text{pt}}} = \langle x\rangle^{bare}_{C_{\mathcal{O}41}/C_{2\text{pt}}} Z_V$.

|  | Bare $\chi$-limit all | Bare $\chi$-limit avg | $\chi$-limit all | $\chi$-limit avg |
|---|---|---|---|---|
| $\langle x\rangle^{\text{bare}}_{C_{\mathcal{O}41}/C_{V/2\text{pt}}}$ | 0.1663(51) | 0.1656(55) | 0.2501(86) | 0.2491(91) |
| $\langle x\rangle^{\text{bare}}_{C_{\mathcal{O}44}/C_{V/2\text{pt}}}$ | 0.1675(31) | 0.1677(34) | 0.2485(62) | 0.2488(66) |

**Table 8.3:** *Bare and renormalised results at the chiral limit* $am_q + m_{res} = 0$*. The renormalised results are given in the* $\overline{MS}$ *scheme at* $\mu = 2$ *GeV.*

### 8.3.1 Quark Mass Extrapolation

One-loop chiral perturbation theory [106, 107] shows that the odd and even moments of the quark distributions extrapolate differently (in this work we calculate the first odd moment $\langle x\rangle$). For the forward moments of the pion quark distributions,

$$\langle x^n\rangle(m_\pi^2,\mu) = \begin{cases} c_0^{(n)}\left(1 - \frac{m_\pi^2}{(4\pi f_\pi)^2}\log\frac{m_\pi^2}{\mu^2}\right) + c_1^{(n)} m_\pi^2 & \text{even } n \\ c_0^{(n)} + c_1^{(n)} m_\pi^2 \qquad \text{odd } n \end{cases} \tag{8.15}$$

with corrections of $\mathcal{O}(m_\pi^4)$ where $c_i^{(n)}$ are low energy constants. For our extrapolation to the physical point, we perform the odd $n$ linear extrapolation in the light-quark mass (equivalent to $m_\pi^2$ eq. (5.11)). For both $\mathcal{O}_{v2,a}$ and $\mathcal{O}_{v2,b}$ we perform a single extrapolation after averaging the equivalent channels for each mass (each column in table 8.2, keeping $\mathcal{O}_{v2,a}$ and $\mathcal{O}_{v2,b}$ separate) before performing the extrapolation fig. 8.4 to determine our best answer. We also perform the extrapolation using the various channels fig. 8.5 to illustrate the spread of the points. Both methods provide very similar extrapolations and both sets of results are given in table 8.3.

The operators $\mathcal{O}_{v2,a}$ and $\mathcal{O}_{v2,b}$ transform under different irreducible representations of the hypercubic group, and so, whilst in the continuum, their results should agree, however, they will have different bare results and require different renormalisation constants. The renormalisation constants for the two operators were calculated in section 7 and presented in tables 7.8 and 7.10. The renormalised moments are given in table 8.3. The results using the two operators $\mathcal{O}_{v2,a}$ and $\mathcal{O}_{v2,b}$ agree within errors, which is true both before and after renormalisation. To strengthen any

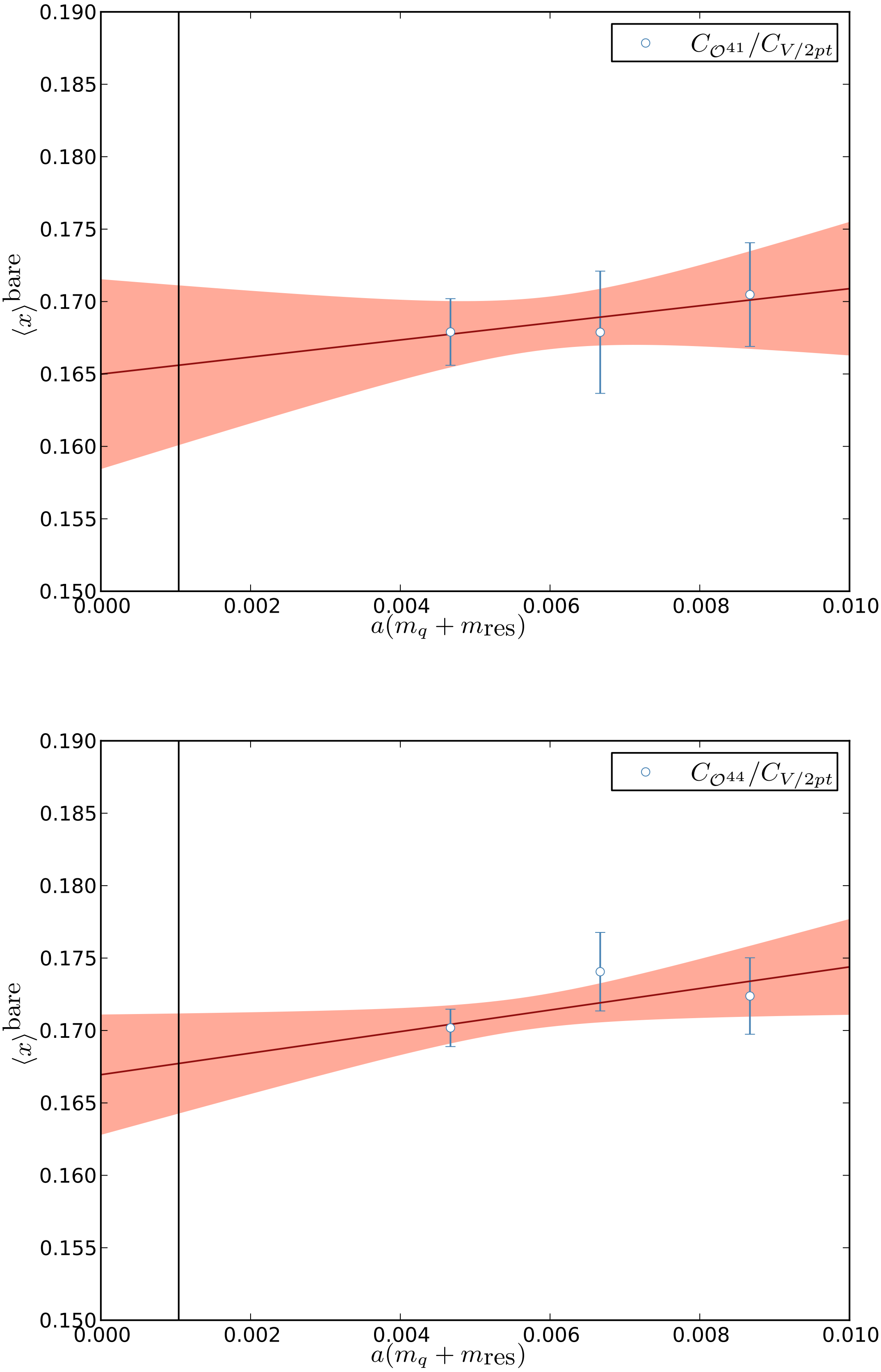

**Figure 8.4:** *Chiral extrapolations to the physical point* $a\tilde{m}_q$ *(table 6.1), corresponding to the physical pion mass, for the bare* $\langle x\rangle$ *moment after averaging all available channels for a given mass. For* $\mathcal{O}_{v2,a}$ *(top panel) and* $\mathcal{O}_{v2,b}$ *(bottom panel). The physical point is shown by the solid black line.*

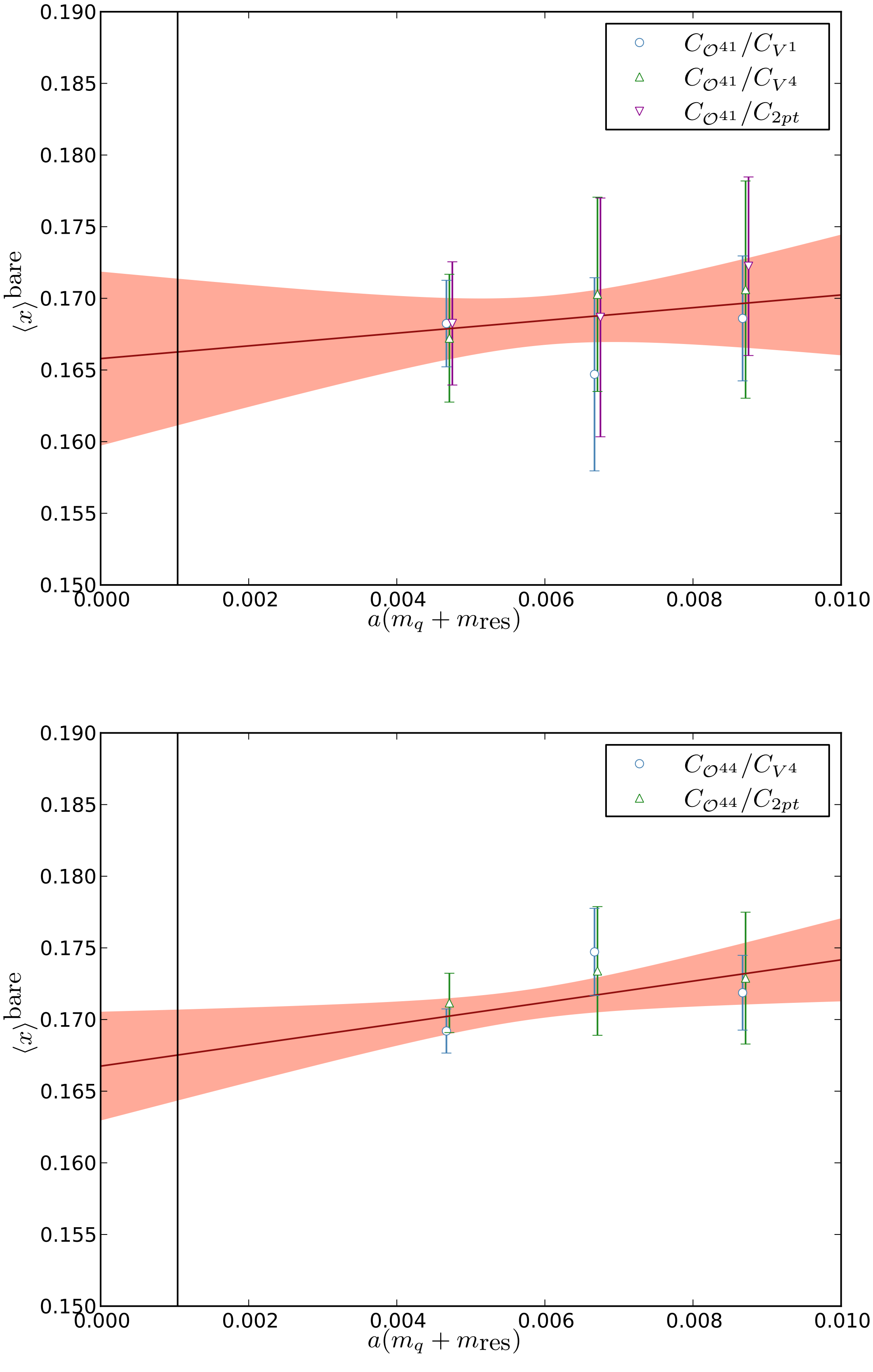

**Figure 8.5:** *Chiral extrapolations to the physical point $a\tilde{m}_q$ (table 6.1), corresponding to the physical pion mass, for the bare $\langle x \rangle$ moment including all available channels to demonstrate the variation. For $\mathcal{O}_{v2,a}$ (top panel) and $\mathcal{O}_{v2,b}$ (bottom panel). The physical point is shown by the solid black line.*

conclusion, an improvement in both the renormalisation errors, (which could be achieved through the use of twisted boundary conditions) and the bare results (through more statistics to reduce the errors) is required. For our best answer, we average our results for the two operators $\mathcal{O}_{v2,a}$ and $\mathcal{O}_{v2,b}$ (last column in table 8.3)

$$\langle x \rangle = 0.249(12),$$

given in the $\overline{\mathrm{MS}}$ scheme for $\mu = 2$ GeV. The error is both statistical and systematic from the continuum limit extrapolation and the renormalisation. $\langle x \rangle$ tells us that the light quarks inside the pion carry approximately 50% of the pion's momentum, the rest of which we attribute to the heavier quark generations and the gluons. It should be noted that the odd moment calculation is for a flavour singlet (the flavour non-singlet moment vanishes for degenerate light quark masses) and thus in principle there are disconnected contributions. These contributions are omitted from this calculation. This is yet to be calculated for the pion on the lattice, although currently the calculation of disconnected diagrams for nucleon structure functions is an active area of research, for which results from a quenched calculation using Wilson fermions can be found in [108]. A further caveat to the calculation is that there may also be a contribution from a $\mathrm{tr}(F_{\mu\rho}F^{\rho\nu})$ term occuring from the gluon contribution in the covariant derivative in the operator. The calculation of this contribution is both noisy and expensive, but it has been calculated for the pion in [109].

The original lattice investigations of the structure functions were performed in quenched calculations in the 1980s by Martinelli and Sachrajda [104]. More detailed and recent studies of the structure functions have been performed by the QCDSF collaboration in [105, 110]. Our results compare within errors to those obtained these papers (table 8.4).

| this work | QCDSF quenched [105] | QCDSF [110] | Martinelli et. al. [104] |
|---|---|---|---|
| 0.249(12) | 0.273(12) | 0.271(10) | 0.23(4) |

**Table 8.4:** *Comparison of renormalised structure function* $\langle x \rangle$ *moments. All are quoted in* $\overline{MS}$*. This work, Martinelli et Al. and QCDSF are given at* $\mu = 2$ *GeV, whereas QCDSF quenched is given at* $\mu = 2.4$ *GeV*

# Chapter 9

# Light Meson PDA - Results

## 9.1 Lattice Data

The PDA calculation was performed on all three lattices, thus allowing an evaluation of both finite volume and discretisation effects. For each of the masses in the three ensembles ($16^3 \times 32$, $24^3 \times 64$ and $32^3 \times 64$), details of the configurations are given in tables 9.1, 9.2 and 9.3 respectively. “Range” refers to the configuration ranges used and $\Delta$ provides the separation between configurations at the same source position $t_{src}$, both of which are given in molecular dynamics time units.

To improve statistics on the finite number of configurations available several calculations are performed on the same configuration but using a different location for the source in each case, which is equivalent to shifting the gauge fields. These are chosen so that the source positions extend along the lattice diagonal. For example, on the $24^3 \times 64$ and $32^3 \times 64$ ensembles, we have the source positions $(0, 0, 0, 0)$, $(8, 8, 8, 16)$, $(16, 16, 16, 32)$ and $(24, 24, 24, 48)$, where $t_{src}$ is the last entry in each and describes the source position of the time co-ordinate. The total number of measurements for a given light quark mass is thus $N_{meas} \times N_{t_{src}}$. We need to be wary of the strong correlations that measurements on a single gauge configuration have, and so we take the step of averaging these measurements together into a single “bin” before performing any statistical analysis or further calculations. For the $16^3$ ensemble, the span of measurements per bin was 50 molecular dynamics (MD)

| $am_q$ | Range | $N_{meas}$ | $\Delta$ | Smearing | $t_{src}$ |
|---|---|---|---|---|---|
| 0.01 | 500-3990 | 350 | 10 | GL-GL | 0, 8, 16, 24 |
| 0.02 | 500-3990 | 350 | 10 | GL-GL | 0, 8, 16, 24 |
| 0.03 | 4030-7600 | 358 | 10 | GL-GL | 0, 16 |

**Table 9.1:** *Parameters for the* $16^3 \times 32$ *PDA dataset* ($a^{-1} = 1.73(3)\,GeV$).

| $am_q$ | Range | $N_{meas}$ | $\Delta$ | Smearing | $t_{src}$ |
|---|---|---|---|---|---|
| 0.005 | 900-4480 | 180 | 20 | HL-HL | 0, 16, 32 |
| 0.01 | 800-3940 | 315 | 10 | GL-GL | 0, 32 |
| 0.02 | 1800-3580 | 90 | 20 | HL-HL | 0, 32 |
| 0.03 | 1260-3040 | 90 | 20 | HL-HL | 0, 32 |

**Table 9.2:** *Parameters for the* $24^3 \times 64$ *PDA dataset* ($a^{-1} = 1.73(3)\,GeV$).

timesteps. For the $24^3$ 0.005 and 0.01 masses, 80 MD were used, whereas 40 MD steps were used for the 0.02 and 0.03 masses in order to have a reasonable number of jackknife samples. Finally, for the $32^3$ ensemble, a span of 40 MD were used.

The smearing used for these calculations is of the form $XY - XY$ and denotes the contraction of two quark propagators, for which $X$ is the smearing type at the source, whereas $Y$ is the smearing at the sink. $X = L,\ G,\ H$ and $Y = L$ where $L$ refers to point/local smearing (i.e. no smearing), $G$ refers to a Gaussian form of radius $r = 4$ [111] for de-localising the source or sink, whereas $H$ smearing uses, instead, a Hydrogen S-wave form of radius $r = 3.5$ [112].

| $am_q$ | Range | $N_{meas}$ | $\Delta$ | Smearing | $t_{src}$ |
|---|---|---|---|---|---|
| 0.004 | 760-2410 | 120 | 10* | HL-HL | 0, 16, 32, 48 |
| 0.006 | 570-3240 | 134 | 20 | LL-LL | 0, 16, 32, 48 |
| 0.008 | 500-2960 | 56 | 40* | LL-LL | 0, 16, 32, 48 |

**Table 9.3:** *Parameters for the* $32^3 \times 64$ *PDA dataset* ($a^{-1} = 2.28(3)\,GeV$). *For* $*$ *entries* $\Delta$ *provides the average separation - these datasets have an irregular separation between adjacent measurements at the same source position. This is taken care of through binning.*

## 9.2 $\langle \xi^1 \rangle_P$ and $\langle \xi^2 \rangle_P$ from Ratios of Correlation Functions

We can extract the first and second moments of the pseudoscalar mesons from ratios of the following two-point correlation functions,

$$\begin{aligned}
C_{A_\mu P}(t,\mathbf{p}) &\equiv \sum_x e^{ip.x}\langle 0|A_\mu(t,\mathbf{x})P^\dagger(0)|0\rangle, && (9.1)\\
C^5_{\{\rho\mu\}}(t,\mathbf{p}) &\equiv \sum_x e^{ip.x}\langle 0|\mathcal{O}^5_{\{\rho\mu\}}(t,\mathbf{x})P^\dagger(0)|0\rangle, && (9.2)\\
C^5_{\{\rho\mu\nu\}}(t,\mathbf{p}) &\equiv \sum_x e^{ip.x}\langle 0|\mathcal{O}^5_{\{\rho\mu\nu\}}(t,\mathbf{x})P^\dagger(0)|0\rangle, && (9.3)
\end{aligned}$$

which at large Euclidean times $t$ and $T-t$, tend towards

$$\begin{aligned}
C_{A_\mu P}(t,\mathbf{p}) &\rightarrow \frac{Z_P f_P^{\text{bare}} e^{-E_P T/2}\sinh((t-T/2)E_P)}{E_P}\, ip_\mu, && (9.4)\\
C^5_{\{\rho\mu\}}(t,\mathbf{p}) &\rightarrow\ , \frac{Z_P f_P^{\text{bare}} e^{-E_P T/2}\sinh((t-T/2)E_P)}{E_P}\, ip_\rho\; ip_\mu \langle \xi^1\rangle^{\text{bare}}, && (9.5)\\
C^5_{\{\rho\mu\nu\}}(t,\mathbf{p}) &\rightarrow \frac{Z_P f_P^{\text{bare}} e^{-E_P T/2}\sinh((t-T/2)E_P)}{E_P}\, ip_\rho\; ip_\mu\; ip_\nu \langle \xi^2\rangle^{\text{bare}}, && (9.6)
\end{aligned}$$

where $Z_P \equiv \langle P(p)|P^\dagger|0\rangle$ and the bare decay constant is defined via the matrix element $\langle 0|A_\nu|P(p)\rangle \equiv ip_\nu f_P^{\text{bare}}$. It proves convenient to take eq. (9.5) and eq. (9.6) as separate ratios with eq. (9.4). This helps to isolate the bare moments and remove factors such as $f_P^{\text{bare}}$ and $Z_P$.

$$\begin{aligned}
R^P_{\{\rho\mu\};\nu}(t,\mathbf{p}) &\equiv \frac{C^5_{\{\rho\mu\}}(t,\mathbf{p})}{C_{A_\nu P}(t,\mathbf{p})} \rightarrow i\frac{p_\rho p_\mu}{p_\nu}\langle \xi^1\rangle^{\text{bare}}, && (9.7)\\
R^P_{\{\rho\mu\nu\};\sigma}(t,\mathbf{p}) &\equiv \frac{C^5_{\{\rho\mu\nu\}}(t,\mathbf{p})}{C_{A_\sigma P}(t,\mathbf{p})} \rightarrow -\frac{p_\rho p_\mu p_\nu}{p_\sigma}\langle \xi^2\rangle^{\text{bare}}. && (9.8)
\end{aligned}$$

We then need only to consider the momentum factors, bearing in mind the mixing discussion of section 6.7. For the first moment, we chose $R^P_{\{\rho,4\};4}(t,\mathbf{p})$ where 4 corresponds to the time direction and $\rho$ may take spatial values for which we require a single non-zero unit of momentum $|p_\rho| = 2\pi/L$. For the second moment, $R^P_{\{\rho\mu 4\};4}(t,\mathbf{p})$ where $\rho \neq \mu$ and thus two non-zero units of momenta $|p_\rho| = |p_\mu| = 2\pi/L$ are required.

## 9.3 $\langle \xi^1 \rangle_V^{\parallel}$ and $\langle \xi^2 \rangle_V^{\parallel}$ from Ratios of Correlation Functions

The longitudinally polarised vector mesons are treated analogously to the pseudoscalars; the two-point correlation functions are:

$$\begin{aligned}
C_{V_\mu V_\nu}(t,\mathbf{p}) &\equiv \sum_x e^{ip.x}\langle 0|V_\mu(t,\mathbf{x})V_\nu^\dagger(0)|0\rangle && (9.9)\\
C_{\{\rho\mu\}\nu}(t,\mathbf{p}) &\equiv \sum_x e^{ip.x}\langle 0|\mathcal{O}_{\{\rho\mu\}}(t,\mathbf{x})V_\nu^\dagger(0)|0\rangle && (9.10)\\
C_{\{\rho\mu\nu\}\sigma}(t,\mathbf{p}) &\equiv \sum_x e^{ip.x}\langle 0|\mathcal{O}_{\{\rho\mu\nu\}}(t,\mathbf{x})V_\sigma^\dagger(0)|0\rangle && (9.11)
\end{aligned}$$

where the bare longitudinal decay constant for a vector meson, with polarisation index $\lambda$ and polarisation vector $\epsilon$ is defined through the matrix element $\langle 0|V_\mu|V(p,\lambda)\rangle \equiv f_V^{\mathrm{bare}} m_V \epsilon_\mu^{(\lambda)}$. For large Euclidean times $t$ and $T-t$,

$$\begin{aligned}
C_{V_\mu V_\nu}(t,\mathbf{p}) &\to \frac{-(f_V^{\mathrm{bare}}m_V)^2 e^{-E_V T/2}\cosh((t-T/2)E_V)}{E_V}\\
&\quad\cdot\left(-g_{\mu\nu}+\frac{p_\mu p_\nu}{m_V^2}\right) && (9.12)
\end{aligned}$$

$$\begin{aligned}
C_{\{\rho\mu\}\nu}(t,\mathbf{p}) &\to \frac{-i(f_V^{\mathrm{bare}}m_V)^2 e^{-E_V T/2}\langle\xi^1\rangle^{\parallel\mathrm{bare}}\sinh((t-T/2)E_V)}{E_V}\\
&\quad\cdot\frac{1}{2}\left(-g_{\rho\nu}p_\mu-g_{\mu\nu}p_\rho+\frac{2p_\rho p_\mu p_\nu}{m_V^2}\right) && (9.13)
\end{aligned}$$

$$\begin{aligned}
C_{\{\rho\mu\nu\}\sigma}(t,\mathbf{p}) &\to \frac{(f_V^{\mathrm{bare}}m_V)^2 e^{-E_V T/2}\langle\xi^2\rangle^{\parallel\mathrm{bare}}\sinh((t-T/2)E_V)}{E_V}\\
&\quad\cdot\frac{1}{3}\left(-g_{\rho\sigma}p_\mu p_\nu-g_{\mu\sigma}p_\rho p_\nu-g_{\nu\sigma}p_\rho p_\mu+\frac{3p_\rho p_\mu p_\nu p_\sigma}{m_V^2}\right) && (9.14)
\end{aligned}$$

where we have used the completeness relation for the polarisation vectors $\sum_\lambda \epsilon_\mu^{(\lambda)}\epsilon_\nu^{*(\lambda)} = -g_{\mu\nu}+p_\mu\, p_\nu/m_V^2$. Eqs. (9.12)-(9.14) may be used to construct the following ratios

$$\begin{aligned}
R^V_{\{\rho\mu\}\nu}(t,\mathbf{p}) &\equiv \frac{C_{\{\rho\mu\}\nu}(t,\mathbf{p}=0)}{\frac{1}{3}\sum_i C_{V_iV_i}(t,\mathbf{p}=0)} \to -i\langle\xi^1\rangle^{\|\text{bare}}\tanh((t-T/2)E_V) \\
&\quad\cdot\frac{1}{2}\left(-g_{\rho\nu}p_\mu - g_{\mu\nu}p_\rho + \frac{2p_\rho p_\mu p_\nu}{m_V^2}\right) \qquad (9.15) \\
R^V_{\{\rho\mu\nu\}\sigma}(t,\mathbf{p}) &\equiv \frac{C_{\{\rho\mu\nu\}\sigma}(t,|\mathbf{p}|=\frac{2\pi}{L})}{\frac{1}{3}\sum_i C_{V_iV_i}(t,|\mathbf{p}|=\frac{2\pi}{L})} \to \langle\xi^2\rangle^{\|\text{bare}}\tanh((t-T/2)E_V) \\
&\quad\cdot\frac{1}{3}\left(-g_{\rho\sigma}p_\mu p_\nu - g_{\mu\sigma}p_\rho p_\nu - g_{\nu\sigma}p_\rho p_\mu + \frac{3p_\rho p_\mu p_\nu p_\sigma}{m_V^2}\right) \qquad (9.16)
\end{aligned}$$

where the index $i$ runs over the spatial indices. The first moment can be extracted with $R^V_{\{\rho 4\}\nu}(t,\mathbf{p}=0)$ where $\mu=4$ and $\rho=\nu=1,2,3$ and the second through $R^V_{\{\rho\mu\nu\}\sigma}(t,\mathbf{p})$ for a choice of indices where $\rho$, $\nu$ and $\mu$ are distinct and different and $\mu=\sigma$ for which we require a single unit of non-zero momenta. These choices simplify the structure of eqs. (9.15) and (9.16) so that all but one of the terms within the large parentheses become zero.

In principle, we should think about contributions from disconnected diagrams to our correlation functions. For the $K$ and $K^*$ mesons, there are no such contributions due to the asymmetry in the quark content. The $\pi$ and $\rho$ mesons are isospin triplets and therefore also avoid any contributions in our isospin conserving calculations. For the case where $m_u = m_d$ there is an explicit cancellation of disconnected diagrams for the $\pi^0$ and $\rho^0$ mesons. We should, however, consider the disconnected diagram contributions to the $\phi$ meson, however this is Zweig suppressed and is neglected in this calculation. This would be an interesting extension for the calculation but would be a computationally challenging one.

## 9.4 16 and 24 Results - Finite Volume Effects

The work presented in this section builds upon the calculations performed in the thesis [92]. The first moment calculations have been independently checked in this work and the results agree with those in [92, 102]. The second moment calculations presented in here are new. The combined results for the first and second moments of the light-meson distribution amplitudes have been presented in a recent publication [1].

To extract the first moment of the PDAs for the kaon, eq. (9.7), with the indices

$$R^P_{\{\rho 4\};4}(t,\mathbf{p}) = i\left(\pm\frac{2\pi}{L}\right)\langle\xi^1\rangle, \qquad \rho = 1,2,3, \tag{9.17}$$

requires both two-point correlation functions in the ratio to have one unit of momentum. In order to fully make use of the statistics available (and to treat all directions equivalently), we average over the three spatial directions for both positive and negative choices of momenta $[p_\rho = (0,0,\frac{+2\pi}{L}),\ (0,0,\frac{-2\pi}{L}),\ (0,\frac{+2\pi}{L},0)...]$ (6 in total).

For the $K^*$ meson, eq. (9.15),

$$R^V_{\{\rho 4\};\nu}(t,\mathbf{p}=0) = -2iE_V\langle\xi^1\rangle^{\parallel}\tanh((t-T/2)E_V), \qquad \rho=\nu=1,2,3, \tag{9.18}$$

we are able to consider the two-point correlation functions with zero momentum, for which we average $C_{V_iV_i}$ over the three spatial dimensions and $C_{\{\rho 4\}\nu}$ over the three choices $C_{\{41\}1}$, $C_{\{42\}2}$ and $C_{\{43\}3}$. The results for the kaon and $K^*$ are shown for the $16^3$ and $24^3$ emsembles in figs. 9.1 and 9.2 respectively.

The second moment for the pseudoscalar $\pi$ and $K$ mesons, eq. (9.8),

$$R^P_{\{\rho\mu 4\};4}(t,\mathbf{p}) = -\left(\pm\frac{2\pi}{L}\right)\left(\pm\frac{2\pi}{L}\right)\langle\xi^2\rangle, \qquad \mu\neq\rho \tag{9.19}$$

require correlation functions with two non-zero components of momentum. Once again, we average over all possible choices for the momentum with two non-zero components
$[p_\mu = (\frac{+2\pi}{L},\frac{+2\pi}{L},0),\ (\frac{+2\pi}{L},\frac{-2\pi}{L},0),\ (\frac{-2\pi}{L},\frac{+2\pi}{L},0),\ (\frac{-2\pi}{L},\frac{-2\pi}{L},0),\ (\frac{+2\pi}{L},0,\frac{+2\pi}{L}),\ ...]$.
The second moment for the vector, eq. (9.16),

$$R^V_{\{\rho\mu 4\}\sigma}(t,\mathbf{p}) = \frac{4}{3}E_V\left(\pm\frac{2\pi}{L}\right)\langle\xi^2\rangle^{\parallel}\tanh((t-T/2)E_V), \qquad \rho=\nu=1,2,3, \tag{9.20}$$

requires the correlation functions to have a single non-zero unit of momentum. For the numerator, we average over all combinations of $C_{\{4ij\}j}$ where $p_j = \pm 2\pi/L$ and

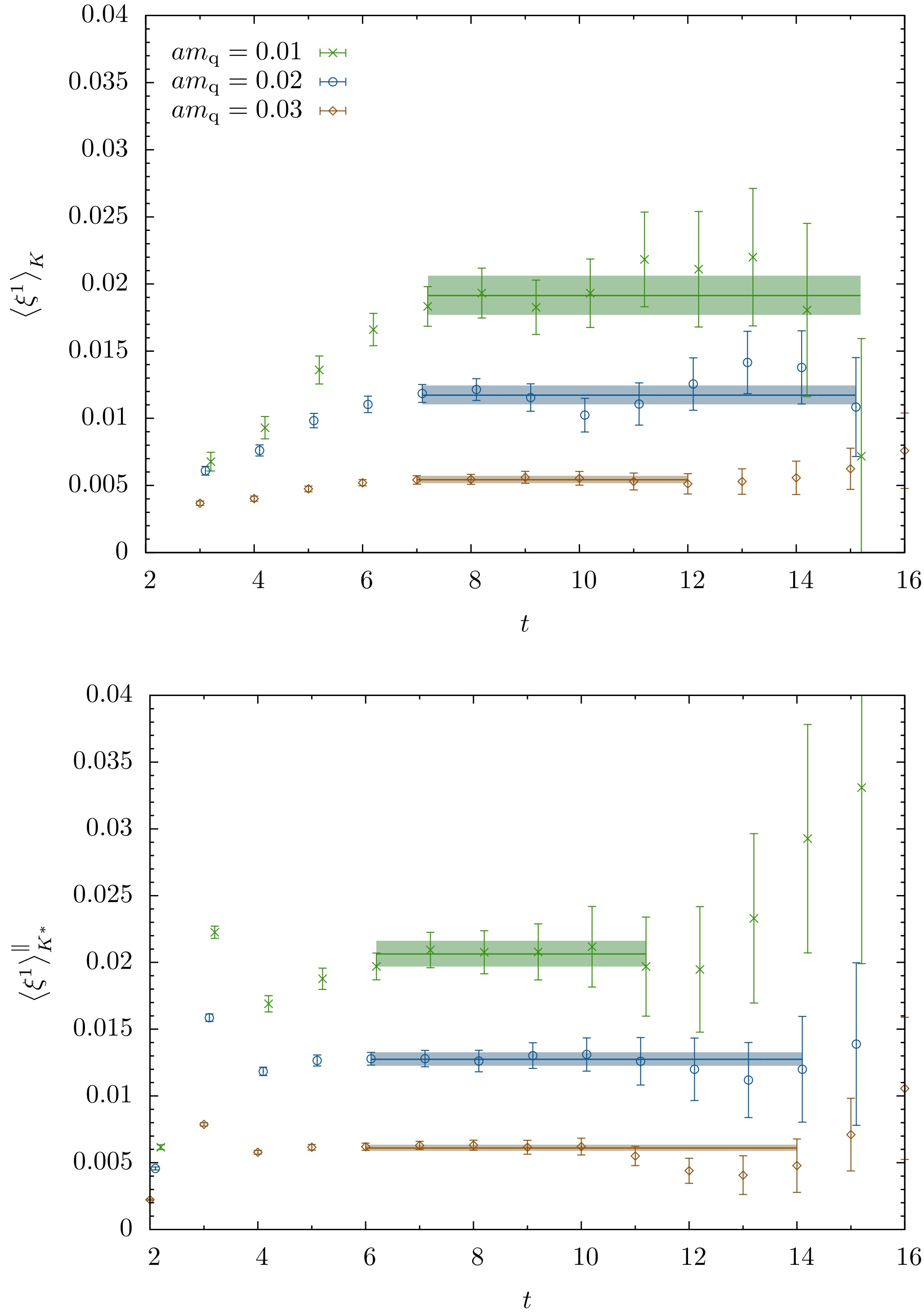

**Figure 9.1:** *Results for the* $\langle \xi^1 \rangle_K^{bare}$ *(top panel) and* $\langle \xi^1 \rangle_{K^*}^{\parallel bare}$ *(bottom panel) for the* $16^3$ *ensembles. The shaded area gives the fit-range, fitted values and errors [1].*

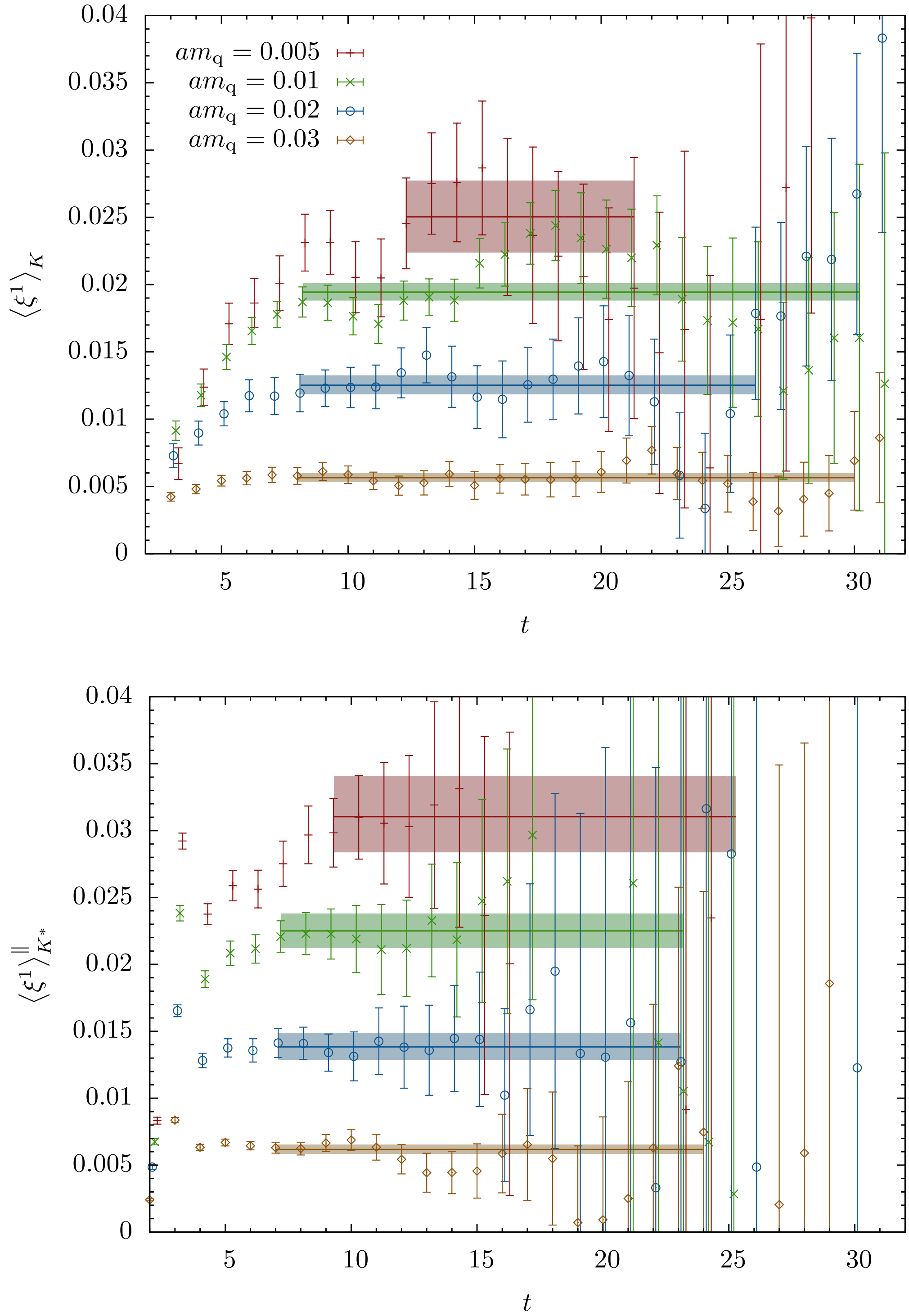

**Figure 9.2:** *Results for the* $\langle\xi^1\rangle_K^{bare}$ *(top panel) and* $\langle\xi^1\rangle_{K^*}^{\parallel\,bare}$ *(bottom panel) for the* $24^3$ *ensembles. The shaded area gives the fit-range, fitted values and errors [1].*

$|\mathbf{p}| = 2\pi/L$ and, for the denominator, we average the four momentum choices for each of the three spatial directions so that $\sum_i C_{V_iV_i}(p_i = 0, |\mathbf{p}| = 2\pi/L)$. The results for the pion and kaon second moments of the distribution amplitudes for the $16^3$ and $24^3$ ensembles are contained in figs. 9.3 and 9.4 respectively.

The bare values for the first and second moments for the pseudoscalar mesons are extracted through constant fits of the form of eqs. (9.7) and (9.8), for which there is no dependence on time, other than waiting for the contribution from excited states to decay. The vector meson moments have an explicit dependence upon time through the $\tanh((t - T/2)E_V)$ function. This dependence is however mild over the intermediate time range where we wish to fit the data. An added difficulty for the vector meson fit is the energy, $E_V$, required to extract the moments, which we extract from a fit to the two-point function found in the denominator of the ratios. To aid the determination of the start of the plateaus, we considered the correlation function of the numerator and denominator separately through effective mass plots, which allowed us to identify and exclude the region where excited states still contributed. In the worst cases, where looking at the numerator and denominator separately does not aid the fitting due to increased noise, we fit as soon as there is a hint of a plateau in order to have as large a plateau as possible. This can also be guided somewhat by the start of the plateaus from the other masses of the same quantity, but this could however lead to fit-ranges which mistakenly involve excited states, which we want to avoid. Another aspect of fitting which we should be cautious of is that the detailed procedure is based upon a somewhat “by-eye” approach and so suffers from the bias of the fitter. In order to provide a check of our fitting, a method for automated fitting was devised in which the routine ranks all possible fit-ranges by the magnitude of the gradient for a $y = mx + c$ fit to the data. The central value for the moment is extracted using the fit-range with the smallest gradient to determine the usual plateau fit of the form $y = c$. This method can also provide a fitting error through taking the variance over, say, the first 20 ranked results of the fits. The results from this technique, in most cases, agreed with our “by-eye” ranges and provided an extra check. Using all of this information as a guide we could then pick a fit range that produced a stable result with respect

| $am_{ud}$ | 0.03 | 0.02 | 0.01 | 0.005 | $\chi$-limit |
|---|---|---|---|---|---|
| $\langle \xi^2 \rangle_{\pi}^{\text{bare}}$ | 0.110(2) | 0.109(2) | 0.113(4) | - | 0.112(5) |
| $\langle \xi^1 \rangle_{K}^{\text{bare}}$ | 0.00543(27) | 0.01174(71) | 0.0194(15) | - | 0.0228(14)(11) |
| $\langle \xi^2 \rangle_{K}^{\text{bare}}$ | 0.109(2) | 0.107(2) | 0.113(3) | - | 0.112(4) |
| $\langle \xi^2 \rangle_{\rho}^{\parallel\ \text{bare}}$ | 0.113(4) | 0.100(5) | 0.116(6) | - | 0.109(10) |
| $\langle \xi^1 \rangle_{K^*}^{\parallel\ \text{bare}}$ | 0.00610(24) | 0.01275(51) | 0.0207(10) | - | 0.02443(96)(107) |
| $\langle \xi^2 \rangle_{K^*}^{\parallel\ \text{bare}}$ | 0.111(4) | 0.101(4) | 0.113(4) | - | 0.110(6) |
| $\langle \xi^2 \rangle_{\phi}^{\parallel\ \text{bare}}$ | 0.109(3) | 0.100(3) | 0.109(3) | - | 0.107(5) |

**Table 9.4:** *Summary of results for the bare values of the distribution amplitude moments on the* $16^3$ *lattices. The errors are statistical and (in the first moment case) systematic due to the uncertainty in the physical point for the chiral extrapolation [1].*

| $am_{ud}$ | 0.03 | 0.02 | 0.01 | 0.005 | $\chi$-limit |
|---|---|---|---|---|---|
| $\langle \xi^2 \rangle_{\pi}^{\text{bare}}$ | 0.103(9) | 0.104(6) | 0.114(3) | 0.121(9) | 0.125(7) |
| $\langle \xi^1 \rangle_{K}^{\text{bare}}$ | 0.00566(33) | 0.01254(72) | 0.01946(65) | 0.0231(15) | 0.02377(71)(110) |
| $\langle \xi^2 \rangle_{K}^{\text{bare}}$ | 0.103(8) | 0.106(4) | 0.112(2) | 0.113(6) | 0.117(5) |
| $\langle \xi^2 \rangle_{\rho}^{\parallel\ \text{bare}}$ | 0.110(9) | 0.093(10) | 0.112(3) | 0.120(13) | 0.118(7) |
| $\langle \xi^1 \rangle_{K^*}^{\parallel\ \text{bare}}$ | 0.00619(35) | 0.0139(10) | 0.0225(13) | 0.0311(30) | 0.0281(13)(14) |
| $\langle \xi^2 \rangle_{K^*}^{\parallel\ \text{bare}}$ | 0.109(12) | 0.095(8) | 0.108(3) | 0.117(5) | 0.118(7) |
| $\langle \xi^2 \rangle_{\phi}^{\parallel\ \text{bare}}$ | 0.108(7) | 0.097(7) | 0.105(2) | 0.107(3) | 0.107(4) |

**Table 9.5:** *Summary of results for the bare values of the distribution amplitude moments on the* $24^3$ *lattices. The errors are statistical and (in the first moment case) systematic due to the uncertainty in the physical point for the chiral extrapolation [1].*

to small variations in the lower limit of the fit range whilst aiming for a good $\chi^2$/d.o.f.. The results for the bare moments of the PDAs extracted from the plateau fits are contained in Tables 9.4 and 9.5

## 9.5 Quark Mass Extrapolations

Current simulations are unable to simulate at masses as low as the physical up and down quarks. In order to access the physical light (up and down) quark mass the technique that is employed is to simulate instead with a range of un-physical light quark masses, so that an extrapolation may be made down to the physical value. Chiral perturbation theory is used to guide this extrapolation. For $SU(3)$ chiral perturbation theory, at leading order, the first moment for the kaon is proportional

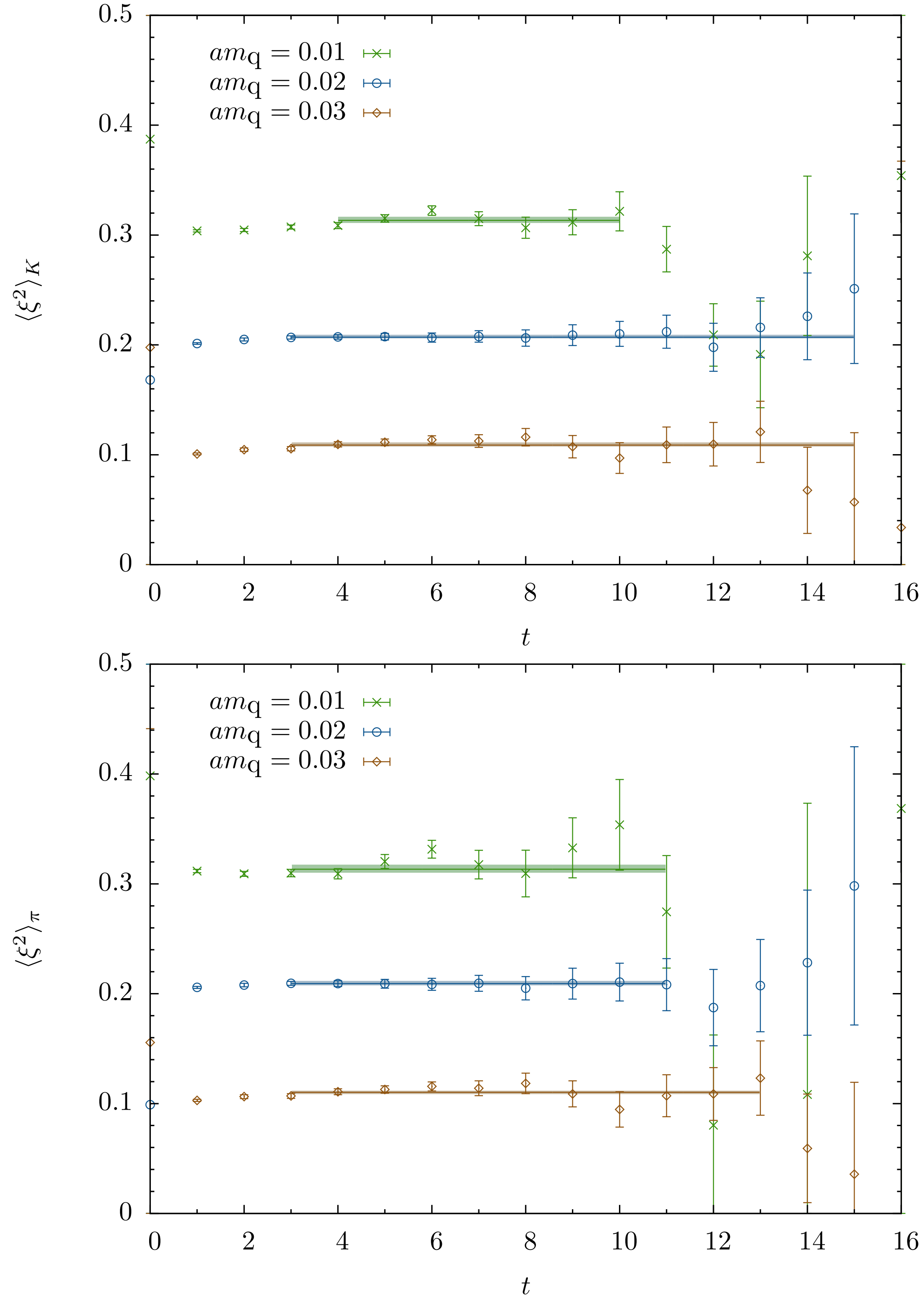

**Figure 9.3:** *Results for the* $\langle\xi^2\rangle_K^{bare}$ *(top panel) and* $\langle\xi^2\rangle_\pi^{bare}$ *(bottom panel) for the* $16^3$ *ensembles. The shaded area gives the fit-range, fitted values and errors. Note that, except for the heaviest data-set, each successive mass from bottom-to-top has been offset incrementally by* 0.1 *in the* $y$*-axis.*

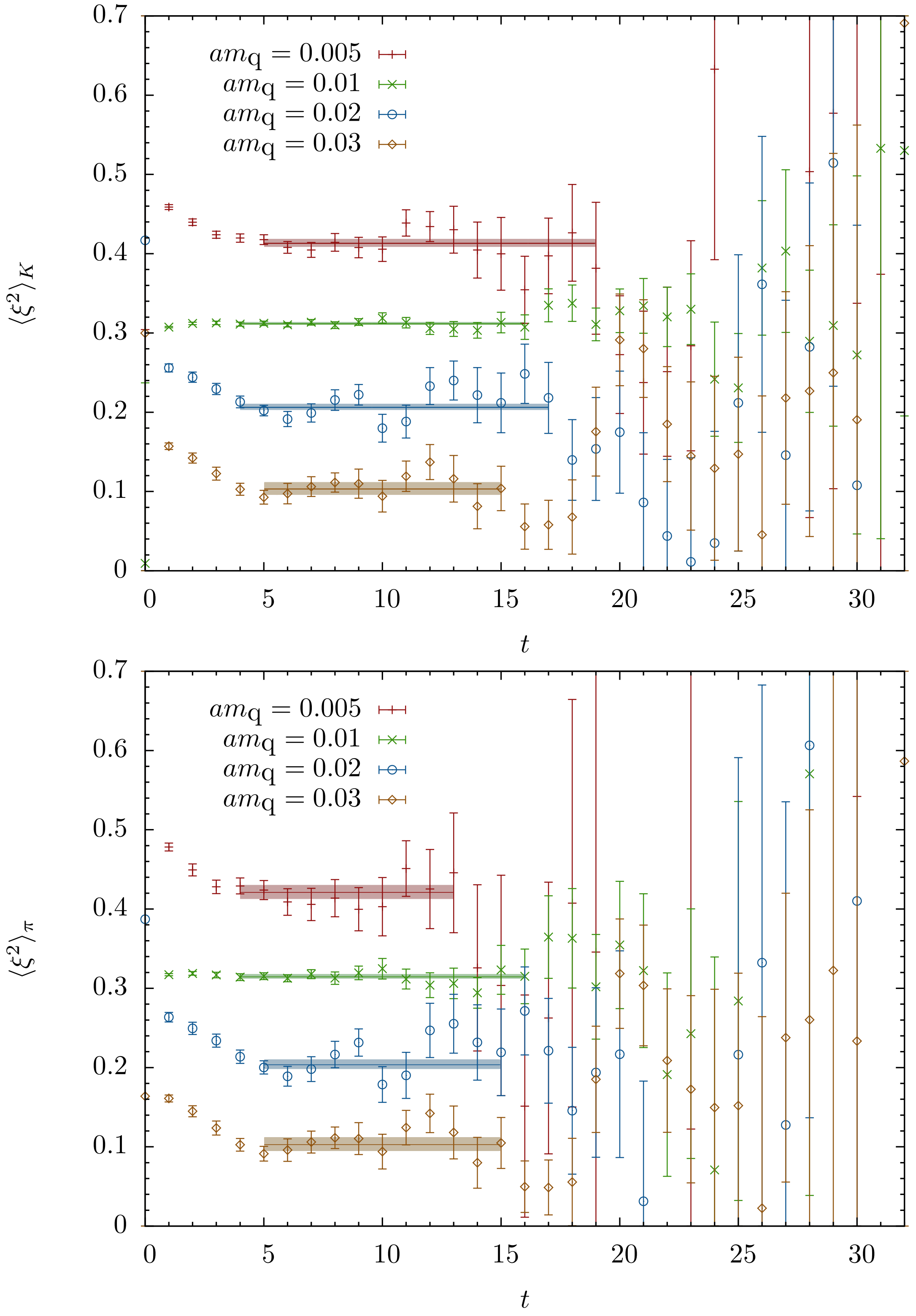

**Figure 9.4:** *Results for the* $\langle\xi^2\rangle_K^{bare}$ *(top panel) and* $\langle\xi^2\rangle_\pi^{bare}$ *(bottom panel) for the* $24^3$ *ensembles. The shaded area gives the fit-range, fitted values and errors. Note that, except for the heaviest data-set, each successive mass from bottom-to-top has been offset incrementally by* 0.1 *in the* $y$*-axis.*

to the difference between the light and strange quark masses [113],

$$\langle \xi^1 \rangle_K = \frac{8B_0}{f^2}\,(m_s - m_q)\,b_{1,2}, \tag{9.21}$$

where $B_0$ and $f^2$ are low energy constants from chiral perturbation theory and $b_{1,2}$ is a Wilson coefficient introduced in [113]. Our data for the first moments clearly show the expected $SU(3)$ breaking effects, which provide the non-zero first moment for the kaon (and $K^*$). In our simulations the strange mass is (nearly) correct and so we extrapolate in the light $u$ and $d$ quark masses. An observation of our collaboration's recent work is that the strange mass is too large for low order chiral perturbation theory, and that we should use $SU(2)$ chiral perturbation theory instead. $SU(2)$ chiral perturbation theory provides explicit $u$- and $d$- quark dependence where the strange quark mass is hidden in the low energy constants. We expect that, for both $SU(3)$ and $SU(2)$ chiral perturbation theory, when $m_q = m_s$ the first moment should vanish, but this need not be the case for the leading terms in the $SU(2)$ chiral expansion. Our chiral extrapolation for the first moment kaon is therefore performed linearly in $a(m_s - m_q)$ (or equivalently $m_K^2 - m_\pi^2$) to the physical point without constraining the moment to vanish in the $SU(3)$ limit. We use the same extrapolation for the $K^*$. Whilst this is not a prediction of chiral perturbation theory, the data does, however, exhibit the same light-quark mass dependence as for the kaon. The extrapolations for both of these are presented in fig. 9.5. The vertical solid black line represents the physical point for the extrapolation; the dotted vertical lines indicate the error on this point which stems form the uncertainty in the strange quark mass (and to a lesser extent the light quark mass) contained in table 6.1. This error translates as the second error in the chiral limit ($\chi$-limit) results contained in tables 9.4 and 9.5. This treatment simultaneously takes account of the strange quark mass extrapolation necessitated by $\sim 15\%$ too large strange quark and the light quark mass extrapolation detailed above.

For the second moments, we learn from $SU(3)$ chiral perturbation theory at one

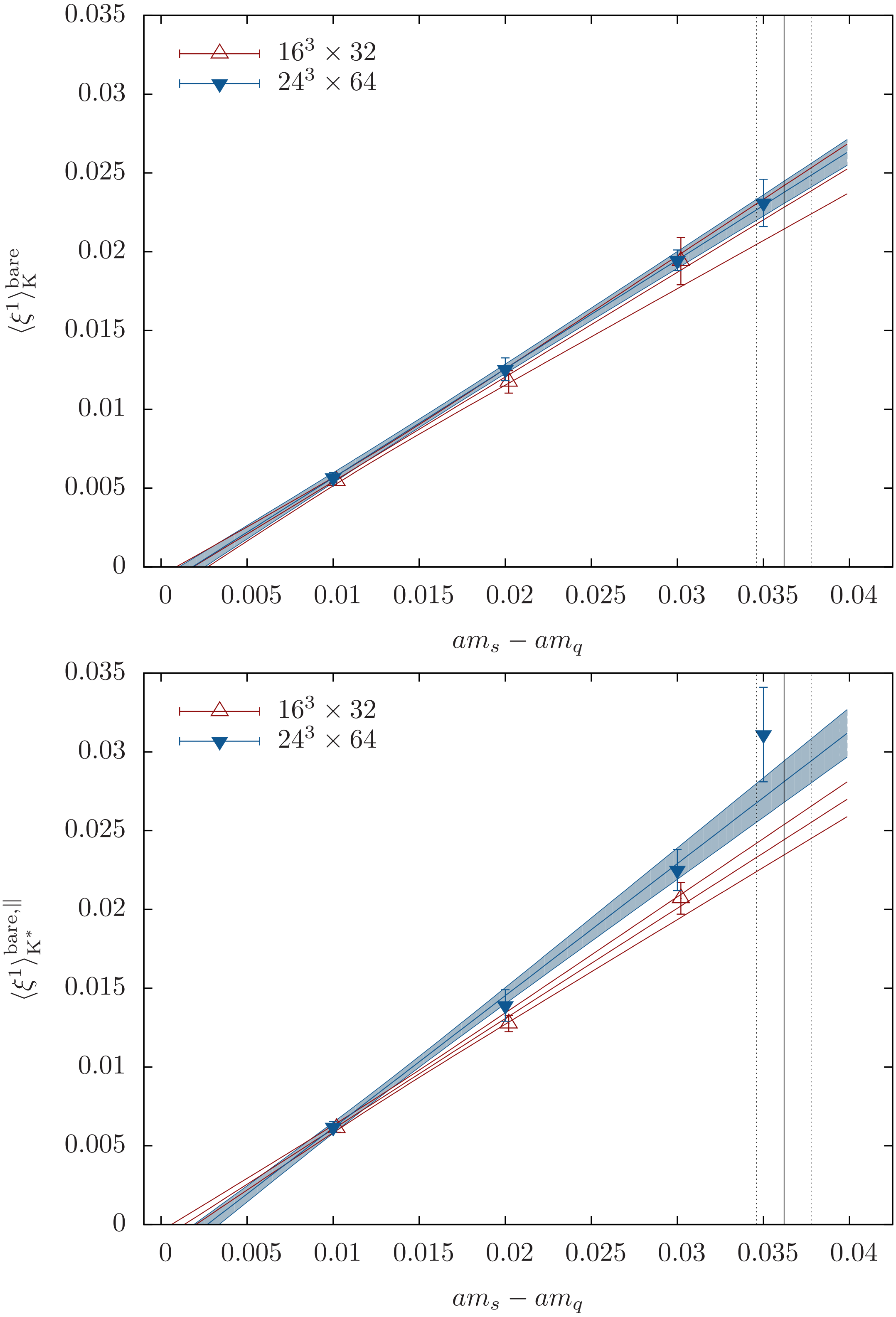

**Figure 9.5:** *Chiral extrapolations to the physical point for the bare first moments* $\langle\xi^1\rangle_K^{\mathrm{bare}}$ *(top panel) and* $\langle\xi^1\rangle_{K^*}^{bare\|}$ *(bottom panel). The physical point is shown by the vertical solid line, with uncertainty, dominated by the uncertainty in the physical strange mass, indicated by the dotted lines [1].*

loop [113] that,

$$\begin{aligned} \langle\xi^2\rangle_\pi &= \langle\xi^2\rangle_0 + \alpha_2 2m_q + \beta_2\left(2m_q + m_s\right) && (9.22)\\ \langle\xi^2\rangle_K &= \langle\xi^2\rangle_0 + \alpha_2\left(m_q + m_s\right) + \beta_2\left(2m_q + m_s\right) && (9.23)\end{aligned}$$

where $\langle\xi^2\rangle_0$ is the chiral limit value and $\alpha_2$ and $\beta_2$ are coefficients that contain low energy constants and Wilson coefficients. The behaviour is analytic, and suggests that we should fit linearly in $m_q$ (or equivalently $m_\pi^2$), once again neglecting the fixed heavy strange quark mass. The chiral extrapolations for the second moment pseudoscalar mesons are presented in fig. 9.6 from which we see that any dependence in the light-quark mass is very mild. We perform the same extrapolation for the vector second moments, fig. 9.7, motivated by their analogous behaviour. Taken together, the $16^3$ and $24^3$ ensemble results provide an indication of possible finite volume effects. However, other than a hint for the $K^*$ first moment at the chiral limit, any such effects seem to be absent for the first two moments. Where there are points from the two ensembles at similar mass values, the values for the $K^*$ agree within statistical uncertainties.

## 9.6 $32^3$ Results - Discretisation Effects

The bare moments for the $32^3$ ensemble are extracted using the same method as for the $24^3$ ensemble, eqns. (9.17)-(9.20), and can be extrapolated to the physical point as before using the chiral perturbation results, eqns. (9.21)-(9.23). Once both sets of data have been renormalised, comparisons can be made and a better idea of the continuum behaviour and discretisation effects associated with these quantities may be determined. The initial measurement runs for this calculation were performed on the QCDOC computers [78–80]. However, in the preceding analysis, it was noted that the were insufficient statistics for the heaviest two masses, 0.008 and 0.006, for which we increased the number of measurements by approximately 30% and 80% respectively. These additional runs exhausted the available configurations with the aim of improving the available statistics to a reliable level from which plateaus

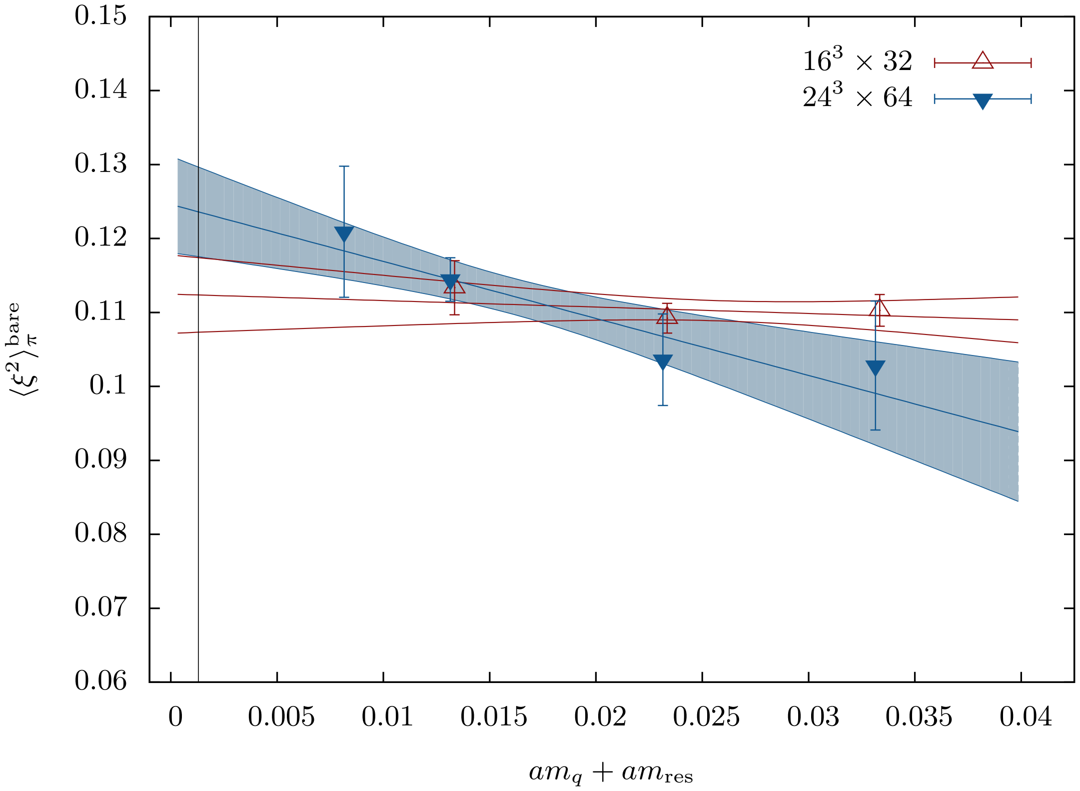

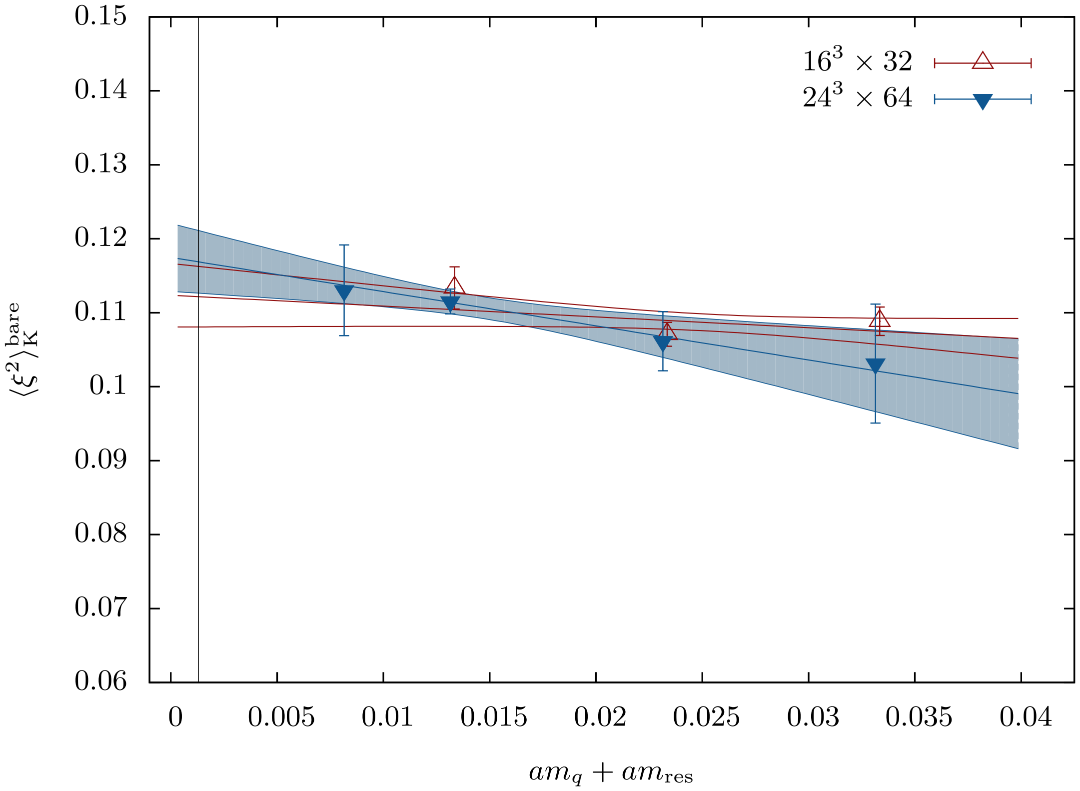

**Figure 9.6:** *Chiral extrapolations to the physical point* $a\tilde{m}_q$ *(table 6.1), corresponding to the physical meson mass, for the bare second moments for the pseudoscalar mesons. The physical value for* $am_q + am_{res}$ *is shown by the solid vertical line in each case [1].*

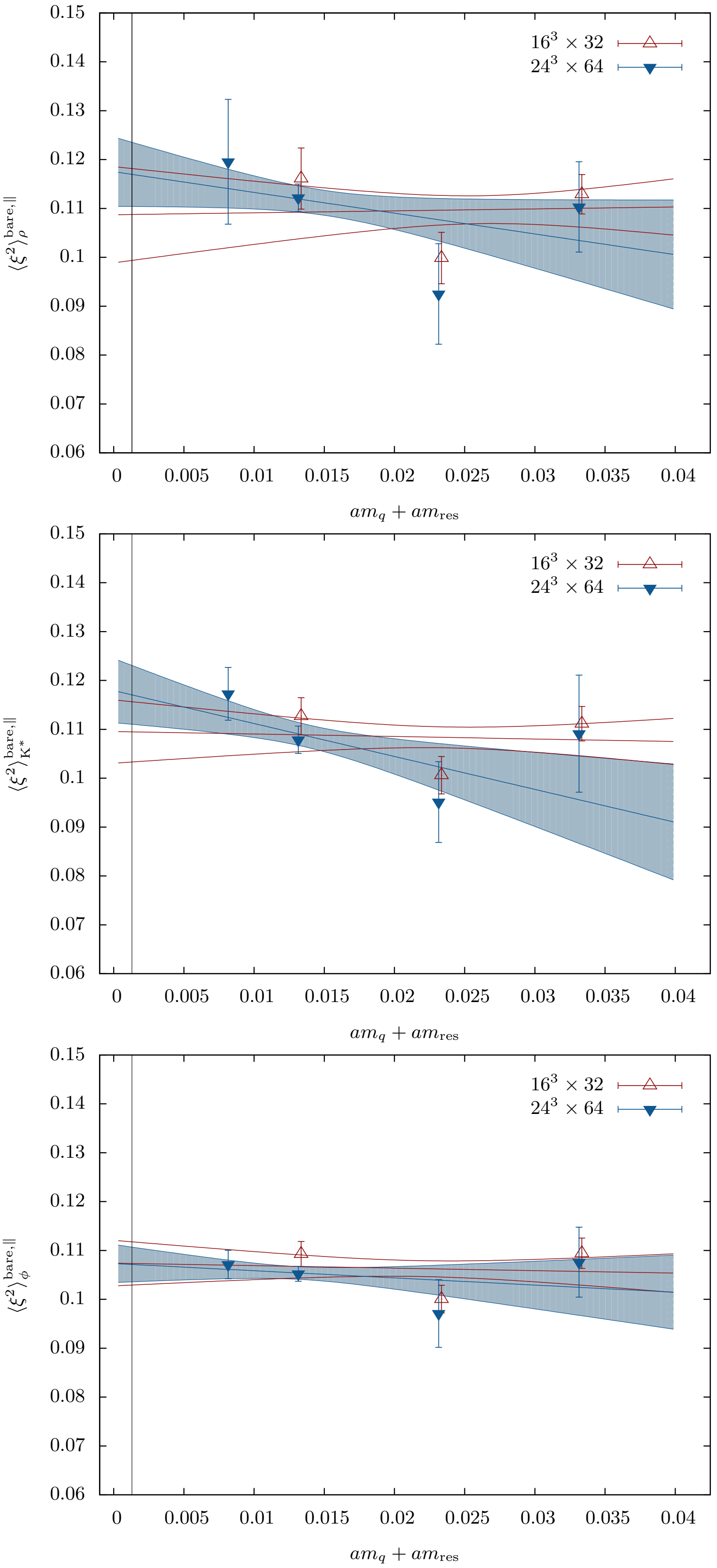

**Figure 9.7:** *Chiral extrapolations to the physical point $a\tilde{m}_q$ (table 6.1), corresponding to the physical meson mass, for the bare second moments for the vector mesons. The physical value for $am_q + am_{res}$ is shown by the solid vertical line in each case [1].*

| $am_{ud}$ | 0.008 | 0.006 | 0.004 | $\chi$-limit |
|---|---|---|---|---|
| $\langle \xi^2 \rangle_\pi^{\text{bare}}$ | 0.137(6) | 0.137(5) | 0.152(13) | 0.152(20) |
| $\langle \xi^1 \rangle_K^{\text{bare}}$ | 0.01912(121) | 0.01972(146) | 0.02079(175) | 0.0217(13)(5) |
| $\langle \xi^2 \rangle_K^{\text{bare}}$ | 0.129(3) | 0.131(3) | 0.134(10) | 0.135(12) |
| $\langle \xi^2 \rangle_{K,\text{PQ}}^{\text{bare}}$ | 0.131(3) | 0.132(3) | 0.134(8) | 0.137(11) |
| $\langle \xi^2 \rangle_\rho^{\parallel\ \text{bare}}$ | 0.136(9) | 0.127(7) | 0.137(11) | 0.130(22) |
| $\langle \xi^1 \rangle_{K^*}^{\parallel\ \text{bare}}$ | 0.02625(236) | 0.02803(193) | 0.02999(119) | 0.0309(12)(7) |
| $\langle \xi^2 \rangle_{K^*}^{\parallel\ \text{bare}}$ | 0.119(6) | 0.129(4) | 0.128(9) | 0.143(16) |
| $\langle \xi^2 \rangle_{K^*,\text{PQ}}^{\parallel\ \text{bare}}$ | 0.121(7) | 0.129(4) | 0.127(6) | 0.135(12) |
| $\langle \xi^2 \rangle_\phi^{\parallel\ \text{bare}}$ | 0.118(5) | 0.117(3) | 0.118(3) | 0.119(8) |
| $\langle \xi^2 \rangle_{\phi,\text{PQ}}^{\parallel\ \text{bare}}$ | 0.120(5) | 0.118(3) | 0.121(4) | 0.121(8) |

**Table 9.6:** *Summary of results for the bare values of the distribution amplitude moments on the* $32^3$ *lattice. The errors are statistical and (in the first moment case) systematic due to the uncertainty in the physical point for the chiral extrapolation. PQ refers to results from partially quenched calculations.*

could be extracted. These extra measurements were performed locally on Southampton University's Iridis-3 cluster computer. The details for the $32^3$ PDA dataset are given in table 9.3, where we see that one difference between this and the $24^3$ ensemble is that the 0.008 and 0.006 are without any smearing, that is point source and sink ($LL - LL$). After the extensions, where the statistics for the $32^3$ dataset are comparable to the $24^3$ dataset, we see that the plateaus for the bare first moments (fig. 9.8) and bare second moments (fig. 9.9) have a similar behaviour to the $24^3$ dataset. Both datasets start around time-step 8 or 9 for the first moment and 5 or 6 for the second, and we also observe similar levels of noise. This suggests that the Hydrogen-like and Gaussian-like smearing confers little advantage for the extraction of these quantities. As before, for some of the meson moments it proves difficult to define the start of the plateau, for example the first moment for the $K^*$ with mass 0.006 fig. 9.8 (bottom panel), for which, as with all fits, the plateau is determined as described at the end of section 9.4. The values for the bare moments, as well as the physical points determined from the chiral extrapolations, are given in table 9.6.

It is instructive to compare the two ensembles ($32^3$ and $24^3$). However, because the two ensembles have different lattice spacings, we must renormalise the bare values before we may compare. We must also "match" the quark masses for the two

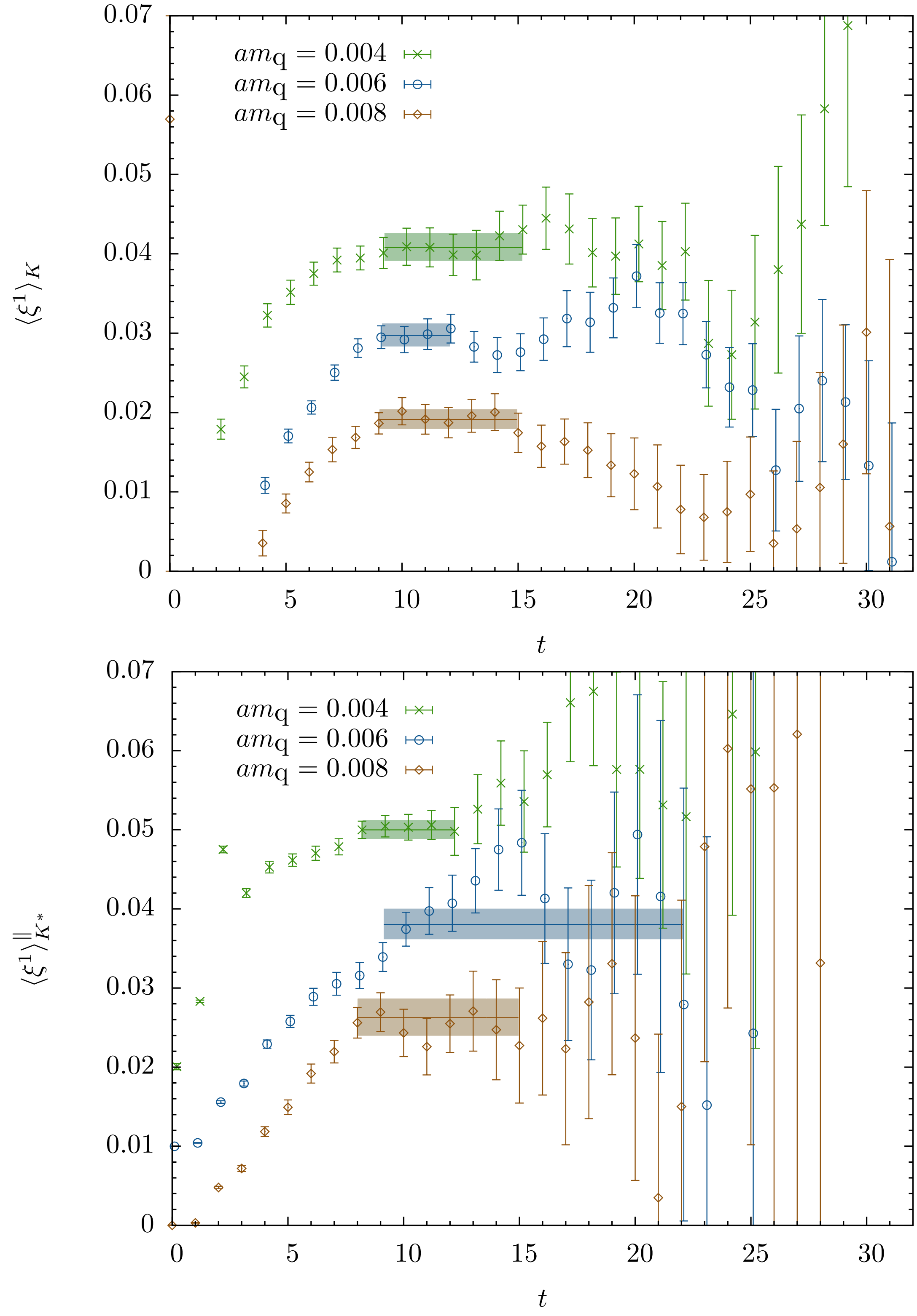

**Figure 9.8:** *Results for the* $\langle \xi^1 \rangle_K^{bare}$ *and* $\langle \xi^1 \rangle_{K^*}^{\parallel\, bare}$ *for the* $32^3$ *ensemble. The shaded area gives the fit-range, fitted values and errors.*

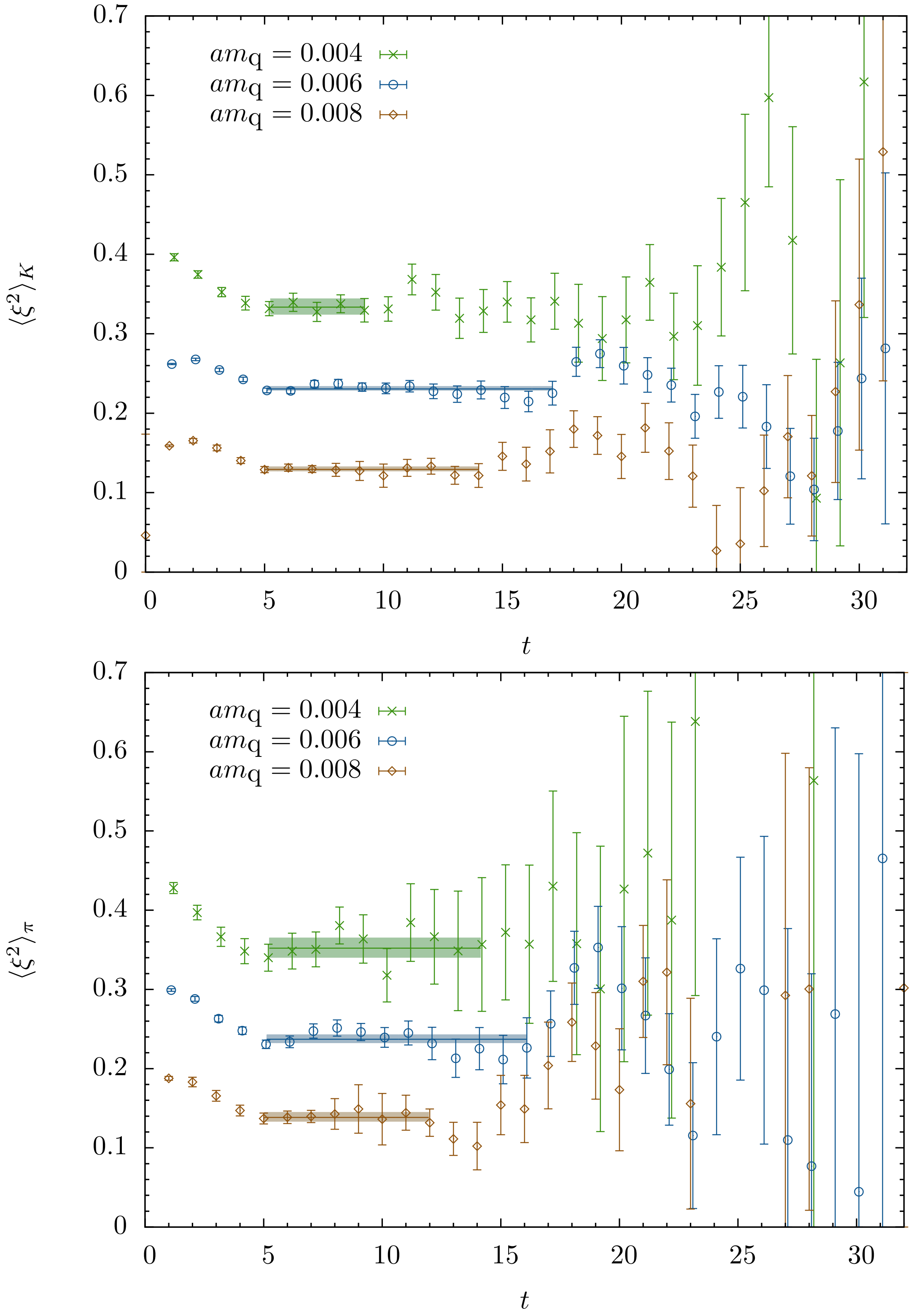

**Figure 9.9:** *Results for the* $\langle\xi^2\rangle_K^{bare}$ *and* $\langle\xi^2\rangle_\pi^{bare}$ *for both the* $32^3$ *ensembles. The shaded area gives the fit-range, fitted values and errors. Note that, except for the heaviest data-set, each successive mass from bottom to top has been offset incrementally by 0.1 in the y-axis.*

ensembles. The matching procedure is detailed in section D of [3], where matching factors are presented, which map the quark masses on one ensemble to their equivalent masses on another ensemble with a different $\beta$. The process is performed by requiring that the ratios of the hadronic masses (the same as those used to determine the lattice scale and initial quark masses, described in section 8.1) $\frac{m_{ll}}{m_{hhh}}$ and $\frac{m_{lh}}{m_{hhh}}$ are the same on all lattices at the matching point. This is an iterative process involving the repeated update of $m_l^{24}$ and $m_h^{24}$ through a series of interpolations. The results, once the process has converged for the light- and heavy-quark matching factors, are $Z_l^{24} = 0.981(9)$, $Z_h^{24} = 0.974(7)$ respectively, where

$$\begin{aligned} Z_f^{24} &= \frac{1}{R_a^{24}} \frac{\tilde{m}_f^{32}}{\tilde{m}_f^{24}} \quad \text{for} \quad f = l \text{ or } h \qquad (9.24) \\ R_a^{24} &= \frac{a^{32}}{a^{24}} \qquad (9.25) \end{aligned}$$

and $\tilde{m}$ is the quark mass in lattice units. For our comparison of the PDA moments on the two ensembles, we convert the $24^3$ quark masses to their $32^3$ equivalents using (9.24). The renormalisation of the moments is performed non-perturbatively, as detailed in section 7, where the renormalisation constants for the two ensembles are given in tables 7.8 and 7.9. We use the twisted results for a more consistent comparison, because both the $24^3$ and $32^3$ NPR results are in the same representation of the hypercubic group. The results after matching and renormalisation are displayed for the first moments in fig 9.10 and for the second moments pseudoscalar and vector mesons in figs. 9.11 and 9.12 respectively. For both of these, we see hints of discretisation effects in the difference of the renormalised central values (table 9.7) although they agree within errors. A further hint is the area of white space observed between the two fit bands (for $\langle \xi^1 \rangle_{K^*}^{\parallel}$, $\langle \xi^1 \rangle_K$, $\langle \xi^2 \rangle_K$ and $\langle \xi^2 \rangle_K$). Where there are points at similar values for the quark mass-difference on the two ensembles, the errors on the individual points overlap for the first moments and just miss for the second moments. We should note that we use the perturbative NPR result for the second moment mixing term and we cannot therefore be confident to ascribe this as a discretisation effect. The results obtained

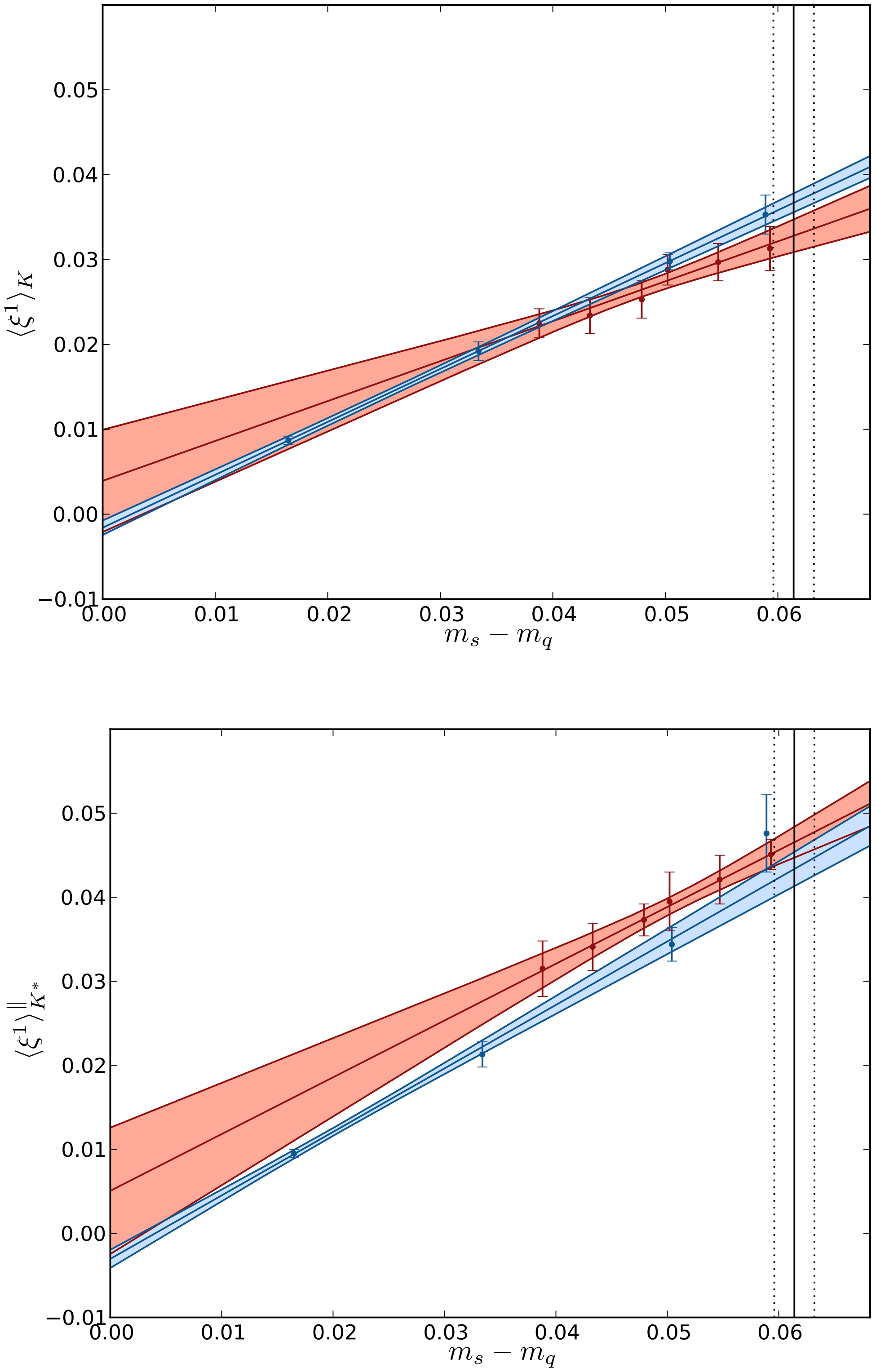

**Figure 9.10:** *Chiral extrapolations for $\langle \xi^1 \rangle_K$ and $\langle \xi^1 \rangle^{\parallel}_{K^*}$. The extrapolation to the physical point is shown by the vertical solid line, with uncertainty, dominated by the uncertainty in the physical strange mass, indicated by the dotted lines. The $24^3$ masses have been matched onto the $32^3$ scale, which is given in GeV. The blue and red points are the $24^3$ and $32^3$ ensembles respectively*

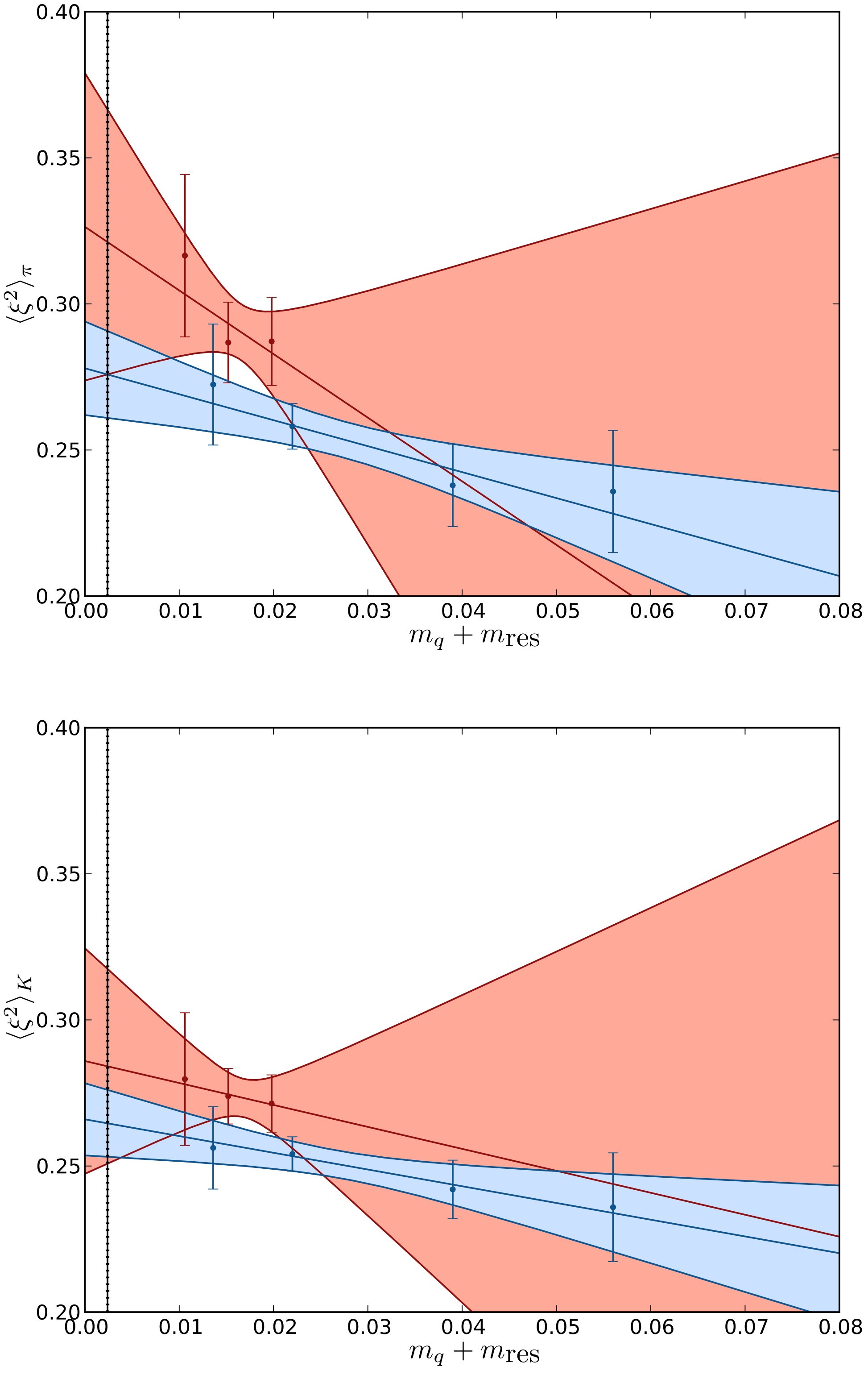

**Figure 9.11:** *Chiral extrapolations to the physical point for the renormalised moments for the second moment pseudoscalar mesons in* $\overline{MS}$ *at* $\mu = 2\,GeV$. *The physical points are given by the vertical solid line and the error by the vertical broken lines. The* $24^3$ *masses have been matched onto the* $32^3$ *scale, which is given in* $GeV$. *The blue and red points are the* $24^3$ *and* $32^3$ *ensembles respectively*

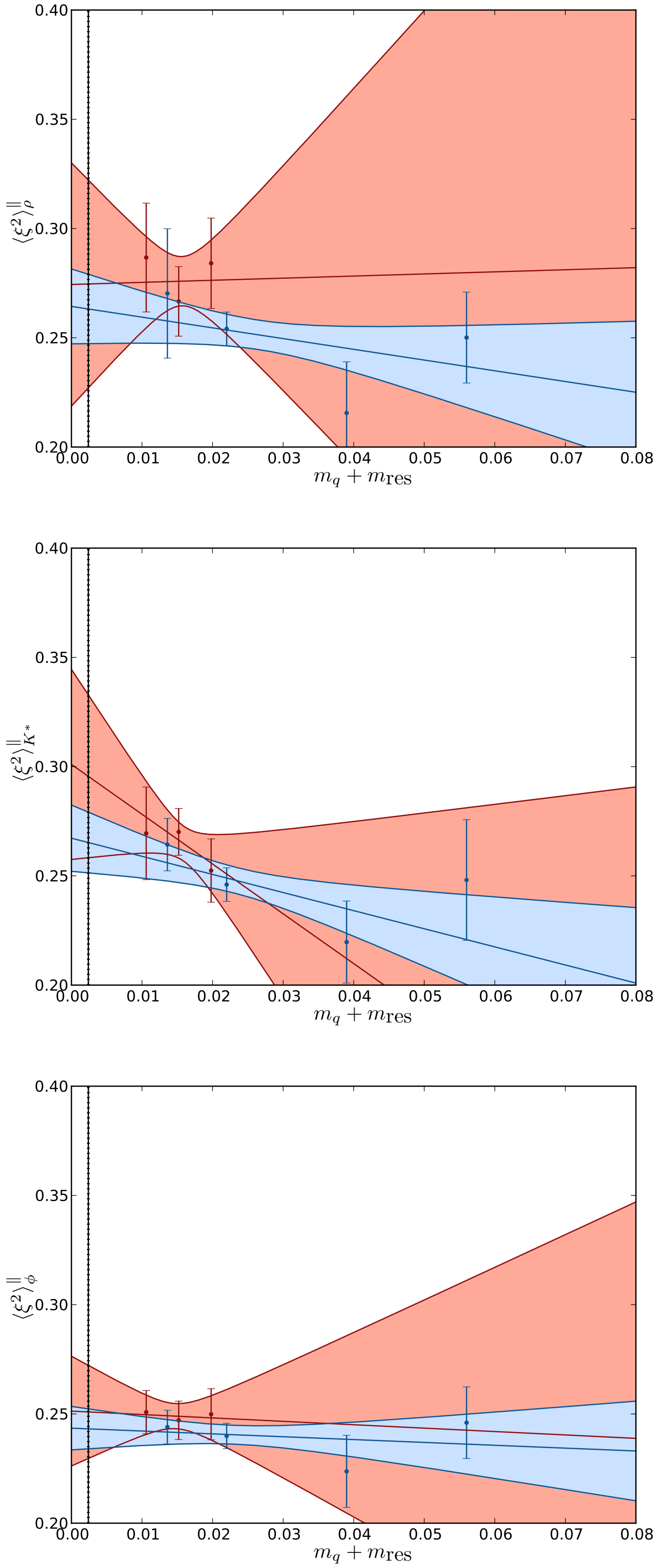

**Figure 9.12:** *Chiral extrapolations to the physical point for the renormalised moments for the second moment vector mesons in* $\overline{MS}$ *at* $\mu = 2GeV$*. The physical points are given by the vertical solid line and the error by the vertical broken lines. The* $24^3$ *masses have been matched onto the* $32^3$ *scale, which is given in GeV The blue and red points are the* $24^3$ *and* $32^3$ *ensembles respectively*

|  | $\langle\xi^2\rangle_\pi$ | $\langle\xi^1\rangle_K$ | $\langle\xi^2\rangle_K$ | $\langle\xi^2\rangle^{\Vert}_\rho$ | $\langle\xi^1\rangle^{\Vert}_{K^*}$ | $\langle\xi^2\rangle^{\Vert}_{K^*}$ | $\langle\xi^2\rangle^{\Vert}_\phi$ |
|---|---|---|---|---|---|---|---|
| $16^3$ | 0.25(1)(2) | 0.035(2)(2) | 0.25(1)(2) | 0.25(2)(2) | 0.037(1)(2) | 0.25(1)(2) | 0.24(1)(1) |
| $24^3$ | 0.28(1)(2) | 0.036(1)(2) | 0.27(1)(2) | 0.27(2)(2) | 0.043(2)(3) | 0.27(1)(2) | 0.25(1)(1) |
| $32^3$ | 0.32(4)(2) | 0.033(2)(1) | 0.28(2)(2) | 0.27(5)(2) | 0.046(2)(2) | 0.30(3)(2) | 0.25(2)(1) |

**Table 9.7:** *Final results in the chiral limit in $\overline{MS}$ at $\mu = 2GeV$ for all of our lattice volumes. The first error is statistical, the second includes systematic errors from $m_s$, discretisation and renormalisation.*

from the separate chiral extrapolations for both the $24^3$ and $32^3$ data sets provide us with the possibility of performing a continuum extrapolation. For this, we could assume $a^2$-scaling, however with only two points (two lattice spacings) available, it is not possible to test how well this assumed scaling works. The results for such a naïve extrapolation are given in table 9.8. It should be noted that the dynamical strange-quark mass has not been tuned to the same value on the two data sets and, further, that the ranges of the light-quark masses are different for the two ensembles [3]. For the $24^3$ ensemble, the chiral extrapolation is larger and we would expect it to have a larger uncertainty. A problem with this naïve method is that, whilst we can determine the continuum values for the moments, we are unable to isolate the discretisation effects in the continuum extrapolation from effects in the chiral extrapolation due to the initial separate chiral extrapolations. We therefore proceed with an alternative approach where we perform a "global" fit - a simultaneous continuum and chiral extrapolation of the two ensembles (after matching and renormalisation) using the following fit-forms

$$\langle\xi^1\rangle = c_{1,0} + c_{1,1}\tilde{m}_q + c_{1,2}a^2 \tag{9.26}$$

$$\langle\xi^2\rangle = c_{2,0} + c_{2,1}(m_s - m_q) + c_{2,2}a^2 \tag{9.27}$$

where we disregard (what we consider as) higher order terms such as $m^2$, $a^4$, $ma^2$, etc.. For this, the two extrapolations are disentangled and we are are able to observe the size of the effect of the respective terms in eq. (9.26) through the magnitude of their respective coefficients (table 9.8). We perform the global fits only for the most chiral points, which exclude the 0.03 and 0.02 $24^3$ quark masses as they are too heavy to be described by $SU(2)$ chiral perturbation theory. These

|  |  | Naive | Global - All |  |  |  | Global - Most chiral |  |  |  |
|---|---|---|---|---|---|---|---|---|---|---|
| $x$ | $y$ | $\langle\xi^x\rangle_y$ | $\langle\xi^x\rangle_y$ | $c_{x,0}$ | $c_{x,1}$ | $c_{x,2}$ | $\langle\xi^x\rangle_y$ | $c_{x,0}$ | $c_{x,1}$ | $c_{x,2}$ |
| 1 | $K$ | 0.029(5) | 0.033(2)(1) | -0.005 | 0.62 | 0.011 | 0.030(3)(1) | -0.001 | 0.50 | 0.017 |
| 1 | $K^*$ | 0.050(6) | 0.053(3)(1) | 0.007 | 0.75 | -0.031 | 0.052(3)(1) | 0.008 | 0.72 | -0.026 |
| 2 | $\pi$ | 0.37(10) | 0.34(2) | 0.34 | -0.91 | -0.190 | 0.35(3) | 0.35 | -1.88 | -0.158 |
| 2 | $K$ | 0.29(7) | 0.30(2) | 0.31 | -0.58 | -0.119 | 0.30(2) | 0.30 | -0.45 | 0.121 |
| 2 | $K^*$ | 0.34(7) | 0.29(2) | 0.29 | -0.92 | -0.071 | 0.30(2) | 0.31 | -2.18 | -0.037 |
| 2 | $\rho$ | 0.28(10) | 0.31(3) | 0.31 | -0.47 | -0.136 | 0.31(3) | 0.31 | -0.81 | -0.114 |
| 2 | $\phi$ | 0.26(5) | 0.26(1) | 0.26 | -0.12 | -0.050 | 0.26(2) | 0.26 | -0.34 | -0.041 |

**Table 9.8:** *Summary of results for the renormalised values of the distribution amplitude moments in* $\overline{MS}$ *at* $\mu = 2GeV$ *at the continuum* ($a^2 = 0$)*. The Naive results are calculated from the two point extrapolation of renormalised physical point values. "Global-All" and "Global-Most Chiral" results use the global fit forms including all and only the most chiral points (i.e. excluding 0.03 and 0.02* $24^3$ *masses) respectively. For the Global results the parameters from the fit are also included.*

|  | $\langle\xi^2\rangle_\pi$ | $\langle\xi^1\rangle_K$ | $\langle\xi^2\rangle_K$ | $\langle\xi^2\rangle^{\parallel}_\rho$ | $\langle\xi^1\rangle^{\parallel}_{K^*}$ | $\langle\xi^2\rangle^{\parallel}_{K^*}$ | $\langle\xi^2\rangle^{\parallel}_\phi$ |
|---|---|---|---|---|---|---|---|
| $24^3$ |  |  |  |  |  |  |  |
| All | 0.28(1)(2) | 0.036(1)(2) | 0.26(1)(2) | 0.27(1)(2) | 0.043(2)(3) | 0.25(2)(2) | 0.25(2)(1) |
| Chi | 0.30(4)(2) | 0.035(1)(1) | 0.26(3)(2) | 0.27(5)(2) | 0.043(2)(2) | 0.29(2)(2) | 0.25(2)(1) |
| $32^3$ |  |  |  |  |  |  |  |
| All | 0.32(4)(2) | 0.033(2)(1) | 0.28(3)(2) | 0.27(5)(2) | 0.046(2)(2) | 0.30(3)(2) | 0.25(2)(1) |
| Chi | 0.32(3)(2) | 0.033(2)(1) | 0.28(2)(2) | 0.29(5)(2) | 0.047(2)(2) | 0.29(2)(2) | 0.25(1)(1) |

**Table 9.9:** *Global results in* $\overline{MS}$ *at* $\mu = 2GeV$ *for the* $24^3$ *and* $32^3$ *lattices. The first error is statistical, the second includes systematic errors from* $m_s$*, discretisation and renormalisation. "All" and "Chi" results use the global fit forms including all and only the most chiral points (i.e. excluding 0.03 and 0.02* $24^3$ *masses) respectively.*

fits are shown for the first moments in fig. 9.13 and for the second moment pseudoscalar and vectors mesons in figs. 9.14 and 9.15 respectively. Fig. 9.16 shows the effect of including the 0.02 and 0.03 $24^3$ masses in the fits as a comparison. The continuum values for the moments as well as the fitted parameters, are given in table 9.8. The global plots will also affect the values for the moments at the physical points for the two lattice spacings for the $24^3$ and $32^3$ lattices. These are given in table 9.9 and may be contrasted with table 9.7.

Before any continuum extrapolations, the discretisation error was estimated as $\mathcal{O}(a^2\Lambda^2_{\text{QCD}}) \approx 4\%$ from the $\mathcal{O}(a)$-improved DWF action and operators. The moments that we have calculated are dimensionless objects, thus in our global fit form, $c_2$ must have dimensions of GeV$^2$, and we expect $c_2 = c_2'\Lambda^2_{\text{QCD}}$. Table 9.10

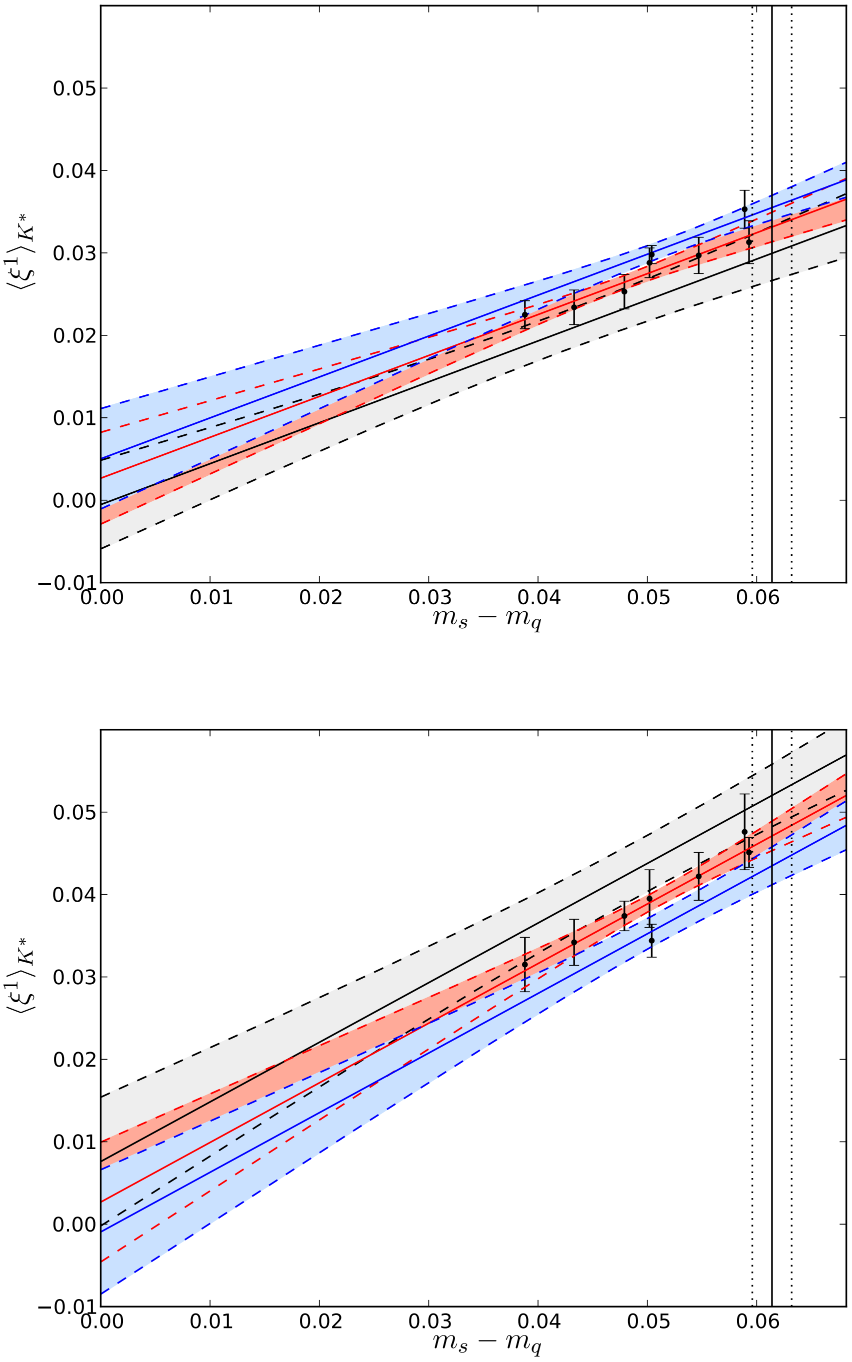

**Figure 9.13:** *Extrapolations to the physical point for the renormalised first moments in* $\overline{MS}$ *at* $\mu = 2GeV$ *using the Global fit-form, eq. 9.26, including only the "most chiral" mass points. The physical points are given by the vertical solid line and the error by the vertical broken lines. After the matching the x-scale is in terms of the* $32^3$ *ensemble and is given in GeV. The blue, red and black fits correspond to* $a^{-1} = 1.73(3)\,GeV$*,* $2.28(3)\,GeV$ *and at the continuum* $(a^2 \to 0)$ *respectively.*

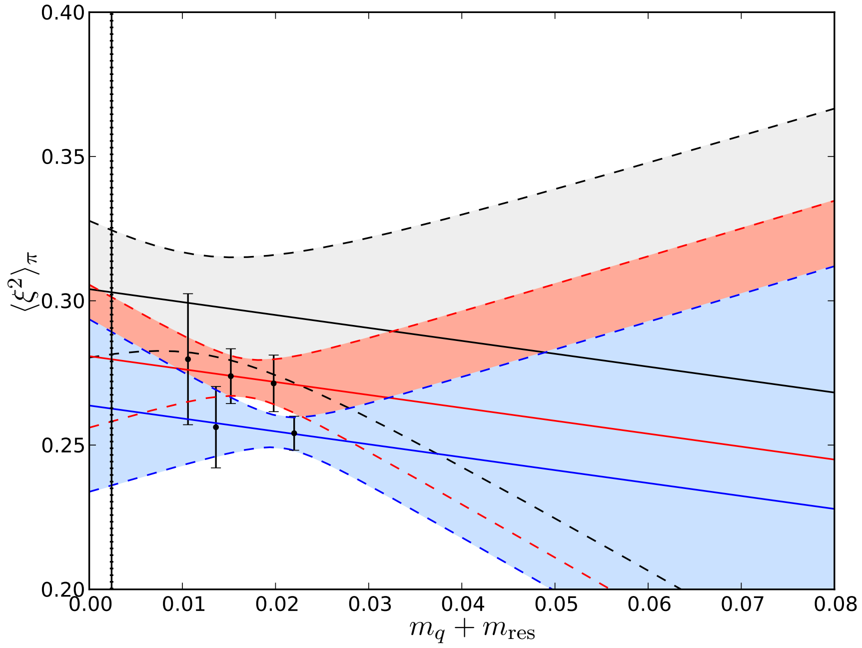

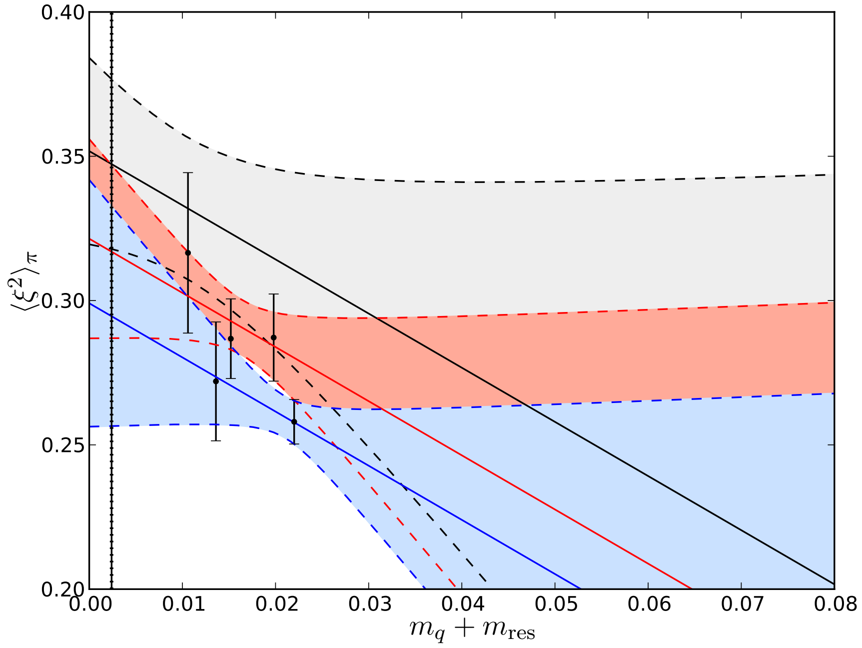

**Figure 9.14:** *Extrapolations to the physical point for the renormalised second pseudoscalar moments in* $\overline{MS}$ *at* $\mu = 2\,GeV$ *using the Global fit-form, eq. 9.27, including only the "most chiral" mass points. The physical points are given by the vertical solid line and the error by the vertical broken lines. After the matching the x-scale is in terms of the* $32^3$ *ensemble and is given in GeV. The blue, red and black fits correspond to* $a^{-1} = 1.73(3)\,GeV$, $2.28(3)\,GeV$ *and at the continuum* $(a^2 \to 0)$ *respectively.*

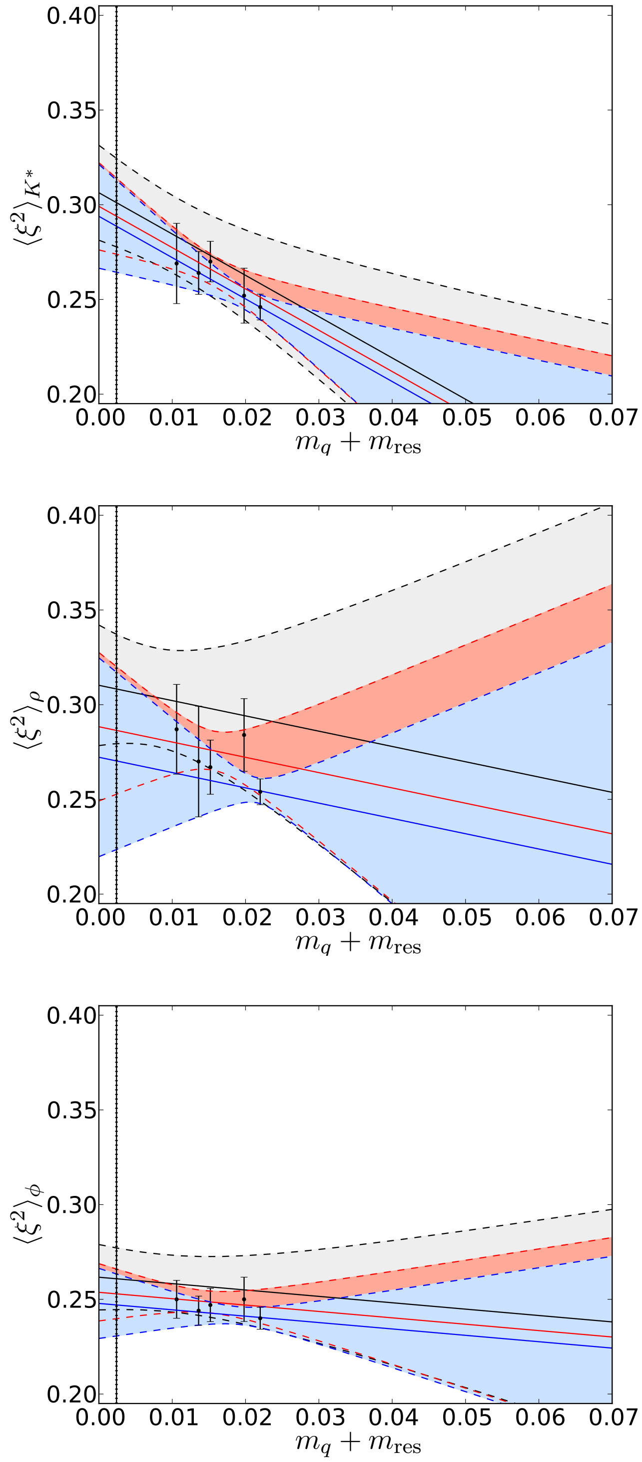

**Figure 9.15:** *Extrapolations to the physical point for the renormalised second vector moments in* $\overline{MS}$ *at* $\mu = 2GeV$ *using the Global fit-form, eq. 9.27, including only the "most chiral" mass points. The physical points are given by the vertical solid line and the error by the vertical broken lines. After the matching the x-scale is in terms of the* $32^3$ *ensemble and is given in GeV. After the matching the x-scale is in terms of the* $32^3$ *ensemble and is given in GeV. The blue, red and black fits correspond to* $a^{-1} = 1.73(3)\,GeV$, $2.28(3)\,GeV$ *and at the continuum* $(a^2 \to 0)$ *respectively.*

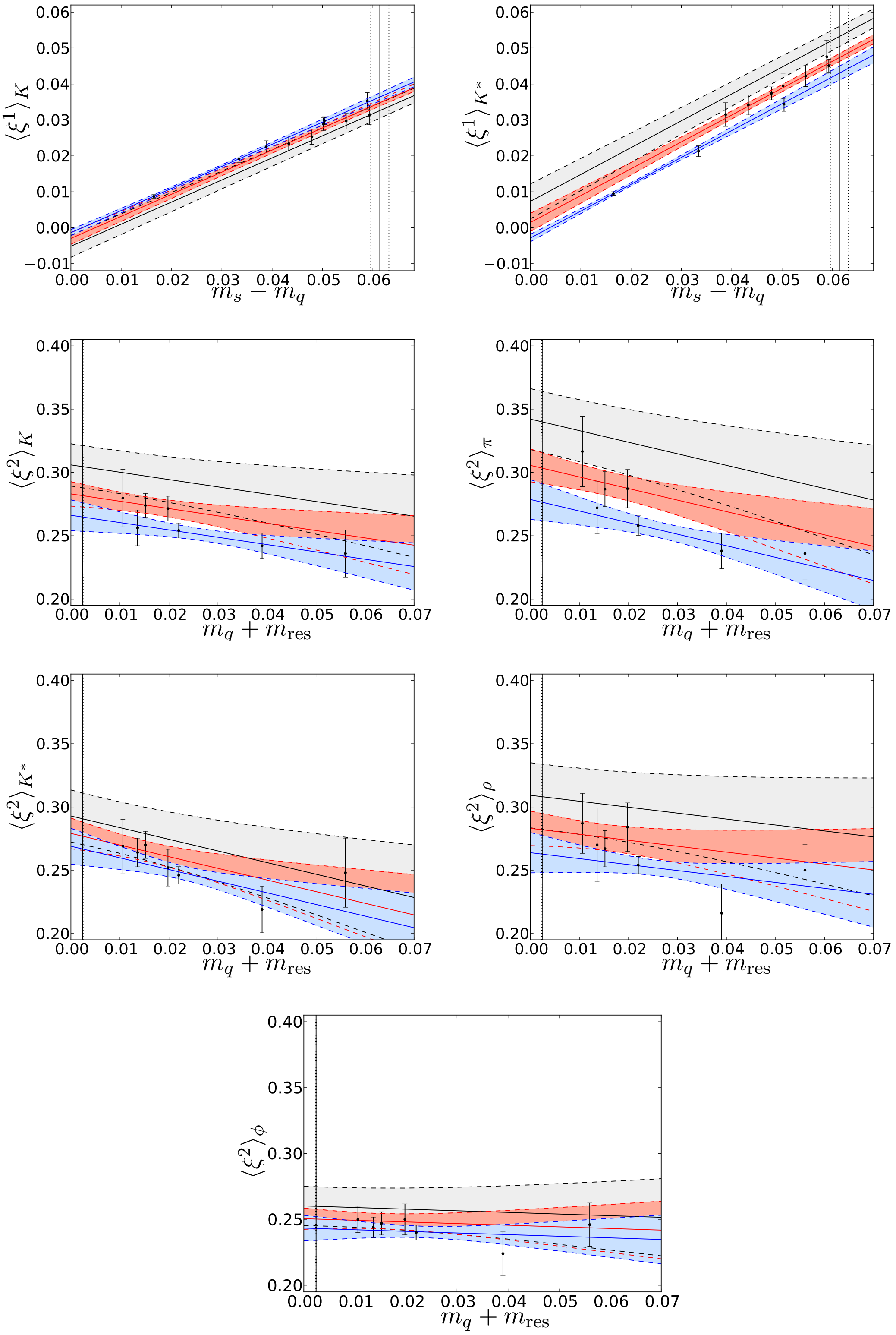

**Figure 9.16:** *Extrapolations to the physical point for the renormalised moments in* $\overline{MS}$ *at* $\mu = 2GeV$ *using the Global fit-form including all mass points. The physical points are given by the vertical solid line and the error by the vertical broken lines. After the matching the x-scale is in terms of the* $32^3$ *ensemble and is given in* $GeV$*. After the matching the x-scale is in terms of the* $32^3$ *ensemble and is given in* $GeV$*. The blue, red and black fits correspond to* $a^{-1} = 1.73(3)\,GeV$, $2.28(3)\,GeV$ *and at the continuum* ($a^2 \to 0$) *respectively.*

| $\langle\xi^x\rangle_y$ | | $c_{x,2}$ | $c'_{x,2}(\Lambda_{\rm QCD}=0.25)$ | $c'_{x,2}(\Lambda_{\rm QCD}=0.5)$ | $c'_{x,2}(\Lambda_{\rm QCD}=1)$ |
|---|---|---|---|---|---|
| 1 | $K$ | 0.0166 | 0.27 | 0.07 | 0.02 |
| 1 | $K^*$ | 0.0256 | 0.41 | 0.10 | 0.03 |
| 2 | $\pi$ | 0.1578 | 2.52 | 0.63 | 0.16 |
| 2 | $K$ | 0.1210 | 1.94 | 0.48 | 0.12 |
| 2 | $K^*$ | 0.0373 | 0.59 | 0.15 | 0.04 |
| 2 | $\rho$ | 0.1140 | 1.82 | 0.46 | 0.11 |
| 2 | $\phi$ | 0.0414 | 0.66 | 0.17 | 0.04 |

**Table 9.10:** *Coefficients of the $a^2$ term in the Global fit determined for a variety of $\Lambda_{QCD}$ values in GeV.*

shows the values for $c'_2$ for $\Lambda_{\rm QCD}=0.25$GeV, 0.5GeV and 1.0GeV. The coefficients for $\Lambda_{\rm QCD}=0.5$GeV are less than one and suggest that the approximation of a discretisation effect of order $\mathcal{O}(a^2\Lambda^2_{\rm QCD})$ is appropriate for this calculation, in the absence of a formal continuum extrapolation with more than two ensembles at different lattice spacings.

A comparison between the continuum results from this work and from QCDSF [37], are contained in table 9.11, where the results differ beyond their errors. However, we observe that our measurements for $N_f=2+1$ dynamical flavours correspond to pion masses in the range 330-670MeV, whereas the QCDSF results use two dynamical flavours and are for heavier pion masses of around 600MeV and above, and therefore require extrapolation over a larger range.

Clearly, we are unable to reconstruct the entire DAs from the first two moments alone, however we can look at the shape of the DAs for the pion and kaon using eq. (4.19) if we assume that all higher order moments are negligible. We do this for our values for the moments at the continuum from table 9.8 and for the $24^3$ and $32^3$ lattices, at different lattice spacings, from table 9.9. We see a skewed DA for the kaon, which indicates that strange quark carries more of the kaon's momentum. Whereas, we see a symmetric DA for the pion, which is what we would expect for a meson of degenerate quark flavours, we are basing this on only one moment (the second, as all odd moments are zero) and so it would be desirable to include more moments in future calculations to further check our expectations. This would, however, require operators with more covariant derivatives, for which it is considerably more difficult to control the operator mixing. Further to this we would

|  | this work | QCDSF [37] |
|---|---|---|
| $\langle\xi^1\rangle_K$ | 0.030(3)(1) | 0.0272(5)(17) |
| $\langle\xi^1\rangle_{K^*}$ | 0.052(3)(1) | - |
| $\langle\xi^2\rangle_\pi$ | 0.35(3) | 0.269(39) |
| $\langle\xi^2\rangle_K$ | 0.30(2) | 0.260(6)(16) |
| $\langle\xi^2\rangle_{K^*}$ | 0.30(2) | - |
| $\langle\xi^2\rangle_\rho$ | 0.31(3) | - |
| $\langle\xi^2\rangle_\phi$ | 0.26(2) | - |

**Table 9.11:** *Comparsion of continuum limit results for the PDAs in* $\overline{MS}$ *at* $\mu = 2GeV$.

require more non-zero components of momenta, which adds to the noise of the signal.

## 9.7 PDAs using Partially Twisted Boundary Conditions

An exploratory study into the use of partially twisted boundary conditions for the extraction of the PDA moments was performed in [114] using the datasets from the RBC/UKQCD $K \to \pi$ form factor runs [73], for two strange quark masses $am_s = 0.04$ (unitary) and $am_s = 0.03$ (partially quenched) respectively and the single unitary $am_q = 0.005$ light quark mass. The data-set consists of 1180 measurements [2]. The gauge field configurations are generated by combining sea quarks obeying periodic boundary conditions with valence quarks that have twisted boundary conditions [71]. The correlation functions were calculated, on these datasets, with zero Fourier momentum and we look at cases where only one of the valence quarks is twisted. Therefore the kaon's momentum is induced purely by the twist angle of the valence quark. The twist angle is only along one of the spatial directions, which is changed regularly in order to reduce correlations. The twist angles used for this analysis are $\theta_l = 1.600$ for the light quark for both strange quark masses which have $\theta_s = 2.5087(2.7944)$ for $am_s = 0.03(0.04)$ [2]. The momentum of the meson is then, $p = \theta/L$. Fig. 9.18 compares the partially twisted data with the untwisted data presented earlier (fig. 9.5). We see that the results agree within errors and that using twisted boundary conditions to extract the

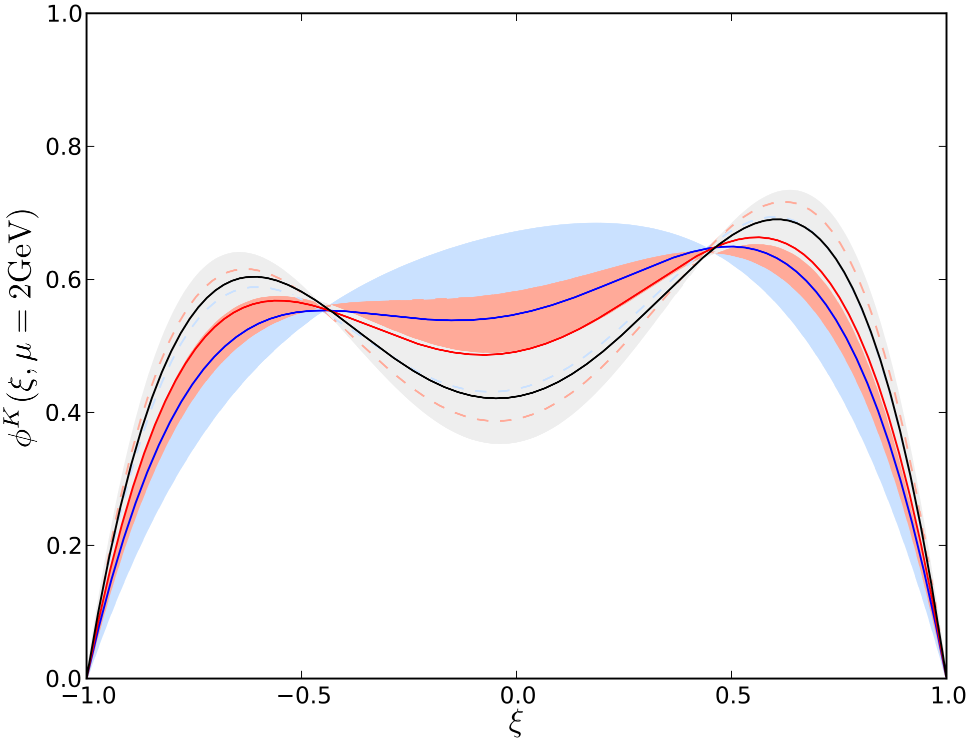

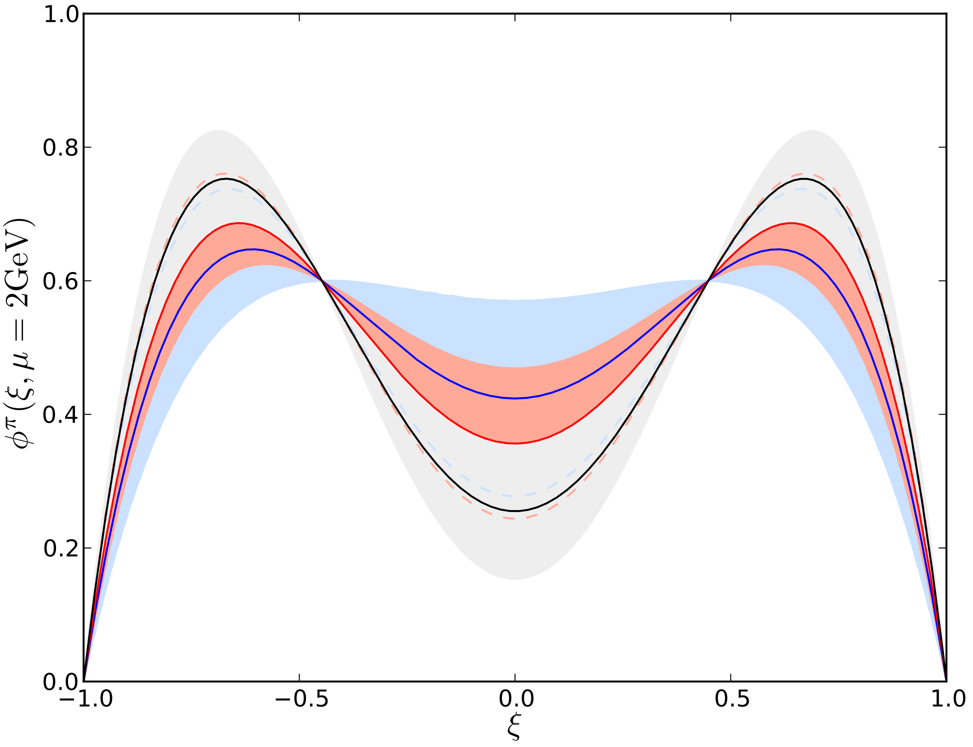

**Figure 9.17:** *Results for kaon and pion distribution amplitudes including the first and second moments, for the* $24^3$ *(blue),* $32^3$ *(red) and at the continuum (black) in* $\overline{MS}$ *at* $\mu = 2$ *GeV. The solid line gives the central values and the shaded area gives the error (both statistical and systematic). The dotted lines indicate where the error bands finish when there is an overlap between plots.*

moments of PDAs (at least for the kaon first moment) is possible. It should be noted that we only show the cases where the strange quark is twisted. The signal where we twist the light quark is too weak to allow a fit. The ratio from which we extract the first moment, eq. 9.7, is proportional to the momentum and hence the twist angle. The twist is small for the light quark and leads to a poor signal for the first moment. This does, however, demonstrate the possibility for using twisted boundary conditions for the extraction of the DAs.

We noted that the extraction of the higher order distribution amplitudes would require more non-zero components of momentum and hence suffers from the associated increase in noise that accompanies a larger magnitude of momenta. The extraction of the DAs with partially twisted boundary conditions could potentially provide a solution to this through using smaller components of momenta induced purely through the twist angle. We have seen that these cannot be arbitrarily small and some sort of balance between the initial signal and the noise is required. However, this application would provide an interesting and useful test for this technique.

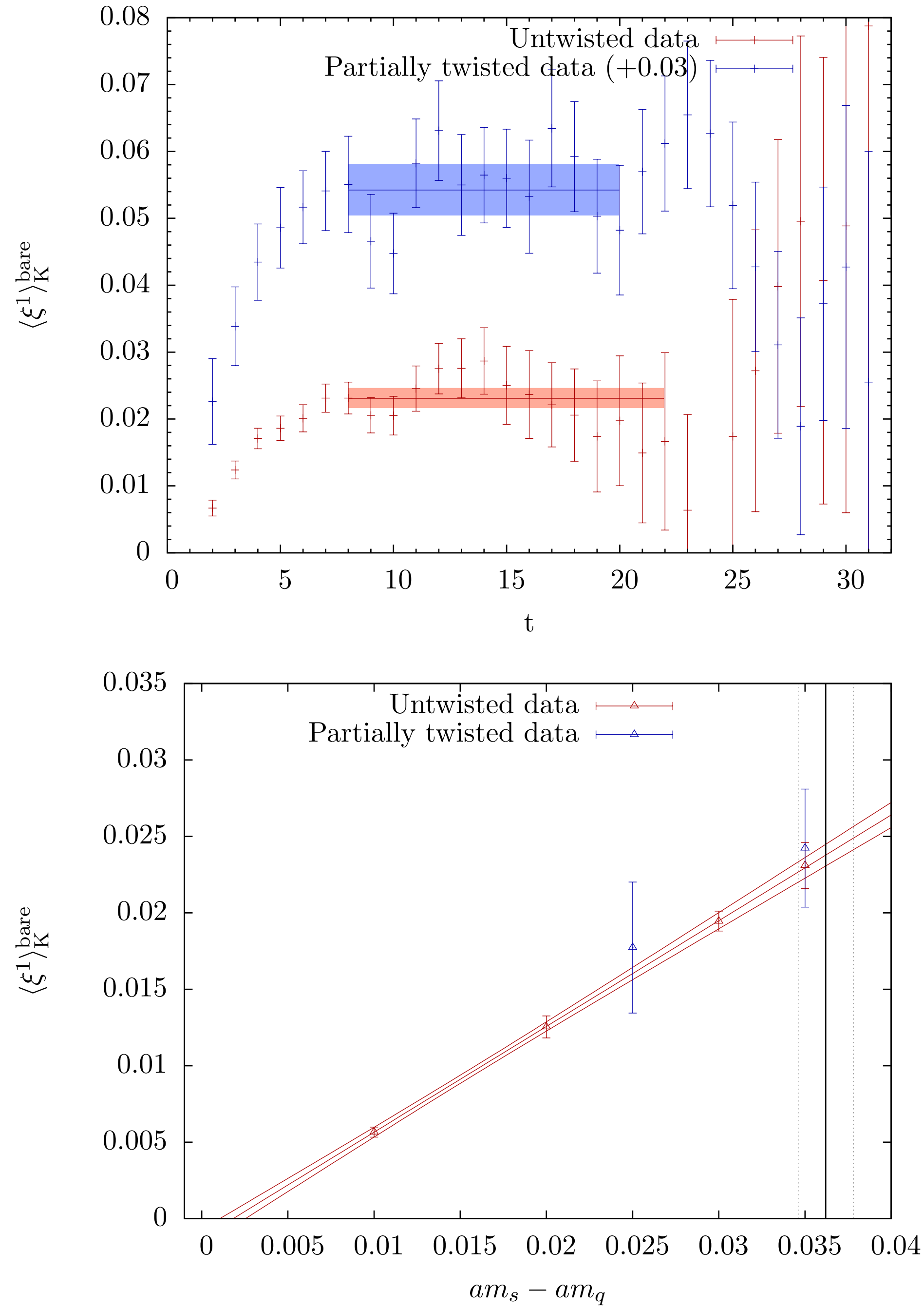

**Figure 9.18:** *Comparison of using twisted boundary conditions to induce momentum (blue data) with just using the Fourier momentum alone (red data), for the kaon first moment,* $24^3$*. The partially twisted data shown on the top panel is for the* 0.04 *mass strange quark, for which the data-points have been shifted by (*+0.03*) in the y-direction. The partially twisted data on the bottom panel shows the results for both the* 0.04 *and* 0.03 *mass strange quark.*

# Chapter 10

# Conclusions and Outlook

The work described in this thesis has been completed as part of the RBC/UKQCD $N_f = 2+1$ domain-wall fermion phenomenology program. A significant part of this work was the non-perturbative determination of the renormalisation factors for the operators involved in the extraction of moments for both the PDAs and structure functions. We used the the Rome-Southampton method for our non-perturbative renormalisation with an exceptional choice of momenta ($p' = p$). The renormalisation constants were calculated for the vector (and axial-vector) bilinears and operators containing one and two derivatives on three lattice ensembles, with parameters that allowed the study of both finite volume and discretisation effects. The use of momentum sources for the NPR calculations led to a significant reduction in statistical errors from previous work [97], this however highlighted a discretisation effect associated with the choice of momenta used to set the scale. The non-perturbative prescription requires an interpolation in the scale (determined by the momentum of the quark propagators), we therefore require simulations at a selection of different momenta. The momentum choices are likely to be in different representations of the hypercubic group, which leads to the observed splitting of the results in the interpolation (figs. 7.5 and 7.6). In order to study this effect, we used twisted boundary conditions to change the magnitude of the momenta whilst remaining in the same representation. This removed the observed splitting in our calculation, resulting in a more reliable interpolation to the result. This also enabled a better comparison between the ensembles, from which we see no obvious discretisation effects in the calculated renormalisation factors (cf. tables 7.9 and 7.8).

We obtained the bare lattice results for the pion's $\langle x \rangle$ moment for the structure functions, using a variety of channels for their extraction (table 8.2), from which we observed the expected difference by a factor of $Z_V$ between the methods that utilise two-point and three-point functions in the ratio with the three-point derivative operator. We observe that the operator $\mathcal{O}_{v2,b}$ provides a cleaner extraction of the moment because it avoids the need for momenta, in agreement with the work performed by the QCDSF collaboration [105, 110]. Unfortunately, our calculation of the non-perturbative renormalisation constants for this operator is not as clean as for the $\mathcal{O}_{v2,a}$ operator as we are limited in the averaging over equivalent indices. Further to this we highlighted the potential improvement to the result and determination of our error estimates that the use of twisted boundary conditions could provide. We present the renormalised result $\langle x \rangle = 0.249(12)$ which, corresponds to the light quarks carrying approximately 50% of the pions momentum, the rest of which we attribute to the heavier quark generations and the gluons. Table 8.4 compares our result with the QCDSF collaboration, where we find agreement at the limit of the errors, however we note that the QCDSF calculation uses two dynamical flavours. The calculation of the pion $\langle x \rangle$ moment, a flavour-singlet, should in principle contain contributions from disconnected diagrams, which are not considered here. Disconnected terms have been considered for the nucleon in [108]. A further caveat to the calculation is that there may also be a contribution from a $\mathrm{tr}(F_{\mu\rho}F^{\rho\nu})$ term occuring from the gluon contribution in the covariant derivative in the operator. The calculation of this contribution is both noisy and expensive, it has however been calculated for the pion in [109]. Both of these restrictions to the complete calculation for the structure function moments would be of great interest to pursue, and would provide an excellent check of existing experimental results for the pdfs, such as MSTW [115] and other groups. A further extension to this work is to calculate the structure function moments for the kaon and other mesons.

The PDAs have been obtained for the light mesons, where we observe the expected $SU(3)$ breaking effects and the expected chiral behaviour of the $\langle\xi^1\rangle_K$. This calculation was performed on three ensembles allowing some evaluation of finite volume and discretisation effects. We see no obvious finite volume effects in the results. The first and second moments, after renormalisation (table 9.7), agree within errors. However, when considering the ensembles together on a point-by-point basis in the chiral extrapolations (figs. 9.5 to 9.12) we start to observe a hint of discrepancy. Currently we cannot confidently ascribe this soley to discretisation effects, especially for the second moment due to the renormalisation. The renormalisation factor for the mixing with the total derivative that is required in the second moment calculation is currently inaccessible to our NPR calculations due to the exceptional scheme used. A non-exceptional method is therefore required, for which, the perturbative matching calculation has only very recently become available [99, 100]. This is therefore a high priority calculation which will allow a more robust statement to be made about the discretisation effects. A comparison between the continuum results from this work, obtained using a global fit-form (figs. 9.13 to 9.15), and from QCDSF [37], is contained in table 9.11. The results differ outside their errors, although we note that our measurements for $N_f = 2 + 1$ dynamical flavours correspond to pion masses in the range $330 - 670$MeV, whereas the QCDSF results use two dynamical flavours and are for heavier pion masses of around 600MeV and higher. A natural progression for the PDA work would be to consider the transversely polarised DAs and the nucleon PDAs for which the UKQCD/QCDSF collaboration have presented results [53]. We have also demonstrated the potential for PDA and structure function calculations with partially twisted boundary conditions, which allow for an improved control of the momentum's resolution.

# Bibliography

[1] R. Arthur *et al.*, *Lattice results for low moments of light meson distribution amplitudes*, *Physical Review D* **83** (Apr., 2011) 1–20.

[2] P. A. Boyle *et al.*, *$K\pi$ form factors with reduced model dependence*, *The European Physical Journal C* **69** (Aug., 2010) 159–167.

[3] Y. Aoki *et al.*, *Continuum Limit Physics from 2+1 Flavor Domain Wall QCD*, *Physics* **73** (Nov., 2010) 125 [`1011.0892`].

[4] J. Chadwick, *Possible Existence of a Neutron*, *Nature* **129** (Feb., 1932) 312–312.

[5] A. Das and T. Ferbel, *Introduction to Nuclear and Particle Physics.* World Scientific, 2004.

[6] R. A. Dunlap, *An introduction to the physics of nuclei and particles.* Thomson/Brooks-Cole, 2003.

[7] R. Taylor, *Deep inelastic scattering: The early years*, *Reviews of Modern Physics* **63** (July, 1991) 573–595.

[8] H. Kendall, *Deep inelastic scattering: Experiments on the proton and the observation of scaling*, *Reviews of Modern Physics* **63** (July, 1991) 597–614.

[9] J. Friedman, *Deep inelastic scattering: Comparisons with the quark model*, *Reviews of Modern Physics* **63** (July, 1991) 615–627.

[10] M. Gellmann, *A schematic model of baryons and mesons*, *Physics Letters* **8** (Feb., 1964) 214–215.

[11] G. Zweig, *An SU(3) Model for Strong Interaction Symmetry and its Breaking*, *CERN Report* **No.8182/TH** (1964) 24.

[12] G. Zweig, *An SU(3) Model for Strong Interaction Symmetry and its Breaking: II*, *CERN Report* **No.8419/TH** (1964).

[13] O. Greenberg, *Spin and Unitary-Spin Independence in a Paraquark Model of Baryons and Mesons*, *Physical Review Letters* **13** (Nov., 1964) 598–602.

[14] M. Y. Han, *Three-Triplet Model with Double SU(3) Symmetry*, *Physical Review* **139** (Aug., 1965) B1006–B1010.

[15] D. Gross and F. Wilczek, *Ultraviolet Behavior of Non-Abelian Gauge Theories*, *Physical Review Letters* **30** (June, 1973) 1343–1346.

[16] H. Politzer, *Reliable Perturbative Results for Strong Interactions?*, *Physical Review Letters* **30** (June, 1973) 1346–1349.

[17] M. E. Peskin and D. V. Schroeder, *Introduction to quantum field theory.* Addison-Wesley Pub. Co., 1995.

[18] N. Cabibbo, *Unitary Symmetry and Leptonic Decays*, *Physical Review Letters* **10** (June, 1963) 531–533.

[19] M. Kobayashi and T. Maskawa, *C P -Violation in the Renormalizable Theory of Weak Interaction*, *Progress of Theoretical Physics* **49** (Feb., 1973) 652–657.

[20] G. Bennett *et al.*, *Measurement of the Negative Muon Anomalous Magnetic Moment to 0.7 ppm*, *Physical Review Letters* **92** (Apr., 2004).

[21] M. Maggiore, *A modern introduction to quantum field theory.* Oxford University Press, 2005.

[22] M. Taizo, *Foundations Of Quantum Chromodynamics: An Introduction To Perturbative Methods In Gauge Theories (3Rd Edition) (World Scientific Lecture Notes in Physics).* World Scientific Publishing, 2009.

[23] C. Yang and R. Mills, *Conservation of Isotopic Spin and Isotopic Gauge Invariance*, *Physical Review* **96** (Oct., 1954) 191–195.

[24] K. Fujikawa, *Comment on Chiral and Conformal Anomalies*, *Physical Review Letters* **44** (June, 1980) 1733–1736.

[25] R. Feynman, *Very High-Energy Collisions of Hadrons*, *Physical Review Letters* **23** (Dec., 1969) 1415–1417.

[26] S. J. Brodsky and G. P. Lepage, *Exclusive processes in quantum chromodynamics*, *AIP Conference Proceedings* (1981), no. March 214–239.

[27] R. Devenish and A. Cooper-Sarkar, *Deep inelastic scattering.* Oxford University Press, 2004.

[28] T. Heinzl, *Light-Cone Quantization: Foundations and Applications*, `hep-th/0008096`.

[29] G. Lepage and S. Brodsky, *Exclusive processes in perturbative quantum chromodynamics*, *Physical Review D* **22** (1980), no. 9 2157–2198.

[30] C. Callan and D. Gross, *High-Energy Electroproduction and the Constitution of the Electric Current*, *Physical Review Letters* **22** (Jan., 1969) 156–159.

[31] J. Bjorken, *Asymptotic Sum Rules at Infinite Momentum*, *Physical Review* **179** (Mar., 1969) 1547–1553.

[32] M. Beneke, G. Buchalla, M. Neubert, and C. T. Sachrajda, *QCD Factorization in B to pi K, pi pi Decays and Extraction of Wolfenstein Parameters*, `hep-ph/0104110`.

[33] M. Beneke, G. Buchalla, M. Neubert, and C. T. Sachrajda, *QCD factorization for B to pi K decays*, `hep-ph/0007256`.

[34] V. Braun *et al.*, *Lattice calculation of vector meson couplings to the vector and tensor currents using chirally improved fermions*, *Physical Review D* **68** (Sept., 2003).

[35] V. Braun, *The Uses of conformal symmetry in QCD*, *Progress in Particle and Nuclear Physics* **51** (June, 2003) 311–398 [`hep-ph/0306057`].

[36] R. Shankar, *Principles of Quantum Mechanics.* Springer, 2008.

[37] V. M. Braun *et al.*, *Moments of pseudoscalar meson distribution amplitudes from the lattice*, `hep-lat/0606012`.

[38] V. Braun, G. Korchemsky, and D. Müller, *The Uses of conformal symmetry in QCD*, *Progress in Particle and Nuclear Physics* **51** (Jan., 2003) 311–398.

[39] A. Khodjamirian, T. Mannel, and M. Melcher, *Kaon distribution amplitude from QCD sum rules*, *Physical Review D* **70** (Nov., 2004) [`hep-ph/0407226`].

[40] V. Braun and A. Lenz, *SU(3) symmetry-breaking corrections to meson distribution amplitudes*, *Physical Review D* **70** (Oct., 2004) 15 [`hep-ph/0407282`].

[41] P. Ball and R. Zwicky, *SU(3) breaking of leading-twist K and KK distribution amplitudesa reprise*, *Physics Letters B* **633** (Feb., 2006) 289–297 [`hep-ph/0510338`].

[42] P. Ball and R. Zwicky, *Operator relations for SU(3) breaking contributions to K and K* distribution amplitudes*, *Journal of High Energy Physics* **2006** (Feb., 2006) 034–034 [`hep-ph/0601086`].

[43] K. G. Chetyrkin, A. Khodjamirian, and A. A. Pivovarov, *Towards NNLO Accuracy in the QCD Sum Rule for the Kaon Distribution Amplitude*, *Physics Letters B* (Dec., 2007) 14 [`0712.2999`].

[44] X.-G. Wu and T. Huang, *Implication on the pion distribution amplitude from the pion-photon transition form factor with the new BABAR data*, *Physical Review D* **82** (Aug., 2010) 19 [`1005.3359`].

[45] H.-J. Behrend *et al.*, *A measurement of the pi0, eta and eta-prime electromagnetic form factors*, *Zeitschrift fuer Physik C Particles and Fields* **49** (Sept., 1991) 401–409.

[46] V. Savinov, *Measurements of the Meson-Photon Transition Form Factors of Light Pseudoscalar Mesons at Large Momentum Transfer*, `hep-ex/9707028`.

[47] B. Aubert *et al.*, *Measurement of the* $\gamma\gamma{*}\pi 0$ *transition form factor*, *Physical Review D* **80** (Sept., 2009) 19 [`0905.4778`].

[48] V. Chernyak and A. Zhitnitsky, *Asymptotic behaviour of exclusive processes in QCD*, *Physics Reports* **112** (1984), no. 3-4 173–318.

[49] E. Arriola and W. Broniowski, *Pion light-cone wave function and pion distribution amplitude in the NambuJona-Lasinio model*, *Physical Review D* **66** (Nov., 2002) [`hep-ph/0207266`].

[50] G. Martinelli and C. T. C. Sachrajda, *The quark distribution amplitude of the proton: A lattice computation of the lowest two moments*, *Physics Letters B* **217** (Jan., 1989) 319–324.

[51] G. Martinelli and C. Sachrajda, *A lattice calculation of the second moment of the pion's distribution amplitude*, *Physics Letters B* **190** (May, 1987) 151–156.

[52] P. A. Boyle *et al.*, *The First Moment of the Kaon Distribution Amplitude from N_f=2+1 Domain Wall Fermions*, `hep-lat/0610025`.

[53] V. Braun *et al.*, *Nucleon distribution amplitudes and proton decay matrix elements on the lattice*, *Physical Review D* **79** (Feb., 2009).

[54] P. Hägler, *Hadron structure from lattice quantum chromodynamics*, *Physics Reports* **490** (May, 2010) 49–175.

[55] A. Pich, *Chiral Perturbation Theory*, `hep-ph/9502366`.

[56] A. V. Manohar, *Effective Field Theories*, `hep-ph/9606222`.

[57] S. R. Sharpe, *Applications of Chiral Perturbation theory to lattice QCD*, `hep-lat/0607016`.

[58] R. Gupta, *Introduction to Lattice QCD*, `hep-lat/9807028`.

[59] H. Nielsen, *A no-go theorem for regularizing chiral fermions*, *Physics Letters B* **105** (Oct., 1981) 219–223.

[60] G. P. Lepage, *Redesigning Lattice QCD*, `hep-lat/9607076`.

[61] T. DeGrand and C. DeTar, *Lattice methods for quantum chromodynamics.* World Scientific, 2006.

[62] A. D. Kennedy, *Algorithms for Dynamical Fermions*, `hep-lat/0607038`.

[63] K. Wilson, *Confinement of quarks*, *Physical Review D* **10** (Oct., 1974) 2445–2459.

[64] Y. Iwasaki, *Renormalization group analysis of lattice theories and improved lattice action. 2. four-dimensional nonabelian su (n) gauge model*, *Univ. of Tsukuba report UTHEP-118* **258** (1983) 141–156.

[65] D. Antonio *et al.*, *First results from 2+1-flavor domain wall QCD: Mass spectrum, topology change, and chiral symmetry with Ls=8*, *Physical Review D* **75** (June, 2007).

[66] C. Davies, *Lattice QCD - A guide for people who want results*, `hep-lat/0509046`.

[67] P. Ginsparg and K. Wilson, *A remnant of chiral symmetry on the lattice*, *Physical Review D* **25** (May, 1982) 2649–2657.

[68] D. Kaplan, *A method for simulating chiral fermions on the lattice*, *Physics Letters B* **288** (Aug., 1992) 342–347.

[69] Y. Shamir, *Chiral fermions from lattice boundaries*, *Nuclear Physics B* **406** (Sept., 1993) 90–106.

[70] P. F. Bedaque, *Aharonov-Bohm effect and nucleon-nucleon phase shifts on the lattice*, *Physics Letters B* **593** (Feb., 2004) 82–88 [`nucl-th/0402051`].

[71] C. T. Sachrajda and G. Villadoro, *Twisted Boundary Conditions in Lattice Simulations*, *Physics Letters B* **609** (Nov., 2004) 12 [`hep-lat/0411033`].

[72] J. M. Flynn, A. Juttner, and C. T. Sachrajda, *A Numerical Study of Partially Twisted Boundary Conditions*, *Physics Letters B* **632** (June, 2005) 10 [`hep-lat/0506016`].

[73] P. A. Boyle *et al.*, *Kl3 and pion form factors using partially twisted boundary conditions*, `0812.4265`.

[74] P. F. Bedaque and J.-W. Chen, *Twisted valence quarks and hadron interactions on the lattice*, *Physics Letters B* **616** (Dec., 2004) 11 [`hep-lat/0412023`].

[75] J. Mandula, *Representations of the rotation reflection symmetry group of the four-dimensional cubic lattice*, *Nuclear Physics B* **228** (Nov., 1983) 91–108.

[76] M. Göckeler *et al.*, *Lattice operators for moments of the structure functions and their transformation under the hypercubic group*, *Physical Review D* **54** (Nov., 1996) 5705–5714 [`hep-lat/9602029`].

[77] M. Clark and A. Kennedy, *Accelerating Dynamical-Fermion Computations Using the Rational Hybrid MonteCarlo Algorithm with Multiple Pseudofermion Fields*, *Physical Review Letters* **98** (Jan., 2007) 4 [`hep-lat/0608015`].

[78] P. A. Boyle *et al.*, *Hardware and software status of QCDOC*, *Nuclear Physics B - Proceedings Supplements* **129-130** (Mar., 2004) 838–843 [`hep-lat/0309096`].

[79] P. Boyle *et al.*, *The QCDOC Project*, *Nuclear Physics B - Proceedings Supplements* **140** (Mar., 2005) 169–175.

[80] P. A. Boyle, C. Jung, and T. Wettig, *The QCDOC supercomputer: hardware, software, and performance*, `hep-lat/0306023`.

[81] developed by members of Columbia University, Brookhaven National Laboratory and UKQCD, "Columbia Physics System code http://qcdoc.phys.columbia.edu/cps.html.."

[82] P. A. Boyle, *BAGEL assembler generator, http://www.ph.ed.ac.uk/˜paboyle/bagel/Bagel.html*, 2005.

[83] P. A. Boyle, *The BAGEL assembler generation library*, *Computer Physics Communications* **180** (Dec., 2009) 2739–2748.

[84] R. Edwards and B. Joo, *The Chroma Software System for Lattice QCD*, *Nuclear Physics B - Proceedings Supplements* **140** (Mar., 2005) 832–834.

[85] C. Allton *et al.*, *Physical results from 2+1 flavor domain wall QCD and SU(2) chiral perturbation theory*, *Physical Review D* **78** (Dec., 2008) 133 [`0804.0473`].

[86] D. Toussaint and C. Davies, *The Ω and the strange quark mass*, *Nuclear Physics B - Proceedings Supplements* **140** (Mar., 2005) 234–236 [`hep-lat/0409129`].

[87] B. Tiburzi and A. Walkerloud, *Decuplet baryon masses in partially quenched chiral perturbation theory*, *Nuclear Physics A* **748** (Feb., 2005) 513–536 [`hep-lat/0407030`].

[88] C. Allton *et al.*, *2+1 flavor domain wall QCD on a (2 fm)3 lattice: Light meson spectroscopy with Ls=16*, *Physical Review D* **76** (July, 2007) 17 [`hep-lat/0701013`].

[89] G. Martinelli, C. Pittori, C. T. Sachrajda, M. Testa, and A. Vladikas, *A General Method for Non-Perturbative Renormalization of Lattice Operators*, `hep-lat/9411010`.

[90] J. Gracey, *Three loop anomalous dimension of the second moment of the transversity operator in the ? and RI schemes*, *Nuclear Physics B* **667** (Sept., 2003) 242–260 [`hep-ph/0306163`].

[91] J. A. Gracey, *Three loop anomalous dimensions of higher moments of the non-singlet twist-2 Wilson and transversity operators in the bar Mbar S and RI schemes*, *Journal of High Energy Physics* **2006** (Oct., 2006) 040–040 [`hep-ph/0609231`].

[92] M. A. Donnellan, *Moments of Light-Meson Distribution Amplitudes from Lattice QCD*. PhD thesis, 2008.

[93] S. Capitani, *Lattice perturbation theory*, *Physics Reports* **382** (July, 2003) 113–302 [`hep-lat/0211036`].

[94] S. Aoki, T. Izubuchi, Y. Kuramashi, and Y. Taniguchi, *Perturbative renormalization factors of quark bilinear operators for domain-wall QCD*, *Physical Review D* **59** (Apr., 1999).

[95] S. Aoki, T. Izubuchi, Y. Kuramashi, and Y. Taniguchi, *Perturbative renormalization factors in domain-wall QCD with improved gauge actions*,

*Physical Review D* **67** (May, 2003) 44 [`hep-lat/0206013`].

[96] S. Aoki, T. Izubuchi, Y. Kuramashi, and Y. Taniguchi, *Perturbative renormalization factors in domain-wall QCD with improved gauge actions*, *Physical Review D* **67** (May, 2003) 1–26.

[97] Y. Aoki *et al.*, *Nonperturbative renormalization of quark bilinear operators and BK using domain wall fermions*, *Physical Review D* **78** (Sept., 2008) 80 [`0712.1061`].

[98] S. Bethke, *The 2009 world average of $\alpha$ s*, *The European Physical Journal C* **64** (Oct., 2009) 689–703 [`0908.1135`].

[99] J. A. Gracey, *RI/SMOM scheme amplitudes for quark currents at two loops*, *The European Physical Journal C* **71** (Mar., 2011).

[100] J. Gracey, *Amplitudes for the n=3 moment of the Wilson operator at two loops in the RI^{}/SMOM scheme*, *Physical Review D* **84** (July, 2011) [`1105.2138`].

[101] M. Gockeler *et al.*, *Nonperturbative Renormalisation of Composite Operators in Lattice QCD*, *Nuclear Physics B* **544** (July, 1998) 41 [`hep-lat/9807044`].

[102] P. A. Boyle *et al.*, *Parton Distribution Amplitudes and Non-Perturbative Renormalisation*, `0810.1669`.

[103] K. Nakamura, *Review of Particle Physics*, *Journal of Physics G: Nuclear and Particle Physics* **37** (July, 2010) 075021.

[104] G. Martinelli and C. T. Sachrajda, *A lattice calculation of the pion's form factor and structure function*, *Nuclear Physics B* **306** (1988), no. 4 865–889.

[105] C. Best *et al.*, *Pion and Rho Structure Functions from Lattice QCD*, `hep-lat/9703014`.

[106] M. Diehl, A. Manashov, and A. Schafer, *Generalized parton distributions for the pion in chiral perturbation theory*, *Physics Letters B* **622** (Aug., 2005) 69–82.

[107] M. Diehl, A. Manashov, and A. Schäfer, *Generalized parton distributions for the nucleon in chiral perturbation theory*, *The European Physical Journal A* **31** (Feb., 2007) 335–355.

[108] M. Deka *et al.*, *Moments of nucleons parton distribution for the sea and valence quarks from lattice QCD*, *Physical Review D* **79** (May, 2009).

[109] H. Meyer and J. Negele, *Gluon contributions to the pion mass and light-cone-momentum fraction*, *Physical Review D* **77** (Feb., 2008) 4 [`0707.3225`].

[110] D. Brömmel, *Pion Structure from the Lattice.* PhD thesis, 2007.

[111] C. R. Allton, C. T. Sachrajda, and C. Michael, *Gauge-invariant smearing and matrix correlators using Wilson fermions at $\beta$=6.2*, *Physical Review D* **47** (June, 1993) 5128–5137 [`hep-lat/9303009`].

[112] P. Boyle, *A novel gauge invariant multi-state smearing technique*, *Physics* (Mar., 1999) 18 [`hep-lat/9903033`].

[113] J.-W. Chen and I. Stewart, *Model-Independent Results for SU(3) Violation in Light-Cone Distribution Functions*, *Physical Review Letters* **92** (May, 2004) 4 [`hep-ph/0311285`].

[114] R. Arthur *et al.*, *Light Meson Distribution Amplitudes*, p. 7, PoS(Lattice 2010)154, Nov., 2010. `1011.2883`.

[115] P. Sutton, A. Martin, R. Roberts, and W. Stirling, *Parton distributions for the pion extracted from Drell-Yan and prompt photon experiments*, *Physical Review D* **45** (Apr., 1992) 2349–2359.